Ph.D. Dissertation in Mechanical Engineering

Enhanced Human-Robot-Environment Interactions Enabled by Multi-Stiffness Soft Sensors and Interactive Control

다중 강성 소프트 센서와 인터랙티브 제어를 통한 향상된 인간-로봇-환경 상호작용

February 2024

Graduate School of Mechanical Engineering
Seoul National University

Myungsun Park

다중 강성 소프트 센서와 인터랙티브 제어를 통한 향상된 인간-로봇-환경 상호작용

Enhanced Human-Robot-Environment Interactions Enabled by Multi-Stiffness Soft Sensors and Interactive Control

지도교수 박용래

이 논문을 공학박사 학위논문으로 제출함

2023 년 10 월

서울대학교 대학원

기계공학부

박 명 선

박명선의 공학박사 학위논문을 인준함

2023 년 12 월

위 원 장 : 이 동 준 (인)

부위원장 : 박 용 래 (인)

위 원 : 양 진 규 (인)

위 원 : 한 경 원 (인)

위 원 : Carmel Majidi (Signature)

Abstract

This thesis addresses the grand challenge of making the robots friendly to humans and adaptive to the surrounding environment. The thesis makes attempts to improve the human-robot-environment interaction loop by seeking solutions from soft robotics technologies. To achieve the ultimate goal, three practical problems are defined.

The first problem is to accurately perceive each of the human, robot, and the environment. In Chapter 2, the multi-stiffness sensor structure with improved sensitivity is proposed to solve the problem. Theoretical modeling and experimental validation are presented to prove the performance of the structure.

The second problem is to measure the motion of human hands, which are actively and elaborately used for interacting with the robots and environments. To achieve both the accuracy of sensing and the structural simplicity, in Chapter 3, the multi-stiffness sensor-based wearable glove is developed and the post-processing method for collecting accurate ground truth data for calibration of the glove is proposed. The hand-tracking system is able to achieve unprecedented accuracy and robustness compared to the previous studies, which are shown through quantitative and qualitative evaluations.

The third problem is to connect the human and soft robots, by implementing self-sensing functionality to a soft robot for accurate control of its motion and developing a haptic device to transmit back the robot's states to the human. In Chapter 4, an ionic electroactive polymer-based actuator is selected as a solution because of its structural compactness, low input voltage, and inherent safety. By integrating the soft sensor into the actuator and using the customized haptic device, accurate teleoperation of the soft gripper system for a practical pick-and-place task is demonstrated.

The last problem is to connect the soft robots and the surrounding environments to complete the entire interaction loop. In Chapter 5, a method of hybrid system analysis is proposed that allows the high complexity of the soft robots' kinematics to be simplified. The method enables the robot to identify and adapt to the environment using the embedded sensors while interacting with it. A pneumatic gripper system trying to grasp an unknown object is selected as an example to implement the method. Based on the method, the robotic gripper successfully completes the given task by estimating the unknown size of the object and modulating its body position to grasp the object.

Keyword : Robotics, Human-Robot Interaction, Robot-Environment Interaction, Soft Robotics, Grippers, Multi-material, Human Motion Tracking, Hybrid System.

Student Number : 2018-20621

Acknowledgement

This thesis will be published as Myungsun Park's Ph.D. dissertation, but I did not write this alone. I would like to express my sincere gratitude to Professor Yong-Lae Park, who believed in me and guided me to become what I am today. I would like to thank Professor Dongjun Lee, Professor Jinkyu Yang, Professor Amy Kyungwon Han, and Professor Carmel Majidi, who helped me complete this thesis. I would like to thank Professor Moon Jeong Park, Professor Sumin Helen Koo, Taejun Park, Sohee John Yoon, Bomin Jeong, Hyeonseong Ham, Yunsik Ohm, and Soah Park for letting me enjoy the valuable time of collaboration. In particular, I would like to express my respect to Taejun Park, who has always been willing to provide great help and inspiration to this inexperienced 사수 - I sincerely support your upcoming days.

마지막으로 언제나 제 옆을 든든하게 지켜주는 엄마, 아빠, 명훈, 그리고 지훈 사랑합니다.

Table of Contents

List of Tables

Chapter 2

Chapter 3

Chapter 4

List of Figures

Chapter 2

Chapter 3

Chapter 4

Chapter 5

Chapter 1

Introduction

1.1. Motivation and background

Traditionally, robotic systems have used their competence in rigidity, power, and repeatability to serve elaborate, dangerous, and tedious tasks for humans. A grand challenge for next-generation robotics is to make these entities friendly to humans and adaptive to the environment to enable active but safe interactions with them. The interaction between humans, robots, and the environment ultimately aims to improve the quality of human life through a wider range of functionalities beyond those played by the robots so far. Seamless interaction between humans and robots, which enables remote manufacturing, assistance of human labor, and augmentation of human experience for entertainment or education, has been desired for a long time. To achieve this, various approaches have been tried such as designing mechanically compliant robots and developing methods for perception of human intention and safe control [1,2]. On the other hand, force sensing and control technologies for stable and robust interaction between robots and the surrounding environment have been extensively studied [3] as well.

Recently, beyond independently considering the human-robot and robot-environment interactions, researchers are trying to comprehensively analyze the entire system. Han et al. tried to identify the robot dynamics and decouple the external forces toward the robot from humans and the environment by considering the coupling effect [4]. To achieve a semi-autonomous control of the robotic system, Chotiprayanakul et al. proposed a method to capture the interaction between a robot and an unstructured environment and developed an intuitive haptic interface [5]. Xiao et al. analyzed a clinical system consisting of a surgeon, an ultrasound transducer device, and a patient's skin as an environment, which is for non-invasive imaging of tissue [6]. Sierra et al. [7] and Jimener et al. [8] focused on the clinical device for walking assistance, where they suggested a framework that transmits the environmental information to the patient or the therapist via haptic feedback. All of these previous studies tried to achieve a precise, intuitive, and safe interaction in perspective of enhanced system identification, perception of the environment, and force or position control.

On the other hand, another approach to addressing the grand challenge has also existed. Some researchers have tried to manufacture robots with compliant materials or mechanisms which are called soft robots. The compliant characteristics of the soft robots inherently ensure safety when interacting with humans and show adaptability to and resilience against harsh environments. However, in translating the technology into real life, there still exist many obstacles, especially in realizing the accurate, safe, and adaptive interconnection between soft robots, humans, and the surrounding environments.

1.2. Problems definition

First, sensor technologies are required to accurately measure each of the systems without disrupting the interaction between them. Many soft sensor technologies have been proposed [9], but generally, their application to actual systems has been limited by the strong trade-off relationship between sensing performance and structural integrity or compliance [10].

Second, interpretation of the human intention and implementation of it in the system is important but difficult. In particular, since the hand is an actively used body part for communication for many individuals [11,12], hand motion-tracking technology has been developed for a long time, and a wide range of commercial products have been released [13,14,15,16]. But for tracking the hand motion, as with the previous problem, it is necessary to minimize the mechanical hindrance and discomfort to the user while ensuring accuracy in tracking, and the state of the art of the existing technologies has not yet reached the desired performance [17].

The next problem is to embody a close connection between humans and robots. In other words, hardware interfaces have to be developed to transmit the human's intention to the robot and also the robot's response to the human. The problem can be specified as satisfying two specific requirements. One is to control the robots in consideration of the human intention by enabling accurate perception of the states of the robots, which is a challenging problem for them having compliant bodies. The other one is to develop effective feedback devices that deliver the information of the robots to the human. These two requirements have been addressed by a broad range of approaches for a variety of systems. In this thesis, we especially focus on an *i*EAP (ionic electroactive polymer)-based robotic gripper system, which is ultra-thin, soft, and safe, but not much effort has been put to use them as human-robot interfaces for some limitations. The efforts of this thesis are based on the belief that the exceptional characteristics of the *i*EAP actuator for safety and compactness are advantageous for human-robot-environment interaction.

The last problem is to build a strong connection between the robot and the environment, through which the robot perceives its surrounding environment, adapts to it, and operates towards it. While the compliance of the soft robots guarantees safety during the interaction with humans and the environment, it also brings difficulties in accurate perception and control of the robots. The problem comes from the fact that the number of sensors or actuators is always limited compared to the infinite degree of freedom of soft robots. Since when a larger number of sensors or actuators are used the system becomes bulkier and more expensive, we should thoroughly understand and express the target system to optimize the design of the system so that better perception, adaptation, and operation can be achieved.

1.3. Solutions overview

In this thesis, we discuss four technical barriers to real-world soft robotics for advanced interaction between humans, robots, and the environment, and propose potential solutions. In each of the following chapters, we first define the problems in detail and study previous approaches to address them. In every chapter, the proposed concept or method is embodied in the real world, subjected to various experiments, and also applied to practical scenarios to display not only the validity of the concept but also the future direction of soft robotics for human-robot-environment interactions.

In Chapter 2, we solve the problem of measuring large deformation with precision and compliance by improving the sensitivity of a conventional soft strain sensor by developing a multi-stiffness structure. We explain the operating principle of this sensor structure both theoretically and experimentally by parameterizing it with two design parameters, discuss the design optimization, and also suggest a wearable application of the enhanced sensitivity.

In Chapter 3, we try to accurately measure human hand motions with comfort by developing a soft wearable glove based on the enhanced sensitivity and accuracy of the developed multi-stiffness sensor, and by collecting highly robust ground truth hand motion data through motion capture. We explain the principle of the improved accuracy and comfort of the hardware, and how the post-processing method achieves the ground truth data. The performance of the overall system is evaluated both quantitatively and qualitatively. Then, some virtual reality applications are demonstrated.

In Chapter 4, we define two sub-problems for the problem of connecting humans and robots. Identifying that the problems have not yet been addressed for a soft robotic actuator (ionic electroactive polymer, *i*EAP), we solve each of the problems by achieving the self-sensing functionality of the actuator and also by developing a haptic device using it. The work is based on the belief that the *i*EAP's exceptional characteristics for safety and compactness are advantageous for human-robot-environment interaction. To implement the *i*EAP's self-sensing functionality, we propose a design for sensor embedding and conduct the structural analysis to optimize the design. Also, a haptic device is developed to be integrated into a teleoperation system, together with the self-sensing *i*EAP and also the sensing glove from Chapter 3, showing the practical advantage for human-robot interactions.

In Chapter 5, to make the robot perceive the surrounding environment, adapt to it, and operate towards it, we propose a hybrid system analysis method that can simply model the complex interactions between soft robots and the environment. Taking an exemplar application of a gripper system with soft pneumatic actuators, the method is applied to attain information about the object to be grasped (environment) while using a minimum number of sensors and actuators, and then to autonomously control the grippers' motions accordingly. The system is demonstrated to perform a high-level grasping task for various unknown environmental conditions, which widens the applicability of the proposed method.

Chapter 2

Multi-Stiffness Structure for Enhanced Sensitivity*

2.1. Introduction

2.1.1. Motivation and background

Highly stretchable strain sensors that can measure large deformation with minimum mechanical load and physical interference are highly demanded for accurate measurement of the deformation in various robotic systems. The existing stretchable sensors are largely classified into five types according to their sensing mechanisms: geometrical effect, piezoresistive effect, disconnection, crack propagation, and tunneling effect [10]. Among them, the geometrical effect-based sensors measure resistance change of the conductive path filled with sensing medium when the sensor is stretched. Typically, the sensors are composed of an elastomer body and embedded liquid conductors such as room-temperature liquid metal [18,19] or ionic liquid [20]. Due to the inherent softness of the materials and the compliance of the mechanism, which cannot be achieved by other types of sensors, the geometrical effect-based soft sensors have been widely used in various applications including skin-like electronics [21], wearables [22,23,24], sensorized soft robots [25,

* The contents in this chapter have been published in [189], [97]

26,27,28,29].

However, improving the sensitivity of this mechanism has been limited. This is because the resistance change of the conductive liquid path is determined only by the strain. From the well-known equation $R = \rho L/A$, assuming the incompressibility and constant resistivity of the liquid, the resistance change of the liquid path under strain ϵ can be expressed as:

$$\frac{\Delta R}{R_0} = \frac{\Delta(L/A)}{L_0/A_0} = 2\epsilon + \epsilon^2. \tag{2.1}$$

The equation shows that the sensitivity cannot be tuned by changing materials or geometric parameters such as the area or the length of the conductive path, which is a dominant approach to enhance the sensitivity of many sensors.

To overcome this limitation, we suggest a different approach that modulates the non-uniform strain distribution along the length of the sensor. The distributed strain can be achieved by the multi-stiffness structure of the elastomer. The structure locally produces a larger strain compared to the conventional single-stiffness structure, which consequently amplifies the total resistance change due to the hyper-linearity of the sensor signals.

2.1.2. Overview

In the first subsection of this chapter, we will explain how this locally concentrated strain results in the enhanced sensitivity of the entire sensor structure by deriving a rigorous mathematical model that calculates the sensitivity in terms of the design parameters. Then, the test procedure and the results for validating the model will be presented throughout the two subsequent sections. Lastly, we discuss the potential design improvements and applications to take advantage of the enhanced performance of the sensor.

2.2. Theory

2.2.1. Introduction of two design parameters

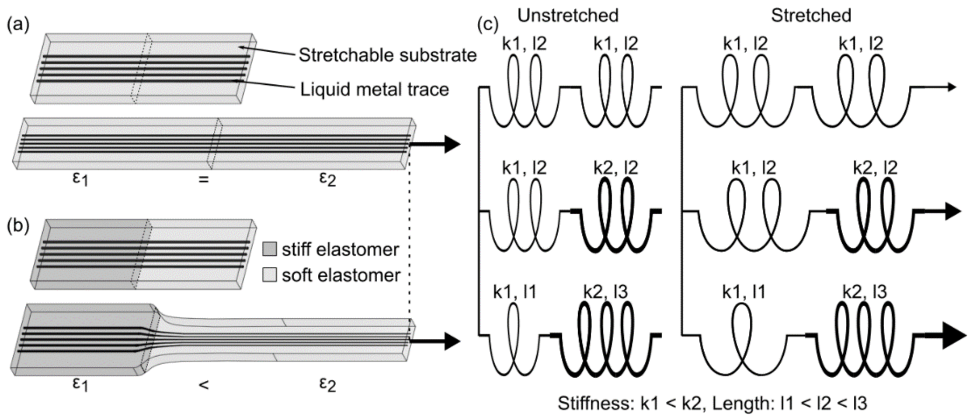

Figure 2.1. Comparison of single-material and multi-material sensors: (a) Deformation of a single-material sensor due to uniaxial tension, which produces uniform strain across the sensor; (b) Deformation of a multi-material sensor due to uniaxial tension. Each segment experiences distinct strains; (c) Three sets of springs in series, where stiffness and initial length distribution affect the final deformation.

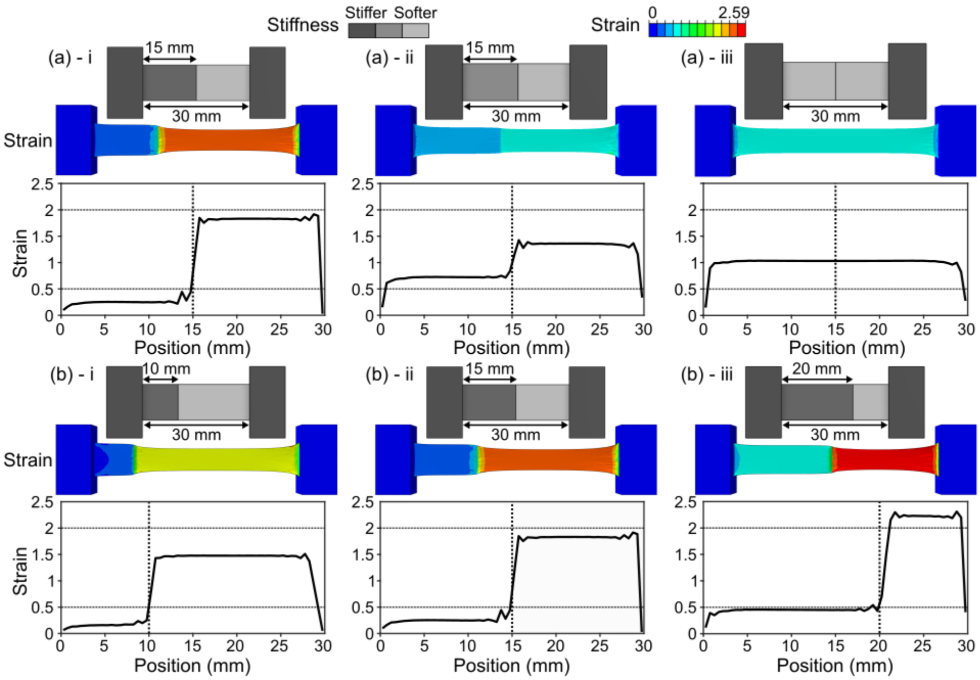

Figure 2.2. Deformation of multi-material sensors with design variations predicted by finite element analysis: Strains (y-axis) along the length of the sensor (x-axis) are plotted: (a) Sensors with various material combinations; the difference in the stiffnesses of the composing materials decreases from left to right. (b) Sensors with different length portions of a stiffer material (33%, 50%, 66%).

To model the geometrical effect-based soft strain sensor, the conductive path is considered as a set of finite numbers of small segments connected in series, embedded in the elastomer substrate as represented in **Figure 2.1a** and **2.1b**. Then, total resistance of the sensor can be calculated as the sum of the local resistances of the segments. Each of the local resistances is determined by the local strain. The modulation of these local strains can be achieved by altering the stiffness variation and the length portion of the elastomer segments, as depicted in **Figure 2.1c**. To prove this concept and investigate how these two factors affect the strain distribution, deformations of multi-material structures with varying material combinations (**Figure 2.2b**) and length portions (**Figure 2.2b**) were simulated using a commercialized finite element analysis software package (Abaqus, Dassault Systems).

In the simulation results, the strain contours of the deformed structure and the strain distributions along the lengths of the sensors are shown. In all designs, we observed that the strain applied to each material segment was almost uniform, which allowed us to model the multi-material sensor with an assumption of piece-wise constant strains over the lengths of the sensor. By comparing the three sensors shown in **Figure 2.2a**, we found that the larger differences in the stiffness of the materials lead to the greater differences in the strain levels between the two segments. More specifically, the differences in the strain levels decreased from approximately 1.58 to 0.64 and ended up approaching 0 as the difference in the stiffnesses of the two materials became smaller, as shown in **Figures 2.2a i – iii**. Increasing the portion of the stiffer material increased the strains in both material segments, as shown in **Figure 2.2b**, leading to an increase in the total resistance based on **Equation 2.1**.

2.2.2. Two-parameter analysis

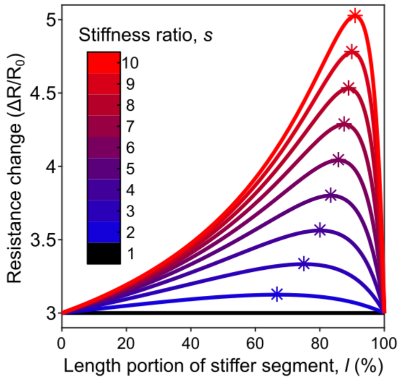

Figure 2.3. Resistance changes at 100% strain: The values were normalized by the initial resistances, i.e., sensitivity, for varied length portions of the stiffer segment and the stiffness ratios.

Governing equations and solution

For multi-material sensors, we assume that the geometry of the embedded conductive path is uniform in the undeformed state, regardless of the component materials. With a uniform cross-sectional area, the initial resistance of each material segment is determined only by its initial lengths. We then establish the total resistance of the multi-material sensors as the sum of the local resistances, each of which was calculated using **Equation 2.1**. Thus,

$$\begin{aligned} \frac{\Delta R}{R_0} &= \frac{R_{1,0}(2\epsilon_1+\epsilon_1^2)+R_{2,0}(2\epsilon_2+\epsilon_2^2)}{R_{1,0}+R_{2,0}} \\ &= \frac{R_{1,0}}{R_{1,0}+R_{2,0}}(2\epsilon_1+\epsilon_1^2)+\frac{R_{2,0}}{R_{1,0}+R_{2,0}}(2\epsilon_2+\epsilon_2^2) \\ &= \frac{l_{1,0}}{l_{1,0}+l_{2,0}}(2\epsilon_1+\epsilon_1^2)+\frac{l_{2,0}}{l_{1,0}+l_{2,0}}(2\epsilon_2+\epsilon_2^2) \end{aligned} \tag{2.2}$$

where the subscript 0 in the variables indicates the initial value before the sensor deformation, and the subscripts 1 and 2 represent the types of the materials in the different segments. Now, the total resistance change of a multi-material sensor can be expressed with second-order polynomials of the local strains as well as with the initial lengths of the segments. The local strains can be calculated by solving the geometric constraints and the force equilibrium of the sensor. The total strain (ϵ) of the sensor is geometrically related to the local strains by

$$l_{1,0}\epsilon_1 + l_{2,0}\epsilon_2 = (l_{1,0} + l_{2,0})\epsilon \tag{2.3}$$

Then, the tensile force equilibrium of the material segments connected in series needs to be satisfied. We first consider a simple case in which the materials follow the linear force—strain relation as

$$K_1\epsilon_1 = K_2\epsilon_2 \tag{2.4}$$

where K_1 and K_2 are the stiffnesses of the two materials. K_1, K_2, $l_{1,0}$, and $l_{2,0}$, used to express the constraining equations (**Equation 2.3** and **Equation 2.4**), can be further simplified to two parameters as

$$\begin{aligned} s &:= K_1/K_2 \in \mathbb{R}, \\ l &:= l_{1,0}/(l_{1,0} + \mathrm{l}_{2,0}) \in \mathbb{R}. \end{aligned} \tag{2.5}$$

by setting K_1 to be larger than K_2 without loss of generality. We denote s as the stiffness ratio between the two materials and l as the length portion of the stiffer material. A sensor with $l = 0$ or $l = 1$ indicates a sensor made of a single material to be entirely soft or stiff, respectively. If the sensor has a large s, the two materials forming the multi-material structure have a large difference in stiffness. Now, Eqs. (3) and (4) can be solved, and the local strains of the two material segments (ϵ_1, ϵ_2) can be expressed using the two parameters (s, l) and the total strain (ϵ) as

$$
\begin{aligned}
\epsilon_1 &= \frac{\epsilon}{s + l - sl}. \\
\epsilon_2 &= \frac{s\epsilon}{s + l - sl}.
\end{aligned}
\tag{2.6}
$$

By plugging these local strains into **Equation 2.2**, we can finally derive the total resistance change of a multi-material sensor in a closed form as

$$
\begin{aligned}
\frac{\Delta R}{R_0} &= l\left(\frac{2\epsilon}{s + l - sl} + \frac{\epsilon^2}{(s + l - sl)^2}\right) \\
&\quad +(1 - l)\left(\frac{2s\epsilon}{s + l - sl} + \frac{s^2\epsilon^2}{(s + l - sl)^2}\right).
\end{aligned}
\tag{2.7}
$$

Analysis

To understand the effects of the parameters s and l in **Equation 2.7**, the equations was plotted in **Figure 2.3** for a fixed input strain (ϵ) of 1 (100% of stretching from the initial length). Each curve represents a different material combination, showing the resistance change as the length portion varies. The flat curve ($s = 1$, black) is a single-material sensor, which is not affected by the changes of the length portion. However, for a large stiffness ratio with distinct materials forming the sensor, we see that the multi-material structure shows greater changes in resistance than does the single-material structure. We also note that the resistance change does not monotonically increase with the increase of the length portion, but rather, a peak exists in each curve (marked with an asterisk). This observation signifies the existence of the optimal length portion for each stiffness ratio. These optimal points can be computed by differentiating **Equation 2.7**. Given the stiffness ratio, the optimal resistance change ($\Delta R/R_o^*$) and the corresponding length portion (l^*) are calculated as

$$\frac{\Delta R^*}{R_o}(s,\epsilon) = \frac{\epsilon(\epsilon + 8s + 2\epsilon s + \epsilon s^2)}{4s}, \tag{2.8a}$$

$$l^*(s) = \frac{s}{1+s}. \tag{2.8b}$$

Lastly, we observed that the overall curve shifted upwards, and the peak rightwards, as the stiffness ratio (s) increased. Therefore, to enhance the sensitivity of a multi-material strain sensor, it is ideal to select materials with a stiffness difference as large as possible with the optimal length portion.

2.3. Experiments

2.3.1. Sensor fabrication and testing

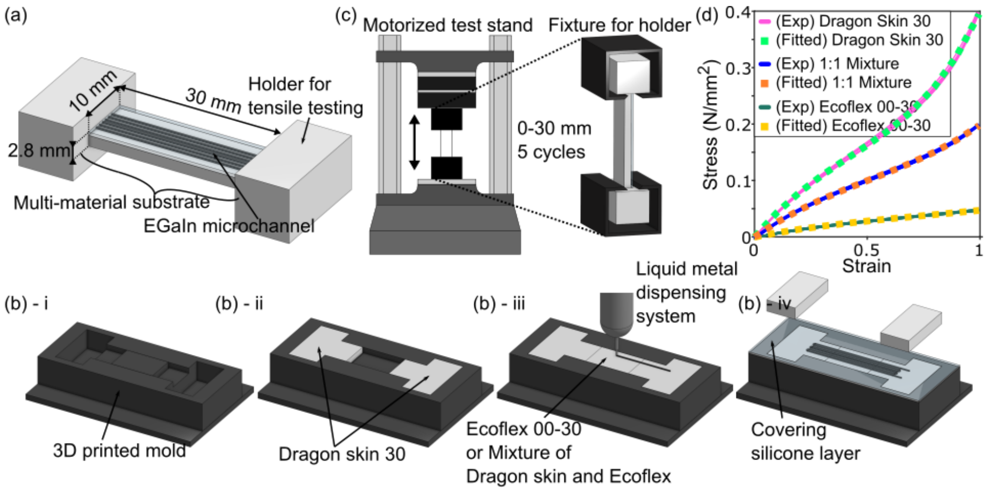

Figure 2.4. Overview of sensor prototyping and testing: (a) design, (b) fabrication process of the multi-material sensor, (c) experimental setup for the cyclic tensile test, and (d) hyperelastic Yeoh model characterization of the materials

used in the experiment. The solid and the dotted lines represent the measured and fitted stress data, respectively.

Sensor design

To investigate the effect of the stiffness ratio on the multi-material sensors, two different stiffness ratios (i.e., two different combinations of silicone materials) were used: a combination of Ecoflex 00-30 (100% modulus: 69 kPa, Smooth-on, Inc.) and Dragon Skin 30 (100% modulus: 593 kPa, Smooth-on, Inc.), and a combination of Ecoflex 00-30 and a 1:1 mixture (mass ratio) of Ecoflex 00-30 and Dragon Skin 30, which we will denote as Ecoflex Ecoflex-DragonSkin mixture. For each combination, sensor samples with seven different length portions were fabricated with the stiffer fabricated occupying 0%, 33.3%, 50%, 66.7%, 83.3%, and 100% of the total length.

The dimensions and the fabrication process of the multi-material sensors are summarized in **Figures 2.4a** and **2.4b**. Plastic molds were prepared by 3D-printing and assembled so that two different silicone materials could be cured one after the other. After preparation of all the molds, liquid-state Dragon Skin 30 was poured into the mold and cured. The remaining space was then filled with Ecoflex 00-30 and cured. Using a motorized *x*-*y* stage (Shotmaster 300ΩX, Musashi), a pneumatic dispensing system (SuperΣ CMIII V2, Musashi), and a laser distance sensor (LK-G32, Keyence), liquid-metal (eutectic gallium-indium, eGaIn) traces were printed on the top surface of the cured silicone. Reliable and efficient fabrication of eGaIn traces was achieved [30,31] by controlling the thickness of the liquid metal using the dispensing pressure, the stand-off distance, the stage velocity, and the shot time [32,33]. The printed eGaIn traces were then encapsulated by a thin layer of the Ecoflex-DragonSkin mixture. A block of Dragon Skin 30 was also cured on each end of the sensor as a holder combined with a custom-built fixture during testing. For fabrication of the samples with the other stiffness ratios, the entire procedure was repeated except for replacing the stiff material (Dragon Skin 30) with the Ecoflex-DragonSkin mixture.

Experimental setup

The resistance and the tensile force of the multi-material sensor samples were measured during uni-axial tensile tests. Each sensor was fixed on a motorized stand (ESM 303, Mark-10) (**Figure 2.4c**). The seven samples were tested for each length portion, and all the sensors were stretched up to 100% strain prior to the main experiment accounting for the Mullins effect [34,35]. For tests involving displacements smaller than 0.1 mm, a universal material testing machine (34C-1, Instron) was used with the same experiment.

2.3.2. Elaborated force-strain relation

There are limitations in directly applying **Equation 2.4** and consequently **Equation 2.7** to actual soft sensors for validation of the proposed model. We previously employed a simplified linear force—strain relationship in order to discuss the parameter of the stiffness ratio as a single variable s. In this way, we can obtain the intuition on the effects of the two parameters on the behavior of the multi-material sensors. However, the simplified relation does not reflect the true nature of silicone materials in general. Therefore, we adopted the hyperelastic

Yeoh model into the previously described theories for accurate prediction of the behavior of the tested samples instead of using the simplified relationship. The Yeoh model is considered to be suitable in interpreting the sensors made of silicone materials, since they experience local strains ranging from 0 to 300% during the tensile test [36,37].

The third-order Yeoh model suggests that the tensile force (F) can be expressed with the stretch (λ) and the three material constants ($C_1,\ C_2,\ \mathrm{C}_3$) as

$$F = 2A_0\left(\lambda - \frac{1}{\lambda^2}\right)\sum_{i=1}^{3} iC_i\left(\lambda^2 + \frac{2}{\lambda} - 3\right)^{i-1}. \tag{2.9}$$

Using this relation, the force equilibrium in **Equation 2.4** can be rewritten as

$$\begin{aligned} &2\left(\lambda_1 - \frac{1}{\lambda_1^2}\right)\left(C_{1,1} + 2C_{1,2}(I_1 - 3) + 3C_{1,3}(I_1 - 3)^2\right) \\ &= 2\left(\lambda_2 - \frac{1}{\lambda_2^2}\right)\left(C_{2,1} + 2C_{2,2}(I_2 - 3) + 3C_{2,3}(I_2 - 3)^2\right), \end{aligned} \tag{2.10}$$

where $\lambda_k = \epsilon_k + 1,\ I_k = \lambda_k^2 + 2/\lambda_k$, and (C_1, C_2, C_3) representing the three Yeoh coefficients of the kth material.

Then, given the Yeoh coefficients and the length portion l, the local strain of each segement in a multi-material structure is calculated by solving **Equation 2.1** with **Equation 2.3**. The calculated local strains are then plugged into **Equation 2.2** and (1) to quantify the sensitivity and the force associated with each sensor.

The force—strain curves of the three silicone materials used for fabrication (Ecoflex 00-30, Dragon Skin 30, and a 1:1 mixture of the two silicone) were fitted with **Equation 2.9** to obtain the corresponding Yeoh coefficients of the material (**Figure 2.4d**). The plots show that the stiffness of the mixed material is approximately the average of the two pure materials. The calculations of the model and the experimental results will be discussed in detail in the following section.

2.4. Results

2.4.1. Enhanced sensitivity and optimal length portion

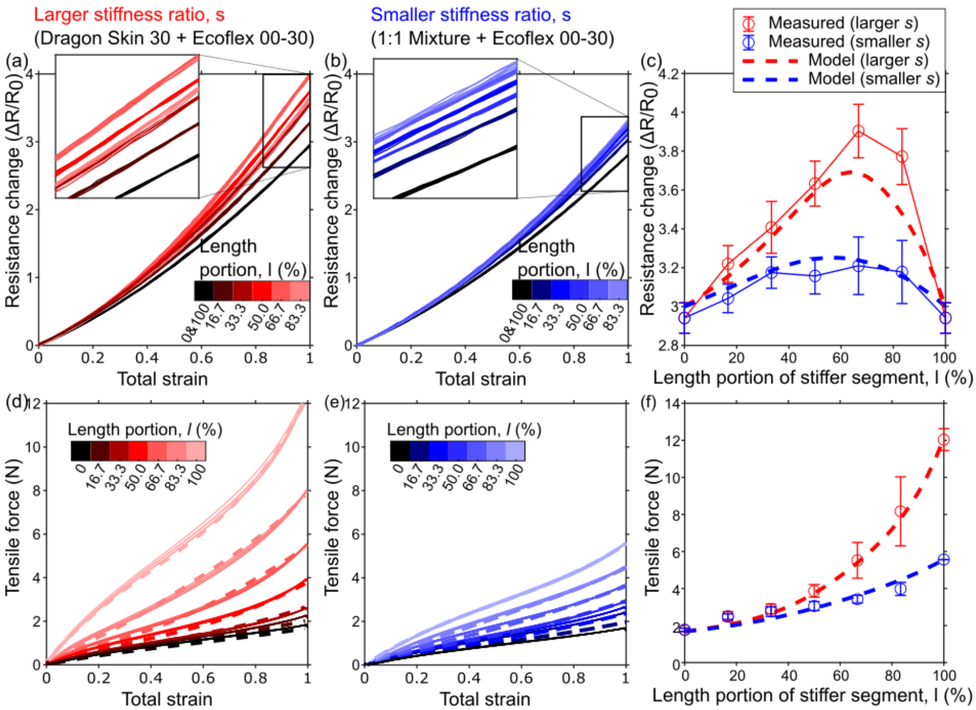

Figure 2.5. Resistance changes and tensile forces of multi-material sensors with various design parameters: (a) Resistance curves of sensors with the high stiffness ratio (i.e., combination of Dragon Skin 30 and Ecoflex 00-30). (b) Resistance curves of sensors with the low stiffness ratio (i.e., combination of Ecoflex-DragonSkin mixture and Ecoflex 00-30). The shades of the color indicate different length portion, with the brighter shades representing larger portions of the stiff segment. (c) Model predictions (dotted lines) from Section 2.3.2 and measured resistance (circular markers) at 100% strain (data points at strain =1 in (a) and (b))

plotted with respect to length portions. The length portions are expressed in x-axis. Error bars were calculated with seven samples of each sensor design. (d) Tensile force curves of sensors with the high stiffness ratio. (e) Tensile force curves of sensors with the low stiffness ratio. (f) Model predictions (dotted lines) from Section 2.3.2 and measured tensile forces (circular markers) at 100% strain (data points at strain =1 in (d) and (e)) plotted with respect to length portions.

Figure 2.5a and **2.5b** show the resistance changes of the sensors with seven different length portions. **Figure 2.5a** shows the results from the sensors with higher stiffness ratios (Dragon Skin 30 + Ecoflex 00-30) than those in **Figure 2.5b** (Ecoflex-DragonSkin Mixture + Ecoflex 00-30). The curves were plotted with respect to the total strain ranging from 0 to 1.

In both material combinations, i.e., **Figures 2.5a** and **2.5b**, all the multi-material sensors (colored in red or blue) demonstrated higher resistance changes than the single-material sensors (black). However, the response curves varied among the sensors with different length portions. A more detailed comparison is depicted in **Figure 2.5c** that marks each sensor's resistance change at a total strain of 100% ($\epsilon = 1$), equivalent to the gauge factor. Each marker represents the last data point of the curve in **Figures 2.5a** and **2.5b**, plotted with respect to the length portion. The two solid line curves, connecting these markers, are both bell-shaped, with the minimum values at 0 and 100% length portion, representing single-material sensors. The bell-shape proves that the multi-material sensors are superior in sensitivity to the single-material sensors, showing enhancement in sensitivity up to 33% and 9% for the two material combinations. Furthermore, the peaks in the curves in **Figure 2.5c** suggests the existence of the optimal length portion. This observation extends the conclusions drawn in the mathematical analysis in the previous section to include even general cases of soft sensors, confirmed through the actual prototypes composed of hyperelastic materials.

Overall, the observations on the distinct level of improvement in sensitivity between the two stiffness ratios and on the existence of the optimal length portion concur with the modeling in **Figure 2.3**. However, for more sophisticated and accurate evaluation of the sensor model, the comparison of the experimental results with the theoretical predictions was elaborated through the hyperelastic force—strain relation in Section 2.3.2. The prediction is shown with the dotted line curve in **Figure 2.5c**, whose shape and relative location of the peak are in agreement with those of the experimental results. This result confirms that we can accurately predict the improvement in the sensitivity, given its length portion and the material properties (i.e., Yeoh coefficients).

2.4.2. Trade-off between sensitivity and softness

Figures 2.5d, **2.5e**, and **2.5f** illustrate the tensile forces measured during stretching and releasing of the sensors. It is apparent that increase in length portion leads to larger tensile forces, since the stiffer material occupies the major portion of the total structure. In addition, particularly in this experiment, larger tensile forces were observed in the sensors with high stiffness ratios in **Figure 2.5d** than those with low stiffness ratios in **Figure 2.5e**. This is because the stiffer material (Dragon Skin 30) was used to create the larger stiffness ratio. However, increase in the stiffness ratio does not necessarily increase the overall stiffness. For example, using a material combination of Ecoflex-DragonSkin mixture and a material softer than Ecoflex 00-30 will have a higher stiffness ratio while showing a smaller overall stiffness compared to the sensors in **Figure 2.5e**. This means a sensitive yet soft sensor can be designed—an idea that will be discussed in detail in Section 6.

2.4.3. Higher resolution

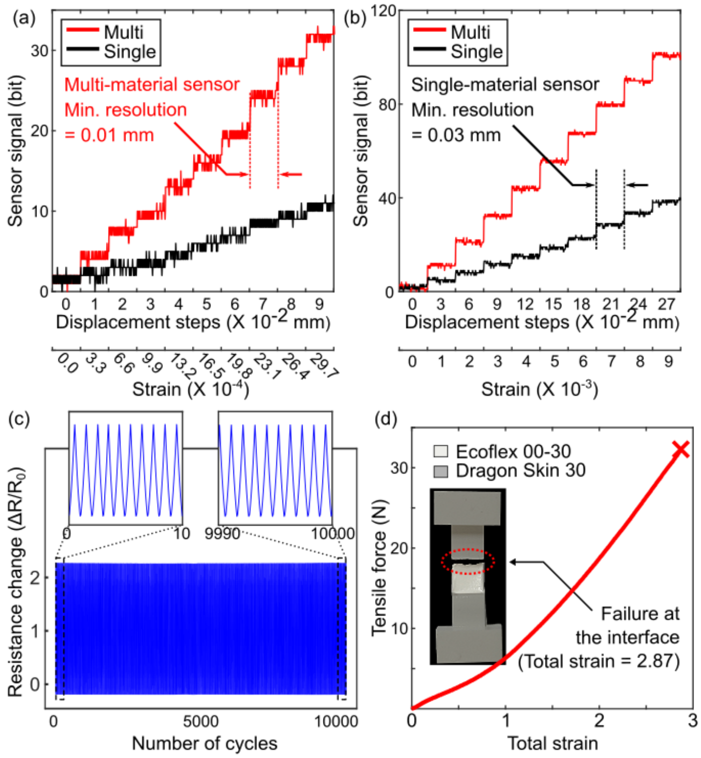

Figure 2.6. Resolution and durability of the multi-material sensor: (a) Sensor signals (digital bits) of the multi-material sensor with the highest sensitivity, in **Figure 2.5**, (composed of Dragon Skin 30 and Ecoflex 00-30 with 66.7% length portion) and a single material sensor stretched with an increment of 0.01 mm. (b) Sensor signals (digital bits) of the sensors stretched with an increment of 0.03 mm. (c) Sensor signal (resistance change) of a multi-material sensor designed with the material combination of Ecoflex 00-30 and an Ecoflex–DragonSkin mixture, and the 50% length portion, stretched up to 100% strain over 10000 cycles. (d) Tensile test result of the multi-material sensor with the highest sensitivity

(66.7% length portion).

Enhancement of the sensitivity due to the multi-material structure led to an increased resolution with a high signal-to-noise ratio. The multi-material sensor with the highest sensitivity, observed in **Figure 2.5c**, and a single-material sensor were stretched with increments of 0.01 mm and 0.03 mm, as shown in **Figures 2.6a** and **2.6b**, respectively. The signals were obtained using a 16-bit analog-to-digital converter (ADS 1115, Texas Instruments) with the maximum gain of 16. The results in **Figure 2.6a** demonstrates that the multi-material sensor was able to clearly detect each 0.01 mm displacements while the signal changes of the single-material sensor was not distinguishable from the noise. The highest resolution of the single-material sensor was 0.03 mm in **Figure 2.6b**, significantly larger than that of the multi-material sensor.

2.4.4. Linearity, dynamic durability, maximum strain, hysteresis and bandwidth

Table 2.1. Nonlinearity of sensors with various design parameters: The values were evaluated by the percentage of deviation (error) from the best fit line to the full scale output (FSO) of the sensor.

Stiffness ratio	High (Dragon Skin 30 + Ecoflex 00-30)						Low (Mixture+ Ecoflex 00-30)					
Length portion (%)	0&100	16.7	33.3	50.0	66.7	83.3	0&100	16.7	33.3	50.0	66.7	83.3
Nonlinearity (%FSO)	6.8	5.9	7.3	6.3	7.2	6.8	7.5	6.1	7.9	6.8	8.3	8.0

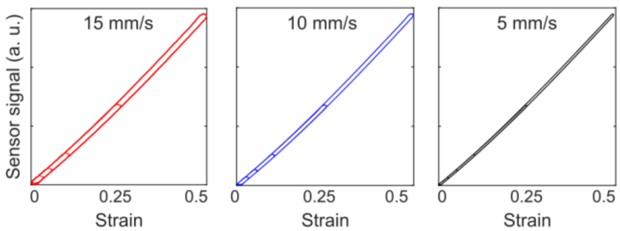

Figure 2.7. Sensor hysteresis and bandwidth: Sensor signals of the multi-material sensor

measured at various elongation rates (5, 10, 15 mm/s).

Multi-material sensors exhibited small and uniform nonlinearity (calculated with the error from the best fit line [38]), as described in **Table 2.1**, an attribute of their sensing mechanism (See **Equation 2.1**), independent of the stiffness ratio and the length portion. Furthermore, **Figure 2.6c** shows the sensor signals of a multi-material sensor composed of Ecoflex—DragonSkin mixture and Ecoflex 00-30 with a 50% length portion during 10,000 stretching-releasing cycles with 100% strain. The consistent output signal proves that the multi-material design was highly durable under long-term dynamic loads. The results prove that the multi-material structure did not undermine the advantageous characteristics of the geometry-based fluidic sensors in terms of linearity and dynamic durability. **Figure 2.6d** shows the result of a tensile test of the multi-material sensor with the highest sensitivity in **Figure 2.5c**. The maximum measurable strain was 2.87, at which the sensor was fractured. A mechanical failure occurred at the interface between the stiff and soft materials, caused by large stress concentrations induced by the abrupt change in the cross-sectional area [39,40]. Potential improvements of the interface design to enhance the structural integrity and the measurable strain range of the multi-material sensors will be discussed in the next section. **Figure 2.7** shows the level of hysteresis according to various elongation rates (5, 10, 15 mm/s), which increases as the sensor is stretched faster. This is a typical phenomenon observed in viscoelastic materials which becomes another research topic to further enhance the performance of the sensor. On the other hand, the magnitude of the output sensor signal, or the bandwidth, remained consistent regardless of the speed.

2.5. Discussions

2.5.1. Design improvement for symmetry and conformity

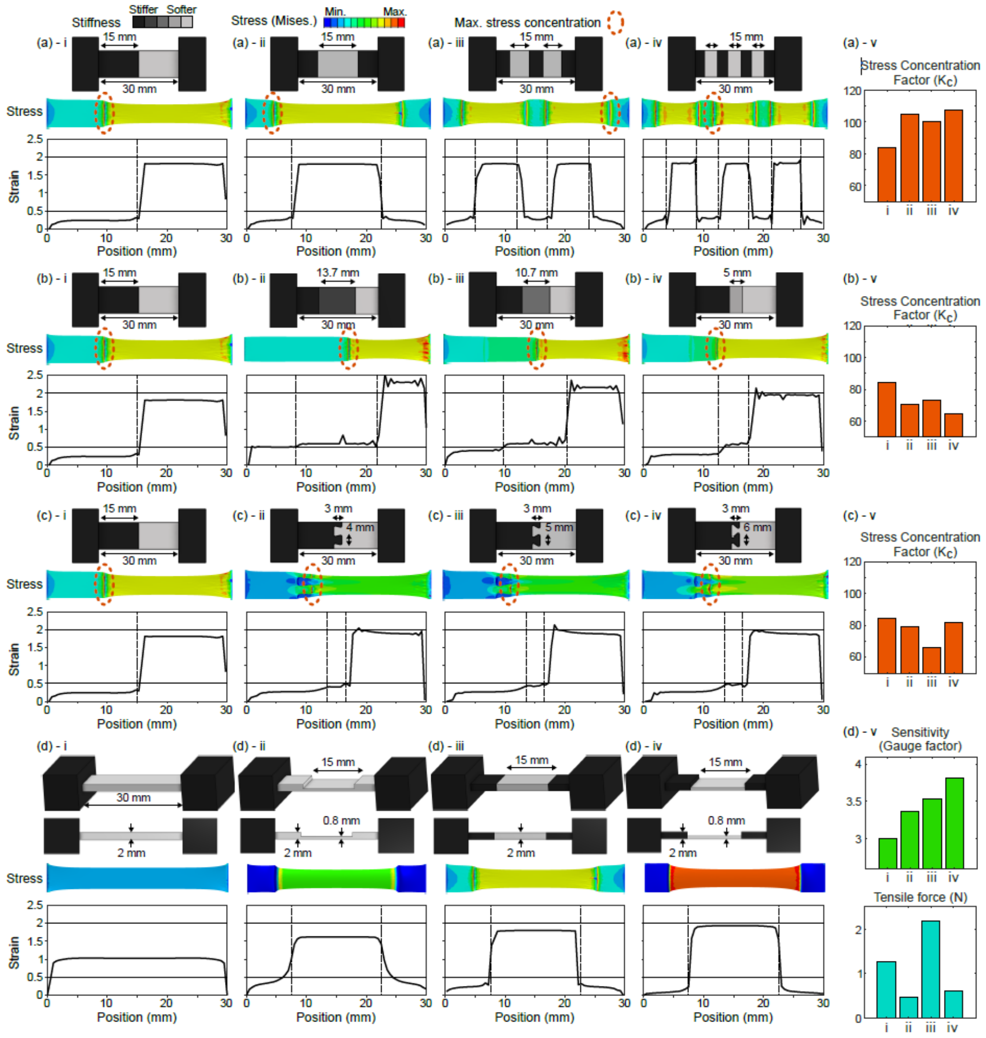

Figure 2.8. Finite element analysis of various designs of multi-material sensors: The stress contours and the strain distributions at 100% strain are illustrated. For comparison of the stress concentration factors, all the sensors in (a)–(c) are designed to have the same sensitivity but with (a) varied numbers of material interfaces, (b) additional intermediate material segment whose stiffness is interpolated at the 1/6, 1/3, 1/2 point from the stiff to soft material for ii–iv, respectively, and (c) increased interfacial area from 1x to 1.8x using a

jigsaw pattern. Sensitivities and tensile forces are compared between single- and multi-material sensors with thickness variations in (d).

Looking back at **Figure 2.2**, it is noted that the asymmetric and non-uniform span of the stiffness of the component materials causes irregular deformation and abrupt changes in the cross-section when stretched. Asymmetric deformation hinders the conformity of the sensor to a large deformable surface, such as the joints in the human body, and sudden reduction in the cross-section induces stress concentration.

Figure 2.8 shows the results of finite element analyses of various designs of multi-material sensors with (a) varied numbers of material interfaces, (b) additional material at the interface, (c) increased area of the interface, and (d) thickness variations. Despite the different designs, the overall strain plots show that the segments of the same material still experience uniform and equal strain levels. This approves that the assumptions behind Eqs. (3)—(7) can also be applied to the new designs. Using these findings, all the sensors in **Figures 2.8a, 2.8b, and 2.8c**, were designed to have constant sensitivities for a more objective assessment of their structural integrity.

The sensors in **Figures 2.8a-ii—iv** shows symmetric and uniform deformations for better conformity to the host structure, while sharing the same stiffness ratio and the length portion with the sensor in **Figure 2.8a-i**.

However, increasing the segmentation of the component material intensifies the stress concentration at the interfaces, marked in the stress contour plots. **Figure 2.8a-v** graphs the stress concentration factor of each sensor, K_c, defined as

$$K_c = \frac{\sigma_{max}}{\sigma_{nom}}, \tag{2.11}$$

where the maximum stress (σ_{max}) occurs at the material interfaces and the nominal stress (σ_{nom}) is the average uniform stress [41]. Sensors with more material interfaces (**Figures 8a-ii-iv**) generally show higher stress concentration factors at the interfaces. This may be critical to the sensor integrity, as shown in **Figure 2.6d**, where a mechanical failure was observed at the material interface, limiting the sensor's maximum strain.

2.5.2. Design improvement for structural integrity

The following two designs can alleviate stress concentration at the material interfaces. The simulation results of the first design are shown in **Figure 2.8b**, in which we introduce an additional material with an intermediate stiffness at the interface, as was done by Bartlett et al. [42]. The stiffness of the interfacial material was selected by linear interpolation of the Yeoh coefficients of Ecoflex 00-30 and Dragon Skin 30, at the 1/6 (ii), 1/3 (iii), and midpoint (iv) from Dragon Skin 30. For each case, the lengths of the material segments were adjusted to produce the same sensitivity. This gradation of the stiffness caused a more gradual distribution of stress along the length of the sensor, and decreased the stress concentration factor (**Figures 2.8b-v**). The second design (**Figure 2.8c**) was inspired by the work by Mengüç et al. [22], which increased the area of the material interface using a jigsaw geometry. We also observed a significant decrease in the stress concentration factor in sensors with a larger interface area than that of the original design (**Figures 2.8c-v**). These enhancements at the material interface will allow multi-material sensors to endure larger strains before failures.

2.5.3. Design improvement for softness

The multi-material approach to enhancing sensitivity, as discussed with **Figures 2.5**, may induce increase in overall stiffness when stiff materials are employed. Also, at the interface between the different materials, there are higher chances of mechanical failures due to the high stress concentration, as observed in **Figure 2.6d** and **Figures 2.8a—c**. To Avoid these problems, using a single material but varying its thickness can be an alternative way to create the non-uniform strain distribution. As shown in **Figures 2.8d-i, ii and v**, the segments with different thicknesses of the same material behave like distinct material segments. The thin segment works as a soft material while the thick segment works as a stiff material, demonstrating a higher sensitivity than the single-material sensor with a uniform thickness. Furthermore, combining the thickness variation with the multi-material structure, as shown in **Figures 2.8d-iv**, may lead to even a higher sensitivity and also a drastically lower stiffness than a simple single- or multi-material sensor with a uniform thickness (**Figures 2.8d-i, iii**).

2.5.4. Literature study: Strain sensor-based finger tracking technologies

The high sensitivity and softness of the proposed sensor structure can contribute to tracking human motion which especially requires high resolution for measuring sophisticated movements. First of all, here, we will enumerate various strain-sensing mechanisms for tracking finger (hand) motions and compare the maximum strains and gauge factors of them. As in **Table 2.2**, diverse transducing materials and designs have been used, such as liquid metal microchannels, conductive fabrics, carbon particles embedded in silicone, and thin metal films. Generally, a mechanism with a larger maximum strain, i.e., more softness of the structure, has a smaller gauge factor, i.e., sensitivity. It can also be observed that our proposed multi-material sensor shows enhanced sensitivity compared to the results from the sensors with the same sensing mechanism but with conventional single-material structure [46]. In [46], a benchtop experiment was conducted to figure out the maximum stretch of the skin near the finger joints (~1 cm long) during the flexion motion, which was about 29% of its original length. To measure this small deformation with high precision, high sensitivity and resolution are required, which can be achieved by the multi-material sensors.

Table 2.2. Strain sensing-based finger tracking technologies

Ref No.	Sensing mechanism	(Reported) Maximum strain	Gauge factor
[43]	Capacitive (Conductive fabric + Silicone)	1.2	1.23
[44]	Resistance (EGaIn microchannel)	1	N/A
[45]	Resistance (Gallium metal film)	0.5	1.6
[46]	Resistance (EGaIn microchannel)	0.45	1.48
[47]	Resistance (Conductive fabric + Silicone)	0.36	2.8
[48]	Resistance (Carbon particles + PDMS)	0.06	18
[49]	Resistance (Conductive fabric)	N/A	*2.76
Ours	Resistance (EGaIn microchannel)	2.87	3.9

*Estimated value assuming strain of 0.29 at maximal flexion [46].

2.5.5. Potential application to hand-tracking devices

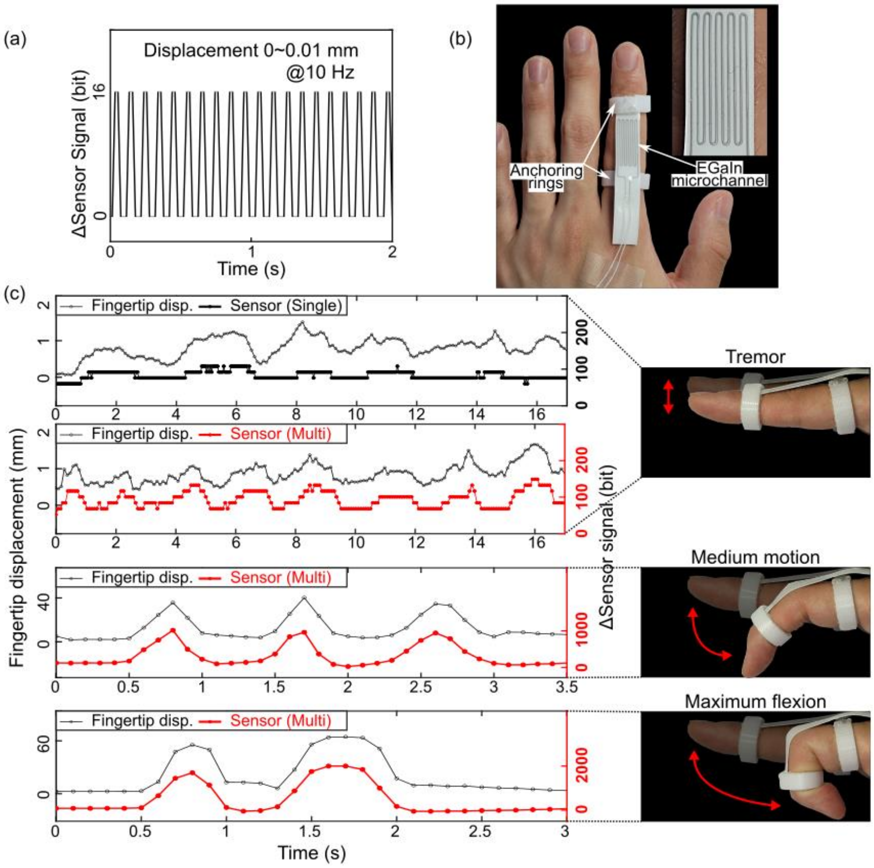

Figure 2.9. Multi-material sensors for measuring finger movements: (a) Multi-material sensor signal (digital bit) subject to cyclic stretching and releasing of 0.01 mm displacement (its highest resolution) at 10 Hz. (b) Multi- or single-material sensor prototype mounted on the proximal interphalangeal joint. (c) Sensor signals obtained during various finger motions. From top to bottom: single material sensor readings (black) for fine finger motions similar to tremor, multi-material sensor readings (red) for flexion/extension motions from a small to the maximum ranges.

Involuntary finger motions, known as tremor, is present in all people. The average resting tremor of a young healthy individual (aged 20—30) is 0.1 mm ± 0.1 mm at frequencies lower than 10 Hz [50]. We demonstrate the ability of multi-material sensors to measure the wide range of finger motions with an exceptional precision that can even detect the tremor. The sensor is placed on the index proximal interphalangeal joint of a male human hand, and the strain caused by the rotation of the joint is measured. The distance from the joint to the fingertip and the radius of the joint were measured to be 49.1 mm and 7.6 mm, respectively. With these measurements, the displacement by the strain at the joint caused by the fingertip displacement of 0.1 mm was estimated as 0.015 mm, which was not detectable by the conventional single material sensor, as found in **Figure 2.9**.

To verify that the sensor can perform reliably at the frequency of the tremor, a multi-material sensor that exhibited the highest sensitivity in **Figure 2.5c** (composed of Dragon Skin 30 and Ecoflex 00-30 with a length portion of 66.7%) was subject to cyclic stretching and releasing with an amplitude 0.01 mm at a frequency of 10 Hz. The results, in **Figure 2.9a**, demonstrate that the multi-material sensor still maintains its highest resolution of 0.01 mm during high frequency motions, such as tremor.

The selected multi-material sensor and a single-material sensor were mounted on the joint, as depicted in **Figure 2.9b**. Their signals were recorded for the flexion and extension motions with the maximum and a slightly reduced ranges and also the fine finger motions that mimicked the tremor. The reference fingertip positions were also tracked by post-processing the recorded videos with a motion analysis software (ProAnalyst, Xcite). The results in **Figure 2.9c** clearly demonstrate that the multi-material sensor signals (colored in red) successfully reflected the fingertip displacements as large as 58.4 mm and as small as 0.2 mm, whereas the single-material sensor failed to distinguish the small displacements.

Chapter 3

Glove-based Hand Pose Reconstruction*

3.1. Introduction

3.1.1. Motivation

Dexterity and versatility, clear distinctions of the human hand from those of animals, allow myriad functions ranging from grasping [51,52] to in-hand manipulation and even to means of communication using hand gestures [53,54]. Tracking and reconstruction of the hand articulation is, therefore, a popular topic of research with numerous applications for human-robot interactions. However, there have been many challenges in estimating hand motions, as the human hand is a complex body part with many degrees of freedom (DoFs) and shows large variations between individuals. Many prior studies have demonstrated the classification and reconstruction of hand poses [55,56,57,58,59], albeit within a limited scope, achieving only rudimentary results. Such performances may not be sufficient for applications, such as the teleoperation of surgical robots [60], control of anthropomorphic robot hands [61], and clinical analysis [62], which demand precise localization of the fingertips and detailed posture of the hand. To replicate these hand

* The contents in this chapter was partially in collaboration with Prof. Sumin Koo (Yonsei University).

motions, it is essential to identify the hand configuration, which is characterized by both the kinematic structure and the joint motions [63]. Consequently, the accurate quantification and measurement of these two components hold significant importance. In this chapter, we will first review the existing hand tracking systems in terms of the choice of the sensing and reconstruction method, dimension reduction, and online kinematic parameter estimation, which are the techniques that contribute to the accuracy of the tracking. Then, we will suggest a wearable-type hand tracking system that uses a strain sensing mechanism to simultaneously estimate the two components, followed by analyzing and assessing the system in the perspective of the three aforementioned techniques.

3.1.2. Background and literature study

Various sensing and reconstruction methods

To quantify the joint motion, some prior studies have employed strain/bending sensors, encoders, or inertial measurement units (IMUs) to directly measure the joint angles or the bone rotations [64,65,66,67]. As a counterpart, vision or magnetic sensors have been used to track specific features of the hand, such as fingertips [57,68]. The measured quantities from either of these approaches then can be used to reconstruct the hand configuration through the forward kinematic (FK) or the inverse kinematic (IK) models, respectively, combined with the kinematic structures. To identify the kinematic structures, some studies have utilized vision-based techniques [69,70] or manual measurements [71,72] to estimate the bone lengths. However, these methods of measurement require highly controlled environmental setups as they are susceptible to factors, such as orientation, occlusions, or expertise of the examiner, limiting the wearer's free hand motions in various environments. In contrast, others have adopted a more simplified approach by applying the average bone lengths to all subjects/users rather than the personalized parameters [61]. However, the use of the average values may yield large errors in FK or provide multiple or no solutions in IK [73,74]. To mitigate these issues, some studies have proposed the application of complex kinematic constraints to hand motions [75,76]. However, this approach requires heavy computation and may inadvertently exclude potential solutions. Table 3.1 summarizes the characteristics and potential weaknesses of the reconstruction methods for wearable-type hand-tracking systems. While some of these issues can be addressed through the integration of multiple sensing mechanisms, this inevitably results in bulky and restrictive systems with reduced wearability [77]. Therefore, there continues to be a significant demand for a hand-tracking system that overcomes these limitations in terms of accuracy, robustness, and wearability.

Table 3.1. Comparison between various sensing and reconstruction methods for hand pose estimation

Reconstruction method	Forward kinematics	Inverse kinematics	Rigid body rotations
Measurements (Dimension)	Joint angles (20)	Fingertip position (15) and orientation (15)	Bone rotations (45)
Sensing mechanism	Strain-based or Bending-based sensors	Camera or magnetic sensors	Camera, IMU
Compactness and compliance	Compact and soft	Compact and rigid	Bulky and rigid
Physical interference	High	Low	Medium
Potential disturbances	Physical contact and stretch	Occlusion or magnetic interference	Occlusion or magnetic interference
Potential reconstruction failure	Fail-proof (robust)	Existence of solution, smoothness of pose	Unnatural motion for redundancy
Requirements for additional sensors in kinematic	Required for bending sensors, Not required	Required for magnetic sensors, Not required for	Required

parameter estimation	for strain sensors	cameras	
References	[64,65,66]	[57,68]	[67, 77]

Dimension reduction for hand coordinate

We also have to determine how to quantitatively express the diverse and complex hand poses. Among the infinite number of mathematical representations, in this chapter, we are focusing on the joint angle coordinate, which is an anthropomorphic representation. In this subsection, the reason for the selection is first discussed, and then we enumerate the previously published methods to measure or calculate the joint angles of human fingers.

The joint angle coordinate was selected in consideration of the efficiency, completeness, and potential need for post-processing. As most of the previous studies on hand configuration model it as 21 degrees of freedom system excluding the wrist motion, the minimum number of dimensions would be 21. If the representation is redundant, heavier computation is required in general, which possibly limits the performance. On the other hand, it has been known that hand movements can be represented using a smaller number of sets of coupled joint motions, called synergies [78, 79]. Although it is important to consider the biomechanics of human hands, still the theory is not completely established and it is impossible to fully express the complicated hand motions using the small number of synergies. It has been shown that the information of the hand synergies is more well extracted in the joint angle coordinate system (of flexion and abduction finger motions), since it is more anthropomorphic, compared to the Cartesian coordinate system (of bone or joint positions); And consequently, it is more robust to reconstruct bio-mechanically plausible motions [78, 79]. Therefore, we decided to use the joint angles to collect the ground truth motions and calibrate the developed system, which inherently includes the synergy of natural hand motions and can be utilized for further studies in reduced dimensions.

To directly measure the ground truth joint angles is challenging, especially while a person is moving its hand. Instead, [80] proposed a method to calculate the joint angles out of the input hand images using the trained model with the data collected from a commercial data glove [81]. This method can be simply implemented with only 2d image inputs without using bulky hardware but lacks accuracy and produces large variations in performance depending on the poses and relative angles to the camera. [82] attached retroreflective markers on each finger joint to track the vectors representing finger bones in Cartesian coordinates. They then calculated the projection angles of the vector onto the orthogonal planes in local frames and assumed two of them as flexion and abduction angles. With the same measurements, [83] first projected the vectors onto the orthogonal plane to the finger roll and then assumed that the two non-zero Euler angles as flexion and abduction angles. As can be implied from the fact that these two studies solved the same problem of finding the two angles in different methods, both of the solutions are not the exact solution and there always exist bounded errors. Furthermore, there exists additional uncertainty that comes from the marker localization error of the rotation center and from the skin stretch. [84] measured SO(3) of each bone and defined a cost function to minimize which measures error between the target and the estimated SO(3) using the relative rotation between them. However, this was limited to only one degree of freedom. In the following subsections, another approach to collecting the joint angles during the hand motion, which tries to overcome the aforementioned limitations, will be suggested.

Online kinematic parameter estimation

Table 3.2 distinguishes the published hand-tracking methods according to the identification or estimation strategies of the kinematic parameters. While direct measurement of the kinematic parameters [68,69,70,71] is more accurate compared to indirect measurement [77], they still have limitations for real-time update (correction) or simple experimental setup. As commercial systems, Manus gloves [15,61] use average values of bone lengths for medium-sized hands resulting in poor fingertip position estimation, while Leap Motion Controllers [14] use vision-based direct measurement of joint positions showing large errors depending on orientation to the camera [45]. Aside from these systems, most of the existing systems did not make an effort to estimate the kinematic parameters since they only demonstrated their performance for a specific user.

Table 3.2. Comparison between kinematic parameter identification or estimation strategies of various hand tracking systems

	Measurement	Accuracy	Real-time update	Experimental setup	Ref. no.
No measurement	N/A	Low	No	Easy	N/A
Direct measurement	Measuring bone lengths in advance	High	No	Laborious	[70],[71]
	Tracking markers on finger joints	High	Yes	Laborious and expensive	[68],[69]
Indirect measurement	Measuring stretch of wearable glove	Low	Yes	Depending on sensing mechanisms	[77], Ours

3.1.3. Overview

In this research, we propose a wearable glove capable of real-time estimation of the wearer's finger bone lengths and joint angles with high accuracy, all achieved through a single sensing mechanism. The glove system is calibrated and evaluated using *comprehensive* hand motion data that reflect the wide range of natural human hand motions. Furthermore, our reconstruction method provides a simple yet robust approach to hand pose reconstruction, regardless of the complexity of the hand motions, suitable for various applications. Below, we outline the key features and the contributions of our glove system.

First, the system uses a single strain sensing mechanism to estimate both the wearer's kinematic parameters (i.e., bone lengths) and joint motions (i.e., joint angles) that define the hand pose. This is enabled by the highly stretchable and flexible characteristic of the soft strain sensors used in this study. The soft strain sensors can be pre-stretched to fit the hand of the wearer and then be further deformed easily by joint movements. Therefore, the sensor signals simultaneously provide information on both the bone lengths and the joint rotations. As a result, once the glove is worn, it can immediately start tracking and reconstructing the wearer's hand without the need for any prior measurements or calibration for personalization. To the best of our knowledge, this is the first system capable of simultaneously estimating both the kinematic parameters and the joint motions using a single proprioceptive sensing mechanism. Consequently, our system not only demonstrates a compact design but also exhibits consistent performance, unaffected by factors like position, orientation, or environmental limitations, making itself a truly wearable system.

Second, the calibration and evaluation of our glove system rely on a comprehensive set of ground truth data, which represents the unconstrained and diverse hand motions expressed in the universal joint coordinate. This differentiates our system from the previous studies that evaluated their systems only for limited experimental conditions and users. For example, the strain-based tracking system was evaluated with the data obtained from the static motions of a hand replica [55], and the vision-based system was tested only for restricted hand motions confined to a customized stage [85]. Another approach with vision used datasets of fingertip positions, highly dependent on the specific kinematic structure, and thus may not be universally applicable to all hand configurations [86]. In contrast, we collected a reference dataset that captures the full ranges of all DoFs in various free hand motions, expressed with joint angles. Using a customized motion capture setup and marker layout, we captured the pure rotation of each finger bone. Since joint angles are a universal representation of human hand motion that does not depend on anatomical variation between individuals [54], we developed a post-processing method that extracts the joint angles from the collected data. When trained and tested with the comprehensive ground truth data, our system demonstrated enhanced performance over a wider range of wearers and diverse hand poses.

Finally, using the estimated kinematic parameters and joint motions, expressed in the form of the bone lengths and the joint angles, respectively, we take advantage of a method of FK to reconstruct the hand poses. This allows our system to be simple and efficient since it does not require a complex set of kinematic constraints often required for IK approaches, thus enabling instant updates of the hand configurations in real time [87]. Furthermore, the reconstruction is not limited to the scope of the constraints or the training dataset. Therefore, our glove system possesses inherent robustness, allowing for accurate estimation of all manner of hand poses, including unconventional and arbitrary ones. As a result, it finds applicability across a diverse array of applications.

3.2. Hardware design

3.2.1. Overview of the glove hardware design

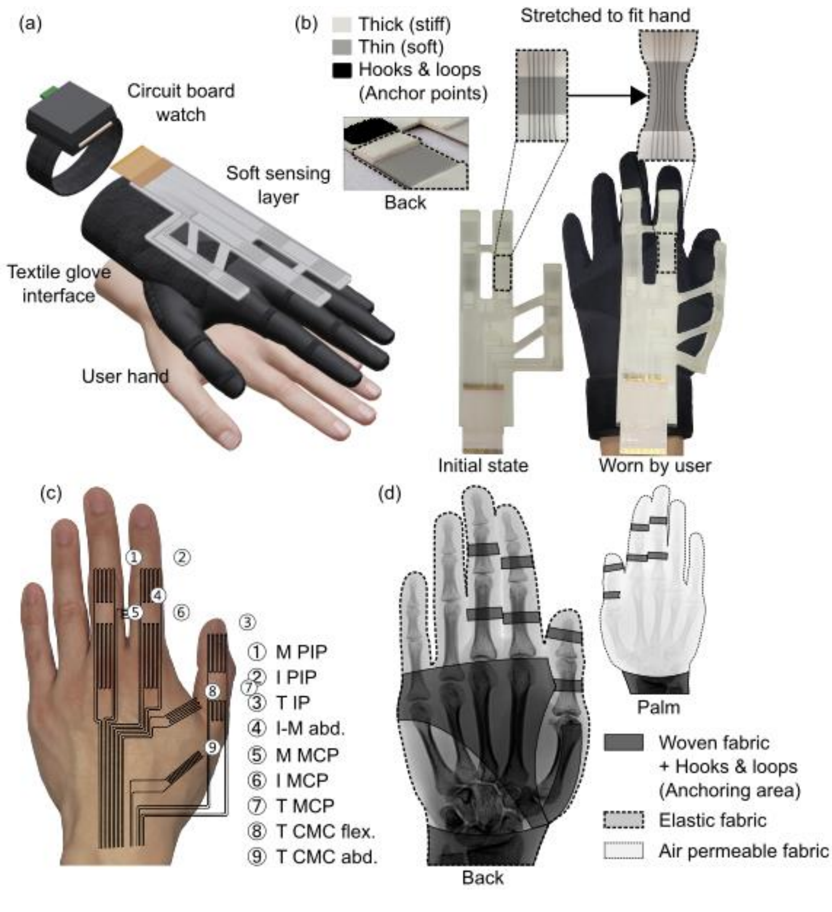

Figure 3.1. Glove hardware design: (a) Schematic diagram of the proposed glove system hardware comprising the soft sensing layer, the textile glove interface, and the watch-type circuit board shown with the hand of the wearer. (b) Image of the initial state of the soft sensing layer (left) and its pre-stretched state (right) when anchored onto a medium-sized hand; the inset images show the multi-stiffness substrate structure and its characteristic

deformation when stretched. (c) Placement of the liquid-metal sensor traces with respect to the hand. (d) Design of the textile glove interface composed of elastic fabric for unrestricted hand motion and hook-and-loop textile for anchoring; their positions are shown with respect to the finger bones of the wearer.

Glove-type soft wearable sensors have an advantage in hand motion sensing over other types of sensing methods as they are not limited by occlusion, strictly controlled environment [57,88], or bulky and rigid components [89,90,91]. Here, we present a wearable sensing glove that provides accurate and robust estimation of the human's hand kinematic structure and joint motion, all while ensuring comfortable wearability. The proposed sensing glove (**Figure 3.1a**) consists of three key components: a liquid-metal soft sensor layer characterized by its high sensitivity and flexibility to accommodate hands of all sizes; a custom-designed textile glove interface designed based on the human hand anatomy and kinematics; and a watch-type circuit board for signal acquisition and conditioning, securely enclosed and worn on the wrist for wireless transmission of sensor measurements. Since the kinematics of the ring and the pinky fingers closely resemble those of the index and the middle fingers, we demonstrate sensing of three fingers: the thumb, the index, and the middle finger. This selection adequately validates the performance of the proposed system.

3.2.2. Soft and sensitive liquid metal-based sensor

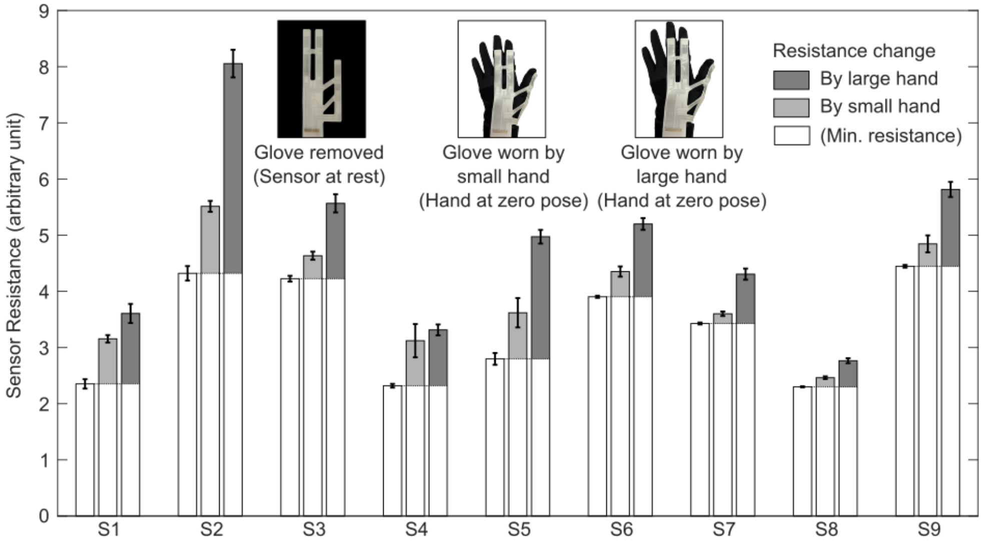

Figure 3.2. Nine sensor signals at zero pose and three states: Sensor signals for each of the nine sensors (S1-S9) measured at the initial unstretched state of the sensor (white), when worn on a small hand (light), and when worn on a large hand (dark), showing error bars obtained over five trials. Sensor signals were measured with the hand at zero pose. Inset images depict the sensor in each of the three states.

The top sensing layer is composed of a silicone substrate (Ecoflex 00-30, Smooth-On) embedded with nine traces of eutectic Gallium–Indium (eGaIn), a room-temperature liquid metal [92]. The soft and stretchable substrate can endure large deformations while exerting minimal force, allowing to accommodate a wide range of movements and conform to irregular contours of the human hand [93,94,95]. The liquid-metal traces are used to measure deformations of the hand as it conforms to the geometrical changes of the soft substrate during stretching, resulting in changes in resistance [96].

The sensing layer and the layout of the traces were strategically designed to simultaneously measure both the finger bone lengths and the joint motions. The dimensions of the sensing layer were intentionally designed to be smaller than the size of the hand, and when initially donned by the wearer, it must be stretched to adequately encompass all three fingers (**Figure 3.1b**). This initial stretch of the sensors provides a preliminary estimation of the hand size and finger bone lengths. The positions and the orientations of the nine eGaIn traces were also designed to measure strains caused by motions of the 10 DoFs of the seven joints in **Figure 3.1c**. During hand motions, the eGaIn traces of the sensing layer are further stretched or relaxed resulting in changes in resistance, providing information on the dynamic joint angles as well as the finger bone lengths. Further details on the estimation method will be discussed in the following subsections.

The mechanical structure of the sensing layer was designed to achieve the increased resolution, resulting in a more accurate measurement of the bone lengths and the joint angle. One approach to increase the sensitivity of the liquid-metal strain sensors is to design the substrate with a combination of multiple elastomer strips with different stiffnesses [97]. We employed this approach, creating the stiffness variations by altering the thickness of the substrate with a single material, as shown in **Figure 3.1b**. This method enhanced both durability and robustness of the sensor while also improving the sensitivity.

Hook-and-loop (Velcro®) patches were bonded to the bottom surface of the sensing layer to anchor the layer onto the textile glove interface. By securing the layer onto the middle of each finger bone, each sensor was positioned directly over each finger joint (**Figure 3.1d**). This anchoring method serves multiple crucial purposes, contributing to the reliability and repeatability of the glove system. Firstly, the anchor points serve as fixed reference points, not allowing rotation or displacement and ensuring all the sensors are subjected to uniaxial tension only.

Consequently, we can safely assume that the sensor signals are only affected by the strains resulting from the joint rotations. Secondly, the anchoring method not only enforces an injective relationship between the sensor signals and the joint angles but also minimizes coupling between the sensor signals. This means that every set of the sensor signals is unique to a combination of the joint angles and the bone lengths, representing a distinct hand configuration. Finally, the anchor points also provide a consistent and repeatable method for attaching the sensing layer. This is particularly important as the system must fit and track different hands with various sizes. The placement of the anchor points at the midpoint of the bones is easily identifiable for all hands, allowing for the consistent attachment of the sensing layer to the hand with minimal deviations in the sensor signals across repeated trials (**Figure 3.2**).

3.2.3. Custom textile glove interface

A customized textile glove was used as an interface between the sensing layer and the wearer's hand (**Figure 3.1a**). This interface serves the purpose of providing robust anchor points that effectively decouple the joint rotation of each finger from those of the other joints, while minimizing any physical interference or discomfort caused by sensors. **Figure 3.1d** depicts an example X-ray image of a male human hand. In order to allow natural finger movements without restrictions, the fabric surrounding the finger and the thumb joints must allow large deformations. Simultaneously, other parts, such as the finger bones located between the joints or on the back of the hand must provide sturdy anchoring points that maintain their positions relative to the wearer's hand. Therefore, elastic and inextensible fabrics were selected and patterned to provide a tight fit over the hand during dynamic motions, facilitating comfortable joint articulation. This approach also guarantees that all deformations are solely induced by the finger articulations.

3.3. Comprehensive dataset

The fundamental goal of our hand tracking system is to accurately quantify and measure the wearer's kinematic structure and the joint motion. To meet this goal, we must calibrate and evaluate the system using comprehensive training data that reflects the vast range of free hand motions. In the following subsections, we describe the procedures employed to acquire comprehensive ground truth data of the hand motions. We first present the motion-capture setup utilized for collecting raw hand motion data. Subsequently, we explain the details of the forward kinematic hand model on which our joint angle processing and hand reconstruction methods are based. Lastly, we discuss the post-processing method to extract the joint angles from the raw motion-capture data. Since these joint angles are not dependent on the variations in hand anatomy, this method allows the captured data from any subjects to be applicable to the general FK model to represent a wide range of wearers.

3.3.1. Motion-capture setup to collect comprehensive motion

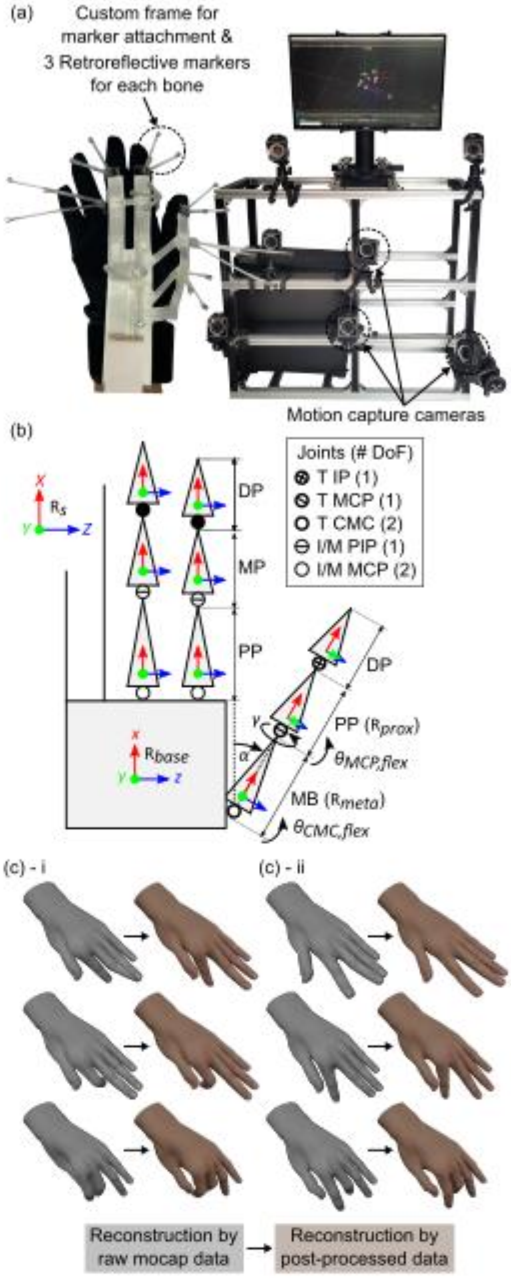

Figure 3.3. Collecting, modelling, and post-processing for comprehensive hand motion data: (a) Motion-capture setup for collecting hand motion data with custom retro-reflective marker frames to define the rigid body of each finger bone (left), and custom motion-capture camera stand (right). (b) Forward kinematic hand model at zero-pose showing the local frame of each finger bone, the joint positions, and the parameters defining the wearer's hand anatomy. (c) Reconstruction of hand poses using the raw motion-capture data (grayscale) and the post-processed data (colored).

Figure 3.3a shows the experimental setting for collecting diverse and unconstrained hand motion data which were used to calibrate and to evaluate our system. A commercialized motion-capture system (*OptiTrack, NaturalPoint*) was used to track the rotation of each bone. In various prior studies [98], retroreflective markers were attached to the finger joints and their positions were tracked to calculate rotation of the finger bones through the difference between two consecutive vectors, formed by neighboring markers. While this method is simple, it is highly susceptible to uncertainty in localizing the exact joint positions on the deformable skin, particularly during motion [99]. Instead, we used three markers (3 mm diameter) to define each bone as a rigid body to directly measure its rotation, which did not require precise positioning of the markers [98,100]. Since the human hand is a very small target [101,102] with a large range of motion, it is difficult to resolve the neighboring markers and avoid self-occlusions if the markers are directly attached to the fingers [63,103]. Therefore, we designed custom frames that protruded the markers outwards to provide enough spaces (>30 mm) between the markers and to prevent self-occlusion during the motion. These frames were attached to the anchor positions of the glove (**Figure 3.3b**) to ensure that the movements of the frames were driven only by the rotation of the corresponding bone.

3.3.2. Forward kinematic hand model for various hand anatomy

Figure 3.3b displays the forward kinematic hand model in its zero pose that we used to reconstruct the hand poses. In this model, we quantify the hand configuration using the bone lengths, the joint angles, and the anatomical parameters ($\alpha,\ \gamma$). In the figure, the lengths of the distal, the middle, and the proximal phalanges (DP, MP, PP) and the metacarpal bone (MB) of the thumb (T), the index (I) and middle (M) fingers are indicated. The IP and the MCP joints of the thumb and the PIP joint of the index and the middle fingers were modeled to have one-DoF flexion motions while the CMC joint of the thumb and the MCP joint of the index and the middle fingers have two DoFs including abduction [57,104,105]. We assumed there was no rolling motion of the index and the middle fingers. In the zero pose, the index and the middle fingers were fully extended and aligned and the thumb was straightened with its CMC joint fully adducted. At this state, all fingers lie on the same plane of the back of the hand. The local frame of each bone in these two fingers was defined by its *x*-axis aligned with the bone lengths and the *z*-axis aligned with the axis of flexion. The base frame was attached to the back of the hand. This arrangement of the local frames was a general model that can be used to represent all hands of different anatomy. On the other hand, the joint axes of the thumb were not aligned with the other fingers and this misalignment varies between individuals [104]. In our model, we specified this variation by parameterizing the abduction offset (α_{abd}) of the metacarpal bone frame (R_{meta}) from the base frame (R_{base}) and the roll offset (γ_{roll}) of the proximal phalange (R_{prox}) from the metacarpal bone (R_{meta}).

Since our metacarpophalangeal (MCP) and the Interphalangeal (IP) joints move with one DoF, by assigning the local frames in a specific orientation with the abduction offset α_{abd}^{*} and the roll offset γ_{roll}^{*}, the rotation of the proximal phalange and the distal phalange can be expressed using a single flexion angle.

These specific offset values, which will be referred to as *true offsets* hereafter, depend on the anatomy of the individual and can be identified by analyzing the rotations of the bones during hand motion.

3.3.3. Post-processing method for identifying hand anatomy and extracting joint angles

To identify the *true offsets* from the raw bone rotations obtained through the motion-capture, we first assumed arbitrary offsets, α_{abd} and γ_{roll}, for the thumb metacarpal bone ($R_{meta}(\theta_{CMC,flex} = 0)$) and the thumb proximal phalange ($R_{prox}(\theta_{MCP,flex} = 0)$). Then, the rotation of each bone during its flexion motion ($R_{meta}(\theta_{CMC,flex})$, $R_{prox}(\theta_{MCP,flex})$) can be expressed in the motion-capture global frame (R_s) as a function of the flexion angle ($\theta_{CMC,flex}$ or $\theta_{MCP,flex}$) and the true offsets (α^*_{abd}, γ^*_{roll}) as:

$$\begin{aligned}
R_{meta}(\theta_{CMC,flex}) &= e^{[\omega_{CMC,flex}]\theta_{CMC,flex}} R_{meta}(0) \\
&= e^{[\omega_{CMC,flex}]\theta_{CMC,flex}} R_{base} R_Y(\alpha_{abd}) \\
\\
&= R_Y(\alpha^*_{abd}) R_Z(\theta_{CMC,flex}) R_Y(\alpha^*_{abd})^{\mathrm{T}} R_Y(\alpha_{abd}) \\
&= R_Y(\alpha^*_{abd}) R_Z(\theta_{CMC,flex}) R_Y(\alpha_{abd} - \alpha^*_{abd}) && (3.1) \\
&= R_Y(\theta_1) R_Z(\theta_2) R_X(\theta_3), && (3.2) \\
R_{prox}(\theta_{MCP,flex}) &= e^{[\omega_{MCP,flex}]\theta_{MCP,flex}} R_{prox}(0) \\
&= e^{[\omega_{MCP,flex}]\theta_{MCP,flex}} R_Y(\alpha^*_{abd}) R_X(\gamma_{roll}) \\
&= [R_Y(\alpha^*_{abd}) R_X(\gamma^*_{roll})] R_Z(\theta_{MCP,flex}) \\
&\qquad [R_Y(\alpha^*_{abd}) R_X(\gamma^*_{roll})]^{\mathrm{T}} R_Y(\alpha^*_{abd}) R_X(\gamma_{roll})
\end{aligned}$$

$$= R_Y(\alpha^*_{abd})R_X(\gamma^*_{roll})R_Z\big(\theta_{MCP,flex}\big)R_X(\gamma_{roll} - \gamma^*_{roll}) \quad (3.3)$$

$$= R_Y(\alpha^*_{abd})R_X(\theta_1)R_Z(\theta_2)R_Y(\theta_3)\ , \quad (3.4)$$

while the base frame is aligned with the global frame ($R_{base} \equiv R_s = \mathrm{I}$). Here, $\omega_{CMC,flex}$ and $\omega_{MCP,flex}$ represent the rotation axes of the thumb MCP and IP joints, respectively. If the arbitrary offsets equal the true offsets (i.e., $\alpha_{abd} = \alpha^*_{abd}$ and $\gamma_{roll} = \gamma^*_{roll}$), the last terms in **Equations 3.1** and **3.3** become identity. The rotation matrices R_{meta} and R_{prox} can be obtained through the motion-capture system and expressed as YZX and XZY Euler angles, as shown in **Equations 3.2** and **3.4**. Here, the elements of the Euler angles (θ_1, θ_2, θ_3) represent the offset, the flexion angle, and zero, respectively. By sweeping the offset values, we can identify the *true offsets* as the values that minimize θ_3.

By assigning the local frames on every bone and phalange based on the identified offsets, relative rotations between successive rigid bodies were calculated. For 1-DoF joints (PIP of the index and the middle finger, IP and MCP of the thumb), the angles in axis-angle representation of the relative rotations were regarded as the flexion angles [106]. For 2-DoF joints (MCP of the index and the middle finger, and CMC of the thumb), we interpreted the pitch and the yaw angles of the relative rotations as the flexion and the abduction angles since the *true offsets* result in negligible roll angles.

We confirmed that the reconstructed hand poses using the hand model from **Figure 3.3b** and the post-processed joint angles were able to accurately represent the target hand poses, as shown in **Figure 3.3c**. The poses on the left (grayscale) were reconstructed by direct application of the 21-DoF raw motion-captured bone rotations to the finger bones. The poses on the right (colored) were reconstructed by inputting the processed joint angles through the method described above into the 10-DoF hand model in **Figure 3.3b**. It is apparent that the proposed method is able to reproduce the original poses by correcting unnatural motions (**Figure 3.3c-i**) that result from the redundant degrees of freedom.

3.4. Pose estimation

Our glove system takes advantage of the stretchable sensor mechanism to attain information on both the bone lengths and the joint angles. The initial stretch of the sensor when it is worn on the hand, provides the initial estimation of the wearer's bone lengths. Afterwards, the sensor signals obtained during dynamic hand motions are used to refine this estimation as well as estimate the joint angles. The system is calibrated and evaluated for general wearers using the comprehensive ground truth data discussed in the previous subsections.

3.4.1. Initial estimation of bone lengths using initial sensor signal

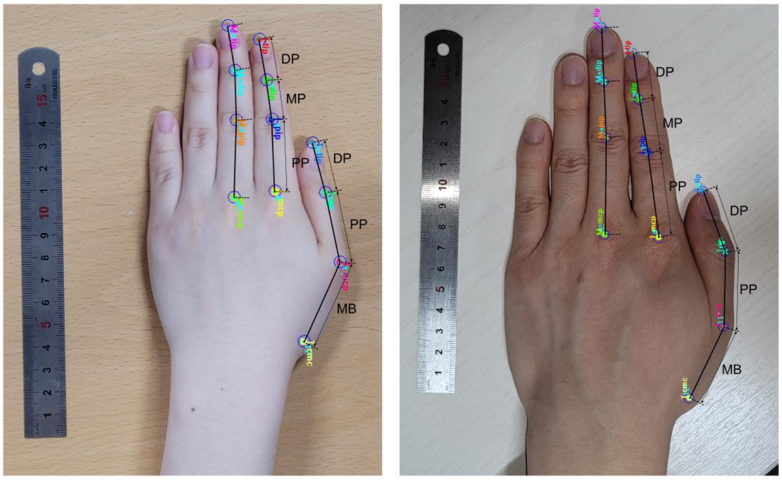

Figure 3.4. Finger bone length measurement method using ProAnalyst, indicating position of each joints marked

Table 3.3. Mean and standard deviation of absolute estimation error of finger bone lengths collected from 11 subjects: The values were normalized by the true bone lengths.

	Absolute estimation error									
	I DP	I MP	I PP	M DP	M MP	M PP	T DP	T PP	T MB	Avg.
Mean (mm)	1.75	1.45	3.21	2.12	1.10	3.05	1.90	2.59	1.78	2.10
Norm. mean (%)	8.10	6.64	8.59	9.08	4.14	7.39	7.11	6.85	4.46	6.93
Std. dev. (mm)	1.15	1.08	1.92	1.11	1.04	2.81	1.42	2.16	1.42	1.57
Norm. std. dev. (%)	5.85	5.08	5.44	5.22	3.84	7.60	5.72	4.72	3.56	5.22

Table 3.4. Initial bone lengths estimation results (RMSE) of all 11 subjects and all bones.

Subject	RMSE (mm)									
No.	I DP	I MP	I PP	M DP	M MP	M PP	T DP	T PP	T MB	Mean
1	2.27	1.54	2.99	3.52	1.16	5.37	2.01	1.00	1.26	2.35
2	1.70	1.56	2.98	2.17	0.22	3.95	1.21	3.58	0.86	2.03
3	3.86	2.98	6.31	3.40	2.23	8.55	4.13	1.29	0.44	3.69
4	1.98	0.41	4.76	2.10	1.85	0.54	1.27	4.20	1.68	2.09
5	0.77	3.37	2.68	0.98	0.66	1.25	2.08	2.10	2.51	1.82

6	1.43	1.51	5.63	0.66	1.21	0.99	0.40	8.21	1.60	2.41
7	1.88	0.33	0.82	3.28	0.43	1.15	0.65	2.88	4.34	1.75
8	0.50	0.68	0.05	1.79	0.22	0.65	0.08	0.83	0.17	0.55
9	0.46	0.13	1.69	1.36	0.52	0.75	2.04	1.47	3.85	1.36
10	0.82	2.39	3.42	0.74	3.43	3.59	2.49	1.53	0.19	2.07
11	3.56	1.02	4.00	3.28	0.13	6.75	4.53	1.36	2.69	3.03
Mean	1.75	1.45	3.21	2.12	1.10	3.05	1.90	2.59	1.78	2.10
St. Dev.	1.15	1.08	1.92	1.11	1.04	2.81	1.42	2.16	1.42	1.57

The underlying assumption for deriving the initial estimation of the bone lengths from the initial sensor signal is that a unique set of sensor signals is generated by each different hand anatomy thanks to the design of the consistent anchor points in **Figure 3.1d**. We collected data from 11 subjects (8 males and 3 females) to test this assumption and characterize the estimation model. Details on the testing procedure and characterization method will be described in **Figures 3.2** and **3.4**. The experimental procedures are approved by the Seoul National University Institutional Review Board (IRB No. 2207/004-005, approved 20/07/2022). Each subject was instructed to put on and remove the sensing layer five times, during which the sensor signals were alternately collected when the glove was worn (*hand at zero pose*) and removed (*sensor at rest*). The bone lengths of each subject were measured by a commercial image analysis software package (ProAnalyst, Xcitex). As expected, increased sensor signals were observed in larger hand sizes and bone lengths. We then used the Gaussian process regression which is a multivariate nonparametric regression method to predict the bone lengths from the sensor signals. The mean function of the regression model was assumed to be quadratic in consideration of the hyperlinear nature of the microfluidic sensors and the squared exponential kernel function was used [96,107]. To evaluate the prediction, leave-one-out cross-validation was conducted for each subject.

The results of the bone lengths estimation are summarized in **Table 3.3** (absolute estimation error in mm and normalized absolute estimation error by the bone lengths in %). The mean absolute errors averaged over all bones was 2.1 mm, approximately 6.9% of the target bone lengths. The results of the initial bone lengths estimation of all 11 subjects are presented in **Table 3.4**.

3.4.2. Refinement of bone lengths using signal distributions

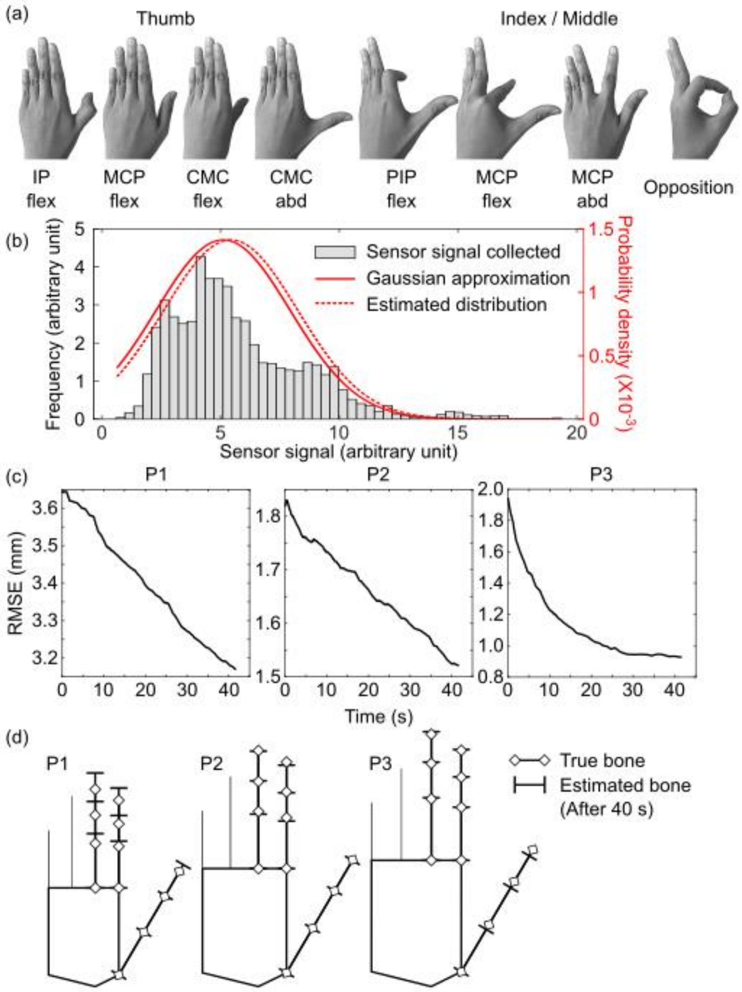

Figure 3.5. Real time refinement of bone lengths using signal distributions: (a) Collection of hand poses conducted for the refinement of bone lengths estimation. All motions were restricted to these eight poses. (b) Histogram of the sensor signals of I-M abd. in **Figure 3.1(c)** collected over the hand motion test; its Gaussian approximation defined by the true mean and variance of the histogram, and the estimated distribution defined by the mean and covariance estimated from the subject's bone lengths. (c) Plot of average estimation errors of 10 bones with respect to time of continuous hand motions, shown for three participants (d) Graphical representation of the estimated and true bone lengths of the three participants.

Table 3.5. Refined bone lengths estimation results of all 5 subjects and all bones: "True", "Initial", and "Refined" represent the true bone lengths, initial estimation errors (RMSE), and refined estimation errors (RMSE), respectively.

RMSE (mm)															
Subject No.	I DP			I MP			I PP			M DP			M MP		
	True	Initial	Refined	True	Initial	Refined	True	Initial	Refined	True	Initial	Refined	True	Initial	Refined
1	18.43	3.66	3.10	17.73	3.87	2.34	32.34	5.00	4.17	20.16	3.35	2.05	22.25	3.02	3.01
2	22.79	2.55	3.31	22.43	1.40	0.83	36.59	1.74	2.13	24.93	2.66	4.13	27.17	1.24	0.91
3	21.14	2.15	0.22	23.49	2.42	0.14	41.44	0.50	0.21	22.82	3.21	1.04	27.83	0.81	0.05
4	23.46	2.23	1.79	20.05	1.73	2.00	39.80	2.89	2.67	24.21	1.43	0.94	23.41	3.11	2.52
5	20.50	0.43	0.05	21.00	0.90	0.84	33.04	3.96	3.40	21.31	0.89	0.17	25.80	1.86	1.23
Subject No.	M PP			T DP			T PP			T MB			Mean		
	True	Initial	Refined	True	Initial	Refined	True	Initial	Refined	True	Initial	Refined	True	Initial	Refined
1	34.71	8.19	7.70	22.73	4.56	5.02	32.04	1.06	1.11	38.68	0.05	0.02	31.44	2.32	2.29
2	47.91	7.36	5.28	28.34	1.47	1.66	33.46	2.13	2.09	39.35	0.31	0.31	26.56	3.64	3.17
3	48.00	0.38	1.02	28.83	2.49	0.13	38.85	1.10	1.17	42.61	4.45	4.36	30.83	1.82	1.52
4	44.60	2.64	2.03	28.10	1.28	0.71	33.53	0.56	0.57	40.32	0.49	0.45	27.91	1.82	1.67
5	37.81	3.25	2.97	25.49	0.04	1.36	31.19	1.37	1.37	35.09	3.68	3.62	32.78	1.95	0.93

Once the wearer starts moving the fingers, the change in the sensor signals form a unique distribution depending on the hand size, which can be used to further refine the initial estimations made in the previous subsection. From Bayes rule [108], the bone lengths (x) estimation can be updated given the subsequent sensor signals (y) as

$$p(x|y) \sim p(x)\ p(y|x), \tag{3.5}$$

assuming that the *a priori* distribution $p(x)$ is obtained from the initial estimation and the likelihood distribution of the sensor signal, $p(y|x)$, was characterized as a function of the bone lengths [109]. To characterize the likelihood, we conducted another experiment with five subjects (two females, three males) and collected sensor signals during dynamic hand motions. To simplify the problem, the hand motions were constrained to the poses illustrated in **Figure 3.5a** to ensure that the likelihood in **Equation 3.5** can be fitted as Gaussian. For each subject, the mean ($\mu \in \mathrm{R}^9$) and variance ($\sigma_i \in \mathrm{R}^9$) of the collected sensor signals were calculated and then linearly fitted to the subject's bone lengths ($x \in \mathrm{R}^{10}$) as

$$\mu \cong \mathrm{M}x = \hat{\mu}, \tag{3.6}$$

$$\mathrm{Diag}(\sigma_i) \cong \mathrm{V}x = \hat{\Sigma}. \tag{3.7}$$

An example of the fitted result is presented in **Figure 3.5b**, showing the histogram of one sensor signal with its Gaussian approximation, $N(\mu, \mathrm{Diag}(\sigma_i))$, defined by the true mean and variance of the sensor signals, and the estimated distribution, $N(\hat{\mu}, \hat{\Sigma})$, defined by the estimated mean and covariance calculated from the subject's bone lengths. From the Gaussian assumption, the *a posteriori* distribution can be obtained in an analytic form as

$$\hat{x}_{\mathrm{k}} = \hat{x}_{k-1} + \mathrm{P}_{k-1}M^{\mathrm{T}}\left(MP_{k-1}M^{\mathrm{T}} + \hat{\Sigma}\right)^{-1}(y_k - \mathrm{M}\hat{x}_{k-1}), \tag{3.8}$$

$$P_k = \left(\mathrm{I} - P_{k-1}M^{\mathrm{T}}\left(MP_{k-1}M^{\mathrm{T}} + \hat{\Sigma}\right)^{-1}M\right)P_{k-1}. \tag{3.9}$$

Here, the equation is expressed in recursive form since the estimation is continuously updated in real time as the sensor signals arrive sequentially $(\dots, y_{k-1}, y_k)$.

Note that the Gaussian assumption in **Equations 3.6** and **3.7**, and the analytic form in **Equations 3.8** and **3.9** are only valid for motions limited to those shown in **Figure 3.5a**. To release this constraint, i.e., to allow the wearer to move their hand more freely while updating the bone lengths estimation, the design of the likelihood function may have to be non-Gaussian and the posterior should be calculated using different methods [110,111], which we leave for future work. **Figures 3.5c** and **3.5d** exemplify how the update algorithm refines the bone length estimation in three subjects (two males, one female). For all three subjects, the average estimation error (**Figure 3.5c**) of the ten bone lengths continuously decreased with time as the subjects moved their hands. After 40 seconds, the average error was reduced by 12.9%, 16.3%, and 8.3% for each subject from their initial estimates. This refinement produced a more accurate estimation of the bone structure that better resembled the true hand, as graphically depicted in **Figure 3.5d**. The results of the refined bone lengths estimation of all five subjects are summarized in **Table 3.5**.

3.4.3. Estimation of joint angles

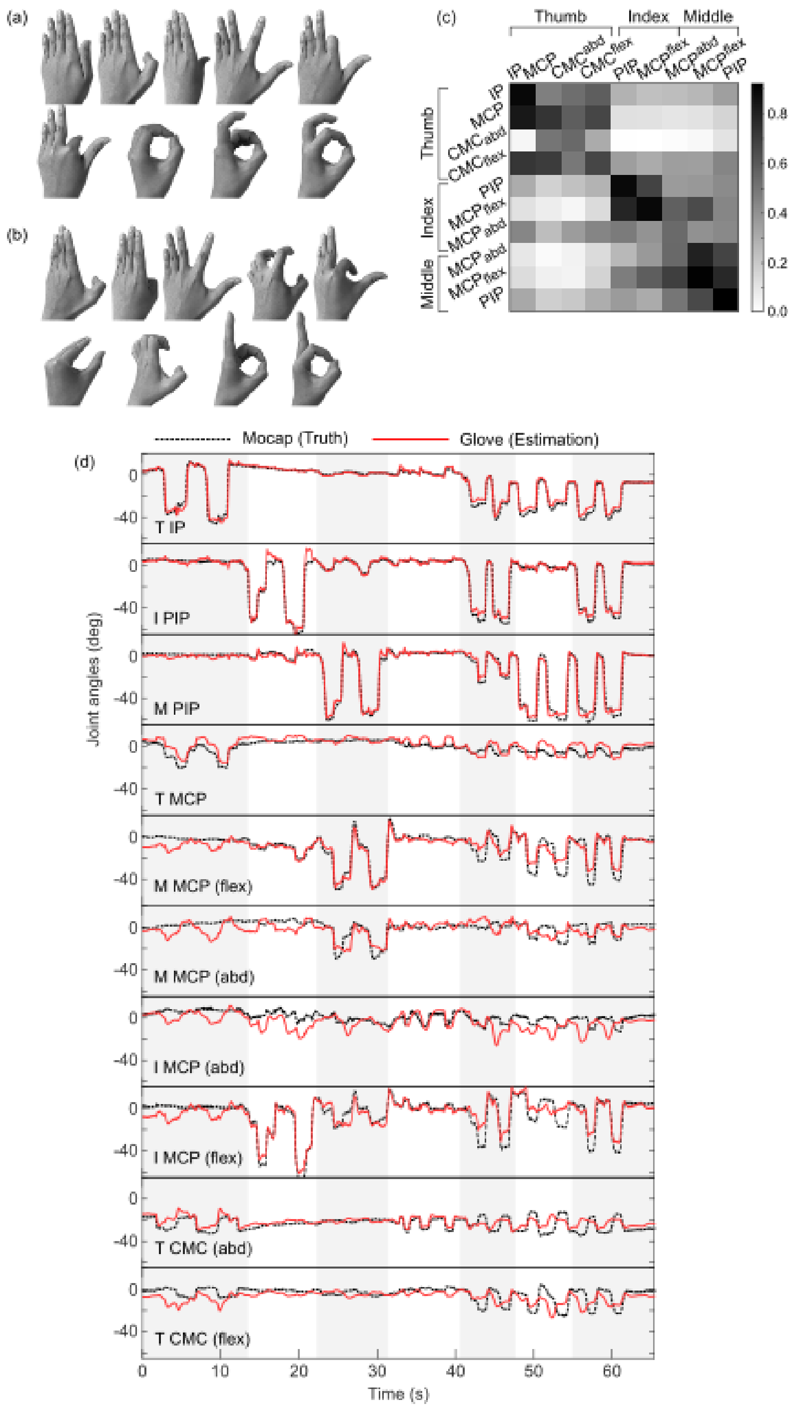

Figure 3.6. Real time estimation of joint angles: (a-b) Collection of hand poses conducted during the calibration (a) and the evaluation (b) for the joint angle estimation. (c) Graphical representation of the correlation between the joint angles (vertical) and the sensor signals (horizontal) in calibration dataset. (d) Plot of the time trajectories of the estimated and true

joint angles for the large hand subject in the *self-calibration* group.

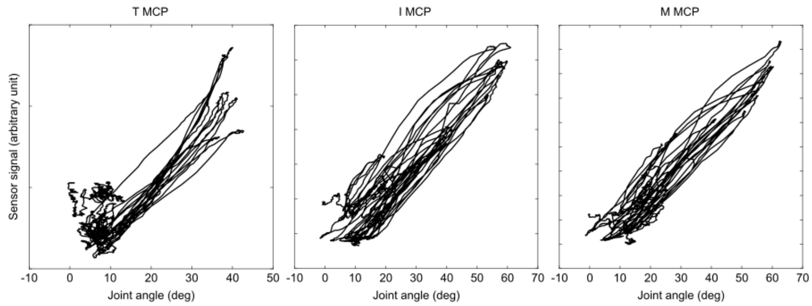

Figure 3.7. Sensor linearity: Sensor signal generated by corresponding (**Figure 3.1(c)**) flexion angles of thumb MCP, index and middle finger MCP joints.

Table 3.6. Mean absolute errors of finger joint angles for subjects in the *self-calibration* group and *non-calibration* group.

Subject		Absolute estimation error (degree)										
		T IP flex.	I PIP flex.	M PIP flex.	T MCP flex.	M MCP flex.	M MCP abd.	I MCP abd.	I MCP flex.	T CMC abd.	T CMC flex.	Avg.
Self-calibration	*Small* hand	2.10	2.05	2.27	11.83	4.51	2.23	3.98	4.62	1.57	3.93	3.91
	Large hand	1.85	2.17	2.68	4.15	4.61	5.23	6.16	5.47	3.79	5.48	4.16
Non-calibration	*Small* hand	1.77	3.01	4.85	3.00	8.88	5.75	3.42	0.47	15.08	0.61	4.69
	Large hand	5.44	4.73	3.94	3.96	11.93	7.57	8.67	13.11	3.13	8.93	7.14

To calibrate and test the joint angle estimation model, we first collected a new comprehensive hand motion dataset. The motion data were collected from two groups of subjects: 1) *self-calibration* group (one male, one female) provided the calibration and the test data, and 2) *non-calibration* group (one male, one female) only provided the test data. During the experiment, the subjects performed diverse and unconstrained hand motions that utilized the full DoFs, deforming each finger joint to the limit (the maximum flexion-extension and abduction-adduction) and exploiting the entire task space of their hands. The poses are partially shown in

Figures 3.6a and **3.6b**.

Figure 3.6c visualizes the correlation between the joint angles and the sensor signals in the calibration data. This map presents dominant diagonal elements, which represents a strong correlation between the joint angle of each finger and its corresponding sensor signal (**Figure 3.6c**), as well as significant off-diagonal elements attributed to the synergetic nature of the hand motions [112,113] and mechanical coupling between the sensors. Based on these relationships between the sensor and the joint angles, a system model with a state ($\mathrm{x}_k \in \mathrm{R}^{10\times 6}$) of the joint angles captured in the previous 0.1 seconds (series of 6 data points at 60 Hz) and the sensor observation ($y_k \in \mathrm{R}^9$) was defined as

$$\begin{aligned} \mathrm{x}_{k+1} &= Ax_k + w_k, \\ \mathrm{y}_k &= Hx_k + v_k, \\ w_k &\sim N(0, \mathrm{Q}),\ \ v_k \sim N(0, \mathrm{R}). \end{aligned} \tag{3.10}$$

The linear system model in **Equation 3.10** was based on two conditions. First, bias terms of the joint angles and the sensor signals were removed from the state (x_k) and the observation (y_k). The joint angle bias refers to the non-zero thumb CMC abduction (α_{abd}) at the zero pose, and the sensor bias is the initial sensor signal that was used to estimate the bone lengths. By removing the initial sensor signal, the joint angle estimation was separated from the bone length estimation. Second, we assumed a linear sensor model. This assumption is grounded on the observation that the relationships between the sensor signals and their corresponding joint angles are approximately linear within the range of motion of the joint (**Figure 3.7**). However, since liquid-metal strain sensors display a hyperlinear behavior in large deformations, the gradient of the linear relationship must be modified to

compensate the different levels of pre-stretching by different wearers. In this study, we categorized the subjects into *small* and *large* hands and the system matrices (A, Q, H, R) of each group were calibrated by fitting the sensor data and the ground-truth calibration dataset to **Equation 3.10** by the least-square method.
The sensor signals were processed and the joint angles were estimated using a Kalman filter. We evaluated the estimations using the test data (~65 seconds, **Figure 3.6b**).

The results of joint angle estimation (the mean absolute errors of each joint) are summarized in **Table 3.6**. **Figure 3.6d** shows the result of the *large* hand subject in the *self-calibration* group, comparing the time trajectories of the estimated and the true (motion-captured) joint angles. For all hand sizes, and for both *self-calibrated* and *non-calibrated* subjects, the average angle estimation outperformed the off-the-shelf hand tracking systems evaluated in [61]. Although the errors in the *non-calibration* group were larger than those of the *self-calibration* group, the calibration method can be further refined with more dataset of various hand sizes, and the system may be universally adopted for a large range of arbitrary wearers with a high accuracy.

3.4.4. Estimation of fingertip positions

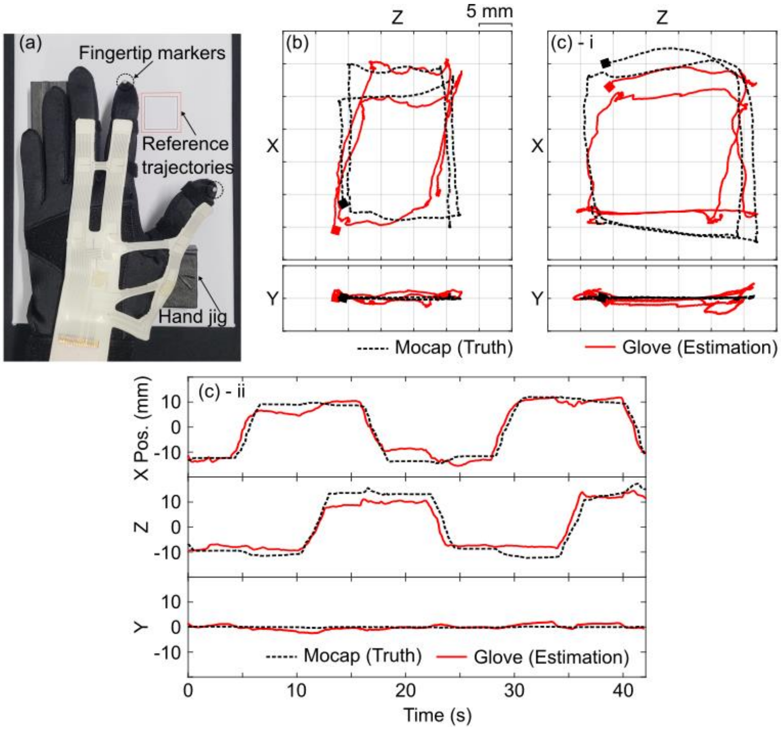

Figure 3.8. Fingertip position estimation: (a) Test setup for prediction of the fingertip position using the bone length and the joint angle estimations. (b) 3D trajectories of the true (motion captured) and the estimated fingertip positions for the small handed subject. (c) 3D trajectories (i) and the time trajectory (ii) of the true (motion captured) and estimated fingertip positions for the large handed subject.

Table 3.7. Mean absolute errors of fingertip position estimation in X, Y, Z direction and the 3d space: The normalized 3d errors were calculated by dividing the 3d error with the side length of the workspace for each subject.

Subject	Absolute estimation error (mm)				
	X	Y	Z	3d	3d (Normalized)
Small hand	1.97	0.51	1.99	3.24	16.2%
Large hand	2.15	0.75	2.81	4.02	16.1%

First, we conducted a quantitative analysis of the hand pose reconstruction by predicting the fingertip positions. Retroreflective markers were attached to the fingertips, and their positions were tracked while the wearer moved the hand with the glove. The test setup and the procedures are described in **Figure 3.8a**. The tests were conducted for two subjects (one male, one female) with different hand sizes. Each subject was provided trajectories of a square with side lengths of 25 mm and 20 mm and instructed to follow the traces with their index finger and thumb, as shown in **Figure 3.5a**. The sizes of the trajectories were selected based on the workspace of each subject's fingers. Also for uniform sampling of the test data for unbiased evaluation, the subjects were guided by periodic (every three seconds) buzzer sound between each stroke.

Figures 3.8b and **3.8c-i** compare the reconstructed and the ground truth (motion-captured) 3D fingertip trajectories for the *small* and the *large* hands, respectively, and **Figure 3.8c-ii** depicts the time trajectory results for the *large* hand. The mean absolute errors of the fingertip tracking test are presented in **Table 3.7**.

Overall, the reconstructed trajectories coincide with the ground truth. However, it underestimated the range of the motions and the result of the smaller hand also showed distorted trajectories in space. These errors were most likely generated by the combined effect of the errors in the joint angles, the bone lengths, and the hand anatomy (α_{abd} and γ_{roll}). The underestimation of the fingertip positions was a result of the underestimated joint angles, as shown in **Figure 3.6d** as well as the errors in the bone lengths. The distortion in the thumb motions is attributed to the errors in the abduction and the roll offset that decouple the abduction and the flexion motions.

Nevertheless, the mean absolute 3D position errors were 3.24 mm and

4.02 mm for the *small* and *large* hands, respectively, lower than a half of the smallest reported error of among commercially available hand tracking systems [61]. These 3D errors were both approximately 16% of the side length of the workspaces, which suggests the performance of the fingertip position reconstruction is consistent regardless of the hand sizes.

3.4.5. Hand pose reconstruction

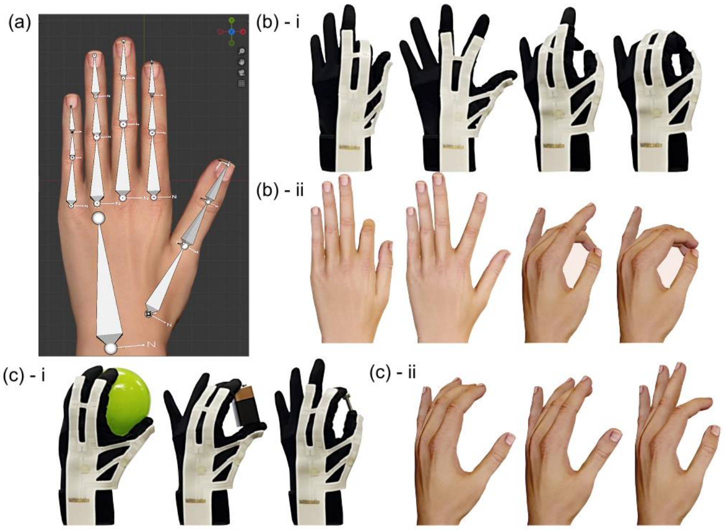

Figure 3.9. Real time hand pose reconstruction: (a) Armature and mesh of the virtual hand created in an open-source 3D computer graphics software tool (Blender). (b-i) Image of the wearer's real hand during various free hand motions and (b-ii) the corresponding real time reconstruction of the hand poses in the virtual environment (c-i) image of wearer's real hand during three different grasping poses (c-ii) corresponding real time reconstruction of the hand pose.

Qualitative assessment of the proposed hand reconstruction method was conducted by visualizing the result in a virtual environment and comparing it to the real hand. An open-source 3D computer graphics software tool (Blender), was used to create a virtual hand in close proximity to the real human hand (**Figure 3.9a**). The finger bone lengths and the joint angles estimated by the proposed glove system are the inputs to update the length and the rotation angle for each virtual finger bone in real time at 30 Hz. The reconstruction was based on FK, and no additional constraints were applied to the motion of the virtual hand. Since the ring and the pinky fingers were not directly measured by the glove, their rotation angles were assumed as two-thirds of the middle finger joints for visualization purposes.

We first reproduced free hand motions involving articulation of each individual finger, as well as their combined motions. Examples of the reconstructed hand poses are shown in **Figure 3.9b**. The reconstructed hand poses closely resembled the real hand poses, accurately reproducing the full DoFs of the finger joints. Particularly, the ability to successfully reconstruct contact or proximity of multiple fingertips through FK without any kinematic constraints or tactile sensors highlights the accuracy of the bone lengths and joint angle estimations. **Figure 3.9c** shows the reproduction of various grasping poses. The virtual hand closely reflected the unique features of the grasping poses ranging from spherical and tripod grips to precision grips (two-fingered pinching), showing the glove performance unaffected by the surrounding environment or contacts with the object in grasp.

3.5. Applications

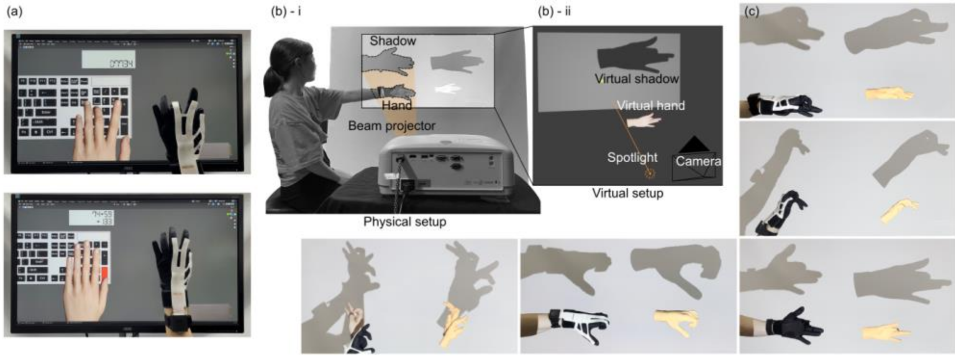

Figure 3.10. Applications in virtual reality: (a) Application of virtual number pad typing of five-digit number (top) and arithmetic operation (bottom). (b) Real world environment (i) and twin virtual environment (Blender) (ii) for real time virtual shadowgraphy. (c) Examples of virtual shadowgraphy showing the real hand and the shadow (left) and the virtual hand and shadow (right).

3.5.1. Number pad typing

To demonstrate the performance and the potential of our sensing glove for use in real world applications, we first conducted a task of typing a virtual number pad (**Figure 3.10a**). Typing, although a very mundane task, requires precise manipulation of the fingers and accurate positioning of the fingertips. Since the fingertips must make contacts with specific locations of the keys, the success of the virtual typing largely depends on accurate estimation of the fingertip position as well as the overall hand configuration that does not cause any unintentional interactions with the keyboard. Since the proposed glove was designed for the left hand of the wearer, we operated a virtual number pad, which can be done with a single hand without controlling the wrist motion. The workspace of the two tasks shown in the demonstration was 80-by-60 mm, which covered the entire area of the number pad, and thereby proved the accuracy of the fingertip position estimation in the large task space.

3.5.2. Shadowgraphy

Next, to prove the robustness of our system in complex and unconventional poses, we demonstrated virtual shadowgraphy. Shadowgraphy is the art of creating distinct figures, such as animals or humans, by projecting shadows casted by the performer's hands. This task requires articulate control of the hand, involving very complex, unusual, and unique hand poses that we may not use in our day-to-day lives. Therefore, it is a good example that can highlight the robustness of our FK method that can accurately reconstruct even uncommon and unnatural hand postures using accurate finger bone lengths and joint angles estimations. As shown in **Figure 3.10b**, a set of twin environments (real and virtual) was set up for real-time comparison of the casted shadows. We first designed a 3D virtual environment with a strong light casted against a hand model to project its shadow onto the vertical plane at the back. A twin environment was set up in the real world with a projector and a screen, so that the wearer could simultaneously cast the hand shadow onto the screen where the virtual hand and its shadow were also displayed for comparison. While the postures of the index and the middle fingers and the thumb were updated in real time based on the sensor glove's estimations, the postures of the ring and the pinky fingers were fixed to the desired configuration since their precise postures were also required in this application.

We demonstrated shadowgraphy of five animals, as shown in **Figure 3.10c**, and for the rabbit, an additional virtual right hand was added, fixed in a similar way to the ring and the pinky fingers. Some differences between the real and the virtual shadows were apparent. However such dissimilarities can be attributed to the differences in the relative position of each hand (virtual and real) with respect to its environmental conditions (e.g., light, screen, or camera), and the differences in hand contour due to the textile glove and the sensing layer. Overall, the proposed system successfully reconstructed complex hand poses to create all five animals.

3.6. Discussion and future works

We proposed a compact wearable glove capable of estimating both bone lengths and joint angles of the wearer with a simple stretch-based sensing mechanism. The system achieved superb accuracy and robustness, confirmed by the evaluations of joint angle estimation, fingertip position estimation, and overall hand pose reconstruction in various virtual applications. We argued that our comprehensive hand motion dataset contributed to the performance. The data were collected with a customized motion-capture setup and transformed into joint angles through the proposed post-process method. To prove that the post-processed dataset reflects the extensive range of natural motions and various anatomical structures, we qualitatively evaluated the biomechanical plausibility and overall similarity of the reconstructed hand poses by the raw (motion-captured) data and the post-processed data. Also, to evaluate the performance of the wearable hand tracking system that was calibrated by the dataset, we suggested both the quantitative and qualitative methods; We calculated the joint angle and the tip position errors, and also qualitatively compared the poses of the real and the virtual hand to evaluate the overall pose estimation. However, the suggested qualitative evaluations are subjective and difficult to implement across a wide range of different systems.

Therefore, our future work would be to find a computable distance metric that can quantitatively evaluate the overall hand pose. In this section, we explore some possible candidates from the previous literatures.

Noy et al., in addition to calculating the Cartesian position error of the fingertip, conducted the human subject test where six subjects were asked to rate the similarity between the real and rendered images [114]. This research tried to compare the performance of the three different reconstruction methods. Even though they showed a significant difference in the score between the methods for specific poses, they were not able to derive any conclusion across all test poses. However, based on the experimental results, they discussed about how to select proper poses for the evaluation.

Tkach et al. suggested a dense evaluation method instead of the sparse marker-based evaluation that we had done [115]. First of all, they paired each of the points in the point clouds of the virtual and the real hand by closest-point projection. Then, they calculated the residual across the entire geometry of the hands as an evaluation metric. This metric may reflect the overall pose better than the marker position error. However, it highly depends on how the points are paired, which has to be carefully considered to be selected.

Lastly, Sharp et al. tried to evaluate the robustness and flexibility of their vision-based pose reconstruction method, in addition to its accuracy [116]. They conducted experiments with a wide range of users including both males and females, and also varied the distances and orientation of the user's hand relative to the camera to prove that their system performs well in various conditions.

Chapter 4

Perception for Interactive Teleoperation of Soft Grippers*

4.1. Introduction

4.1.1. Motivation

Due to the enriched security and sensitivity, the concept of human-in-the-loop teleoperation of robotic systems has been used for a wide range of applications that require delicacy and safety, such as cell manipulation, grasping in cluttered environments, and robot surgeries [118]. For enhanced performance, immersive and transparent control and haptic feedback are the keys, that provide useful information about the target system to the human operator for closing the bi-directional teleoperation loop.

Three requirements have to be satisfied for achieving the keys. First, a sophisticated perception of the target system is important. The haptic feedback has to be generated timely and properly according to the perceived information due to the event that occurred in the target domain. For example, feedback has to be turned on if and only if there actually happened the relevant event. For traditional

* The contents in this chapter have been published in [117], in collaboration with Prof. Moon Jeong Park (POSTECH).

robots with motors and encoders, the state estimation is straightforward, but for the soft robots, it is not. Especially the soft actuators that have ultra-thin form factors [119,120], such as electroactive polymer, dielectric elastomer, shape memory polymer, liquid crystal elastomer-based, and light-driven actuators, it is challenging to embed additional sensor to measure the deformation along their body without degrading the actuation performance. Unless the state (or deformation) of the actuator cannot be precisely measured, the control of the system is impossible, which limits the potential application of the thin soft actuators despite their advantages in compactness and safety.

Second, a haptic feedback device has to induce minimal discomfort and hindrance to the motion while producing the stimuli to the operator. The use of a haptic device can help the operator to make an appropriate decision as a complement to the visual feedback in harsh conditions such as occluded environments. However, unless it is thoroughly designed, it can confuse the operator's cognition or limit the operation. There have been various types of haptic devices, which will be discussed more in detail in the next subsection, but none of them achieved wearability, compactness, and safety at the same time.

Lastly, an input device that interprets the operator's command with great accuracy and minimum latency has to be developed, such as the anthropomorphic and therefore intuitive input device that we have already proposed in Chapter 3.

In this chapter, we propose a human-in-the-loop teleoperation system satisfying the first two requirements. Especially we focus on the ionic electroactive polymer-based actuator (*i*EAP), which is ultra-thin and requires only a few volts to drive, and therefore shows exceptional characteristics for safety and compactness.

However, applications of this type of actuators to human-robot-environment interactions have been limited yet, due to the difficulties in addressing the requirements. In the next subsection, we will discuss the previous efforts and limitations in using the *i*EAP actuators to get some hints for a new approach.

4.1.2. Background and literature study

Self-sensing ionic electroactive polymer actuators

The *i*EAP-based soft actuators are compliant and easily scalable into various shapes and sizes like other soft actuators. Also, they are compact, lightweight, and low-voltage-driven. Therefore, they have been suggested by many researchers as a promising candidate to be used for robust and safe grasping [121,122,123,124].

A challenge to using *i*EAP-based actuators is the perception of the actuator state by self-sensing functionality. To be precisely controlled, the information about the deformation of the actuator and the contact with the grasping object should be identified. Vision sensors (e.g., optical cameras) can capture the information [125]; however, the performance depends on the environmental condition and the use of the external sensor compromises the compactness and wearability of the actuator, and therefore, limits the potential applications. There have been approaches to leverage the electrical charge between the electrodes of the *i*EAP to estimate its deformation; however, this produced limited accuracy due to the coupling between the driving voltage and measured charge. To embed additional sensors into the *i*EAP, we have to minimize their form factor and stiffness considering the low mechanical strength of *i*EAP and its small generated force, not to compromise the actuator performance.

Haptic actuation mechanisms

There have been many different haptic actuation mechanisms for human-robot interaction. Depending on the hardware structure, they have been categorized into grounded devices, exoskeletons, and fingertip devices [126]. To be used for teleoperation with the wearable input device proposed in Chapter 3, the most compatible structure is the fingertip-type, since they minimally hinder the natural hand motions and therefore preserve the robustness of tracking them. This group of devices generates cutaneous stimulations on the fingertip to render the tactile sensations. Mechanical deformation of the skin induced by those devices has to be properly designed to deliver the desired haptic sensations. For example, we can render a sense of contact, pressure, and softness by generating controllable normal indentation on the fingertip skin. Stretch or tangential motion and vibration of the skin can be interpreted as friction and texture of the surface, respectively. Ideally, implementing as many actuation modes in as high magnitude as possible will result in the best performance of the device. However, at the same time, the form factor or structural complexity of the device generally increases according to higher generated force or more actuation modes. This compromises the advantage of the minimal hindrance of the fingertip-type devices to natural hand motions. To address this trade-off between the actuation performance and the structural compactness, the choice of a proper actuator is critically required.

Many wearable haptic devices are composed of rigid and bulky units which hinder the users' motion [126], but there are some works that use soft actuators such as dielectric elastomer actuators (DEAs) for compactness, lightweight, and biocompatibility. However, they require a driving voltage as large as several hundred or kilo-volts, which is not desirable for its potential safety risk. Ionic electroactive polymer actuators that are driven by a few voltages can be an alternative, however, due to the relatively low speed and small force level, they have been barely tried to be used to generate haptic stimuli. To use the *i*EAP actuator to generate tactile stimulus, hardware design optimization and control of the driving conditions (e.g., frequency) are required. From the previously discovered fact that the force threshold for tactile perception is highly dependent on the frequency [49], assuming the same small level of forces, it is more likely to perceive vibrotactile stimuli compared to the normal indentation or skin stretch. It means there is a potential to deliver binary information to the operator by generating a vibrotactile stimulus.

4.1.3. Overview

In this chapter, we propose an integrated teleoperation system for interactive control of the *i*EAP-based gripper to grasp an object, satisfying the aforementioned requirements. Firstly, we will discuss how to measure the deformation of the gripper by embedding the liquid metal-based soft sensor in the gripper with optimized dimensions. With the optimized design, we will achieve desirable size and sensitivity with minimal compromise of actuation. In addition, from the knowledge of the dynamic actuation model and the sensor model, attained from the measured sensor signal, a decision algorithm can be implemented to identify the gripper's contact state with the outer environment. This bi-functionality of the embedded sensor for measuring the deformation and the contact decreases the number of sensors enabling a more compact system. Then, a haptic device based on the low-voltage *i*EAP will be developed to deliver the binary information of the contact between the gripper and the object, which enhances the operator's cognition. For the teleoperation, we will use the tracking glove described in Chapter 3, which enables an intuitive operation, as an accurate input device. In the last part of this chapter, the overall integration of the system will be presented with a representative demonstration of picking and placing an object.

4.2. Perception of the target domain and haptic interface

4.2.1. Sensor integration

(a)

(b)

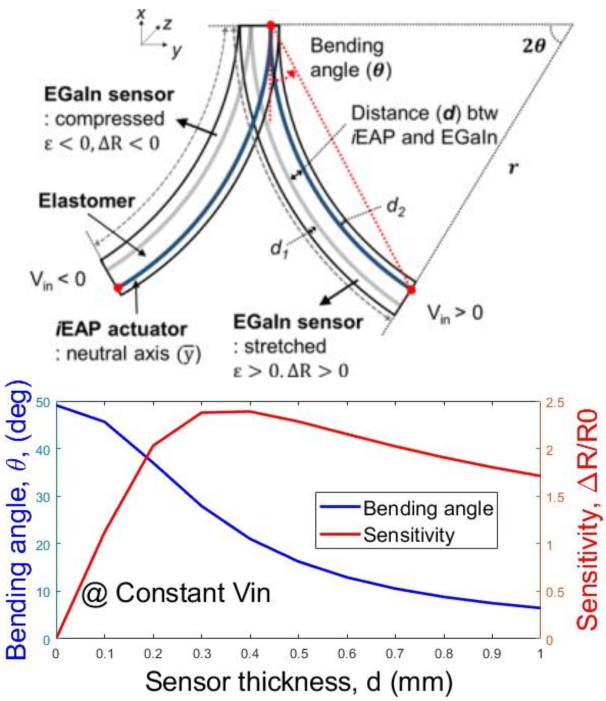

(c)

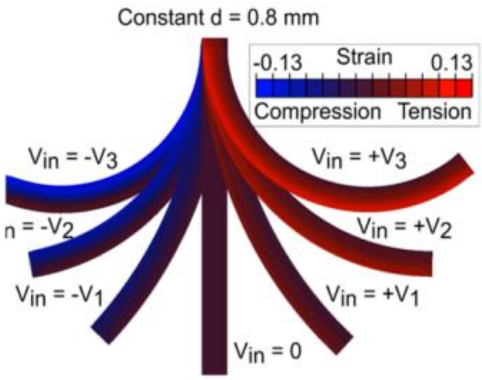

(d)

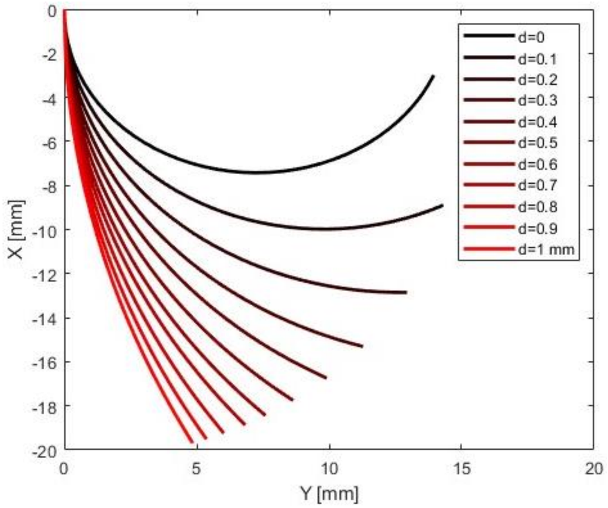

Figure 4.1. Design optimization for sensor integration: (a) Structure and electrical resistance changes of the sensor-integrated *i*EAP actuator under mechanical deformation. (b) Theoretical bending angle and sensitivity of the sensor-integrated actuators depending on the *d* value. (c) Deformation of the sensor-integrated actuator depending on the voltage inputs predicted by finite element analysis. (d) Deformation of the sensor-integrated actuator depending on the distance between the sensor layer and the *i*EAP layer (*d*).

Optimal design in consideration of sensitivity—deformation trade-off

Figure 4.1a shows the cross-sectional structure of the sensor-integrated *i*EAP actuator, where the layers of the *i*EAP actuator and the EGaIn sensor are embedded in the elastomer (Ecoflex 00-30, *Smooth-sil*) matrix. We defined the input voltage

(V_{in}) as positive when the actuator bent in the stretching direction of the sensor layer. Therefore, the expansion of EGaIn when $V_{in} > 0$ causes an increase in the resistance ($\Delta R > 0$), whereas the contraction of EGaln when the actuator bends in the opposite direction results in a decrease in the resistance ($\Delta R > 0$).

To amplify the sensor signal ($\Delta R/R_0$), the inner elastomer layer between the EGaIn sensor layer and *i*EAP actuator layer (d) has to be thick enough to induce a greater strain (ε) at the same bending angle (θ). The bending angle from the vertical axis can be measured by tracking the position of the actuator tip (marked by a red circle). However, when the elastomer layer becomes too thick, it will degrade the actuation performance (bending angle) due to increased bending stiffness. Therefore, the effect of d on the sensitivity and bending angle of the sensor-integrated *i*EAP actuator has to be investigated to optimize the design.

We tried to express the strain energy in terms of the thickness (d) and bending angle (θ), that are required to bend the entire structure. Assuming that there is no energy loss while the input electrical energy is converted to the strain energy, we will set the strain energy as constant and express the bending angle (actuation) in terms of the thickness (design parameter). Also, as we can calculate the resistance change of the eGaIn microchannel from the strain as in Chapter 2, we can express the sensitivity in terms of the design parameter.

First of all, the location of the neutral axis of the structure has to be identified to find the strain profile of the composite beam. The static equilibrium equation and the constitutive equations can be expressed as below;

$$\int \sigma \; dA = w\left(\int_{EAP} \sigma \; dy + \int_{ela} \sigma \; dy\right) \tag{4.1}$$

$$\sigma_{\mathrm{EAP}} = \sigma_{EAP}(\epsilon_{EAP}) = \sigma_{EAP}\big(\kappa(y, y^*)\big) = \sigma_{EAP}(\kappa, y, y^*) \tag{4.2a}$$

$$\sigma_{\mathrm{ela}} = \sigma_{ela}(\kappa, y, y^*) \tag{4.2b}$$

where σ_{EAP} and σ_{ela} are the (maybe nonlinear) stress—strain relations of the iEAP and the elastomer, respectively, κ is the curvature of the beam, y is the coordinate in the thickness direction, and the y^* is the position of the neutral axis. Solving the two equations, the neutral axis is determined by the curvature (or the bending angle from the geometrical relation, $\theta = \frac{L_0}{2}\kappa$, where L_0 is the actuator length) and the material properties of the two materials. It means the neutral axis changes during the bending motion of the actuator.

To simplify the system, we can linearize the stress—strain relations in **Equation 4.2**. In advance, we have to validate the availability of this linearization by approximating the maximum strain of each material and confirming that it is small enough.

Given the fixed thickness (0.05 mm) and length (20 mm) of the *i*EAP, the thickness of the elastomer (<1 mm), and bending angle ($|\theta|_{max}$ = 90°) of interest, the maximum strain of each material can be determined as

$$|\epsilon|_{max} = (1 \;\; mm + 0.005 \;\; mm) * \frac{2|\theta|_{max}}{20 \;\; mm} = 0.16 = 16\%, \tag{4.3}$$

up to which the linear model can represent the mechanics of the materials [127,128]. From the linear assumption, **Equation 4.2** can be simplified as

$$\sigma_{\mathrm{EAP}} \quad = \sigma_{EAP}\epsilon_{EAP} = E_{EAP}\epsilon_{EAP}^2 = \kappa^2 E_{EAP}(y - y^*)^2 \tag{4.3a}$$

$$\sigma_{\mathrm{elastomer}} \quad = \sigma_{ela}\epsilon_{ela} = E_{ela}\epsilon_{ela}^2 = \kappa^2 E_{ela}(y - y^*)^2. \tag{4.3b}$$

Then, substituting the **Equation 4.3** into **Equation 4.1** as

$$\int \sigma \ dA = w\kappa^2\left(\int_0^{d_2} \mathrm{E_{ela}}(\mathrm{y}-\mathrm{y}^*)^2 \ \mathrm{dy} + \int_{d_2}^{d_2+0.005} \mathrm{E_{EAP}}(\mathrm{y}-\mathrm{y}^*)^2 \ \mathrm{dy} + \int_{d_2+0.005}^{d_2+0.005+d+d_1} \mathrm{E_{ela}}(\mathrm{y}-\mathrm{y}^*)^2 \ \mathrm{dy}\right), \tag{4.4}$$

The position of the neutral axis can be identified in terms of the dimensional parameters (thickness of the elastomer covering the EGaIn pattern, d_1, and the thickness of the elastomer covering the iEAP actuator, d_2) and the design parameter (thickness between the EGaIn pattern and the *i*EAP, d) to be optimized.

Now given the neutral axis, the strain energy can be expressed as

$$\begin{aligned} U &= \int F du = \int \left(\int \sigma w dy \, L_0\right) d\epsilon \\ &= \int w\mathrm{L_0}\kappa^3 \left(E_{EAP}\int_{EAP} (y-y^*)^2 \, dy + E_{ela}\int_{ela} (y-y^*)^2 \, dy\right) dy \\ &= w\mathrm{L_0}\kappa^3 (d_2 + 0.005 + d + d_1) \\ &\qquad \left(E_{EAP}\int_{EAP} (y-y^*)^2 \, dy + E_{ela}\int_{ela} (y-y^*)^2 \, dy\right) \\ &= w\mathrm{L_0}\left(\frac{2\theta}{L_0}\right)^3 (d_2 + 0.005 + d + d_1) \\ &\qquad \left(\int_0^{d_2} \mathrm{E_{ela}}(\mathrm{y}-\mathrm{y}^*)^2 \ \mathrm{dy} + \int_{d_2}^{d_2+0.005} \mathrm{E_{EAP}}(\mathrm{y}-\mathrm{y}^*)^2 \ \mathrm{dy} + \int_{d_2+0.005}^{d_2+0.005+d+d_1} \mathrm{E_{ela}}(\mathrm{y}-\mathrm{y}^*)^2 \ \mathrm{dy}\right), \end{aligned} \tag{4.5}$$

where it is clearly shown that the actuation (θ^3) is inversely proportional to the design parameter (d^4), given a constant energy input U_0 (i.e., constant electric energy).

Assuming a constant volume of the inner elastomer layer, the sensitivity of the EGaIn strain sensor can be calculated as follows [129]:

$$\frac{\Delta R}{R_o} = (1 + \epsilon)^2 - 1 \tag{4.6}$$

Using **Equations 4.5,** and **4.6**, the bending angles and sensitivities of the sensor-integrated actuators with different *d* values in the range of 0–1.0 mm were simulated under a constant energy input. As shown in **Figure 4.1b**, with the increase in *d*, the bending angle decreases, whereas $\Delta R/R_0$ shows the opposite tendency. In other words, the greater distance of the EGaIn sensor layer from the *i*EAP actuator produced a higher sensitivity but a smaller bending angle. In this study, the *d* value was optimized to ~350 μm to create a sufficient bending angle by the actuation of the *i*EAP actuator and the high sensitivity of the EGaIn sensor layer.

Finite element analysis (FEA) was conducted using a commercialized software (Abaqus, Dassault Systems) to verify the model in **Equations 4.1—4.6** and **Figures 4.1a** and **4.1b**. The lateral dimension of the sensor-integrated *i*EAP actuator was set to be 20 mm × 5 mm while the thickness of the silicone substrate layer between the EGaIn channel and the *i*EAP actuator was varied from 0 to 1 mm with an increment of 0.1 mm. One end of the actuator was fixed, and a moment was applied to the other end to have the same internal energy of 0.0025 mJ. The displacement and strain along the length of the actuator were used to calculate the bending angle of the actuator and the change in resistance (sensitivity) of the embedded EGaIn channel. The material properties used in the analysis were determined experimentally; Young's modulus of the *i*EAP actuator was 650 MPa and the Yeoh coefficients of the silicone elastomer were C_1=1.366e-02, C_2=-2.588e-04, and C_3 = 8.889e-05.

As shown in **Figure 4.1c**, at a fixed *d* value of 0.8 mm, the *i*EAP actuator layer is subjected to the lowest strains (i.e., the neutral axis) at any pair of positive and negative V_{in} values. In contrast, the sensor layer underwent the largest deformation (stretching, colored in red; compression, colored in blue) under a given V_{in}.

In **Figure 4.1d**, the effect of *d* on the sensitivity and bending angle of the sensor-integrated *i*EAP actuator was also in agreement with the results from the mathematical modeling described in **Figure 4.1b**.

Sensor characterization

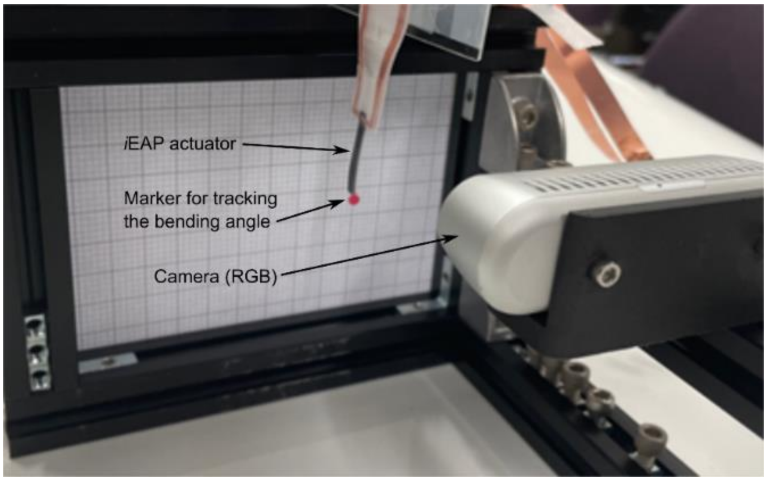

Figure 4.2. Experimental setup for characterization and control of the sensor-integrated *i*EAP actuator.

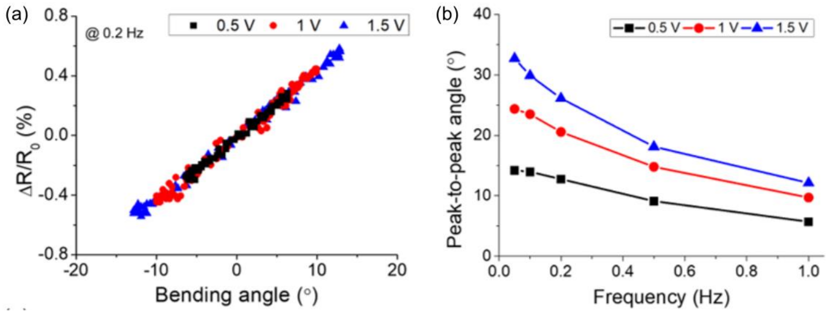

Figure 4.3. Sensor response to the actuator bending: (a) Linear relationship of the sensor

signal to the bending angle measured under various voltage inputs at 0.2 Hz. (b) Peak-to-peak bending angles of the sensor-integrated actuator as a function of the sine-wave voltage frequency.

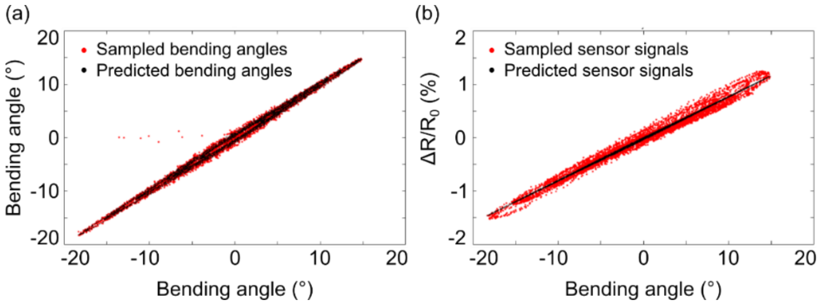

Figure 4.4. Linear fitting of dynamic and sensor model: (a) Sampled bending angles (red) and predicted bending angles (black) from linearly fitted dynamic model. (b) Sampled sensor signals (red) and predicted sensor signal (black) from linearly fitted sensor model.

The bending angle and the sensitivity of the optimally designed *i*EAP actuator were experimentally characterized with the experimental setup shown in **Figure 4.2**. **Figure 4.3a** further shows the consistency of the sensitivity under driving sinusoidal wave voltages of 0.5, 1, and 1.5 V at 0.2 Hz by showing an excellent linear correlation between θ and $\Delta R/R_0$ without hysteresis. Although increasing the frequency of the sine-wave voltages resulted in a reduction in the peak-to-peak angle (**Figure 4.3b**), the relation in which the angle increases with V_{in} was maintained. A high peak-to-peak angle of 12° was achieved at 1 Hz and 1.5 V, which is unprecedented for sensor-integrated actuators driven by an *i*EAP actuator, which constitutes only 6% of the total thickness.

The accurate measurement of the actuator motion in real time by the introduction of a liquid-metal sensor layer enabled active control of the sensor-integrated *i*EAP actuator by modeling the dynamic deformation and corresponding sensor signal

[130]. For this purpose, the θ and $\Delta R/R_0$ values were sampled under various sinusoidal voltage inputs with different amplitudes and frequencies, which were used to fit the discrete-time linear system model (**Figure 4.4**):

$$\begin{aligned} \theta_{k+1} &= A_d\theta_k + B_d V_{in,k} \\ \left(\frac{\Delta R}{R_0}\right)_k &= C_d\theta_k \end{aligned} \tag{4.6}$$

4.2.2. Tracking control

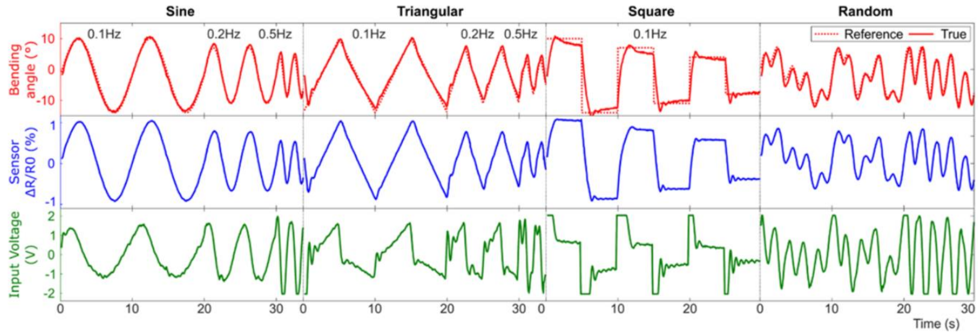

Figure 4.5. Tracking control following the pre-defined trajectories of various shapes and frequencies.

The sensor-integrated *i*EAP actuator was successfully controlled based on the identified system model to track a predetermined trajectory. **Figure 4.5** shows representative results, where the actuators accurately track the predefined target trajectories (dotted red curves) with various shapes (sine, triangle, square, and random) and frequencies of 0.1, 0.2, and 0.5 Hz. During tracking control, the input voltage was calculated using the model predictive control (MPC) method, which determines the optimal control in a receding time horizon [131].

4.2.3. Contact detection

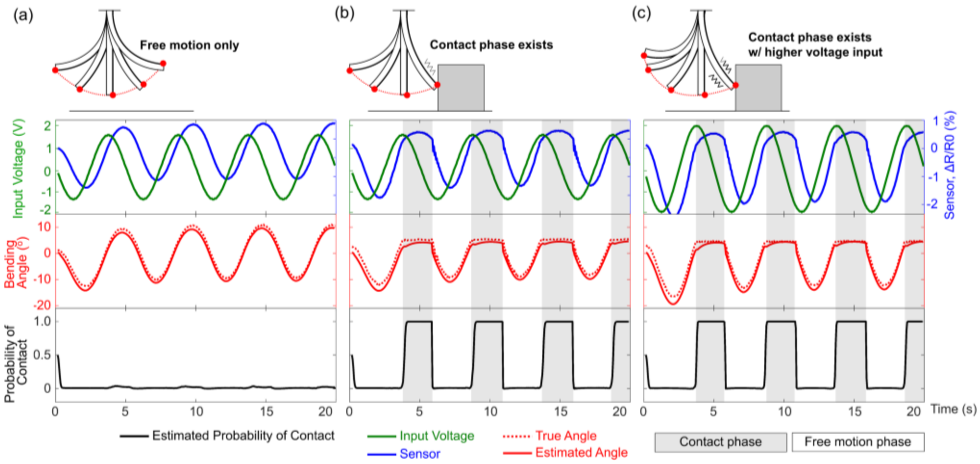

Figure 4.6. Interactive multiple model-based estimation for the motions of the sensor-integrated actuator: Estimating the contact phase of the sensor-integrated iEAP actuator by interactive multiple model (IMM) analysis during (a) free motion; (b) contacting an obstacle under various input voltages; (c) contacting an obstacle under increased input voltage.

In the case of the *i*EAP actuator used as a robotic gripper, the most important information is whether the gripper holds the object. Encouragingly, without the need to introduce additional sensors, our sensor-integrated actuator can statistically provide contact information, through the proprioceptive strain signal. We established two different system models based on the motion of the sensor-integrated actuator in two ways: free motion and contact phases. These can be distinguished by the strain sensor signal using the interactive multiple model (IMM) method [132]. To identify the dynamics of the contact motion of the *i*EAP actuator with an object, a 3d printed hexahedron block was placed on the side of the actuator so that the actuator could touch the block when the voltage was applied. The initial probability estimate was chosen as $\mu = [0.5, 0.5]$ and the transition matrix was designed as $\Pi_{ij} = \begin{bmatrix} 0.99 & 0.01 \\ 0.0001 & 0.9999 \end{bmatrix}$ (i for free motion, j for contact).

Figure 4.6 shows the representative results of the IMM estimation for the three different motions of the sensor-integrated actuator. Unlike the case of free movement without contact with the object (**Figure 4.6a**), a plateau of the bending angle was observed for the actuator during the contact phases even when the changed input voltage was continuously applied (**Figures 4.6b** and **4.6c**). However, the EGaIn sensor signal continued to change owing to the compressive force acting on the contact area of the EGaIn pattern, as well as further deformation of the actuator while its tip was fixed. Using these signals, the IMM estimates the contact phase (as the probability of contact in the bottom plots) to match the true state (shaded in gray when it is in contact).

4.2.4. Haptic interface

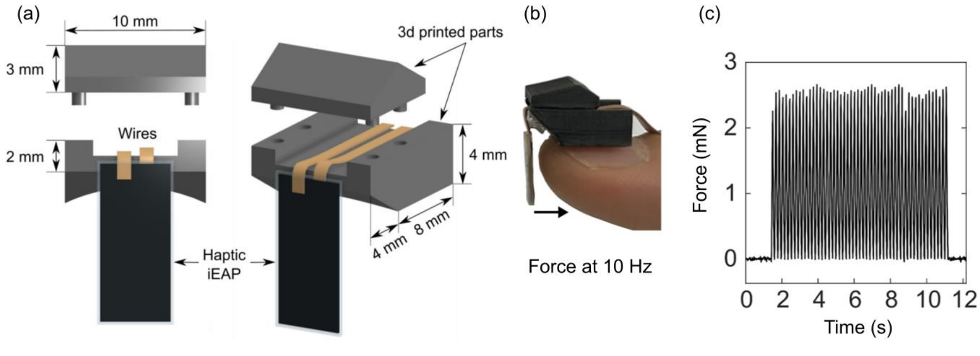

Figure 4.7. Haptic module design and generated force: (a) Cross-sectional images of the 3d-printed parts of haptic modules generated by 3d CAD rendering; (b) Prototype of the haptic *i*EAP module on the user's thumb; (c) Measured force at the fingertip at 2 V and 10 Hz.

The CAD design and prototype image of the haptic interface based on iEAP actuator are shown in **Figures 4.7a** and **4.7b**. The copper electrode was fixed to the surface of the iEAP actuator (16 mm × 3 mm), followed by the encapsulation with ~ 80 μm thick elastomer layer. In order to firmly anchor the haptic module to the fingertip of the user, two parts were designed using a 3d printer (Mark Two, Markforged). The bottom part was attached to the fingernail using commercial double-sided tape. The upper part was mechanically assembled with the bottom one to fix the electrode wire.

When the module is turned on, the *i*EAP actuator vibrates at 10 Hz to provide stimuli to the fingertip. The normal force measured by the haptic *i*EAP module at 2V and 10 Hz is shown in **Figure 4.7c**.

4.3. Integrated teleoperation system

4.3.1. System schematics

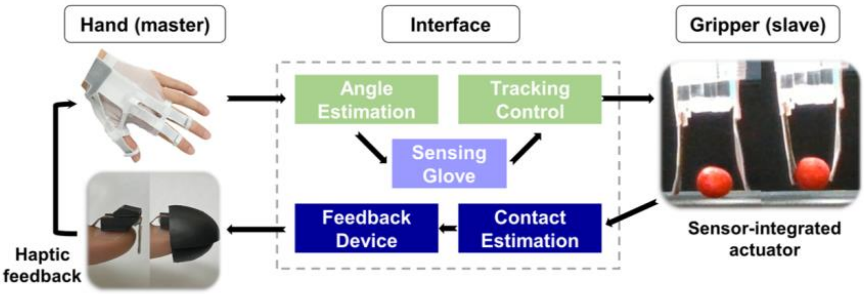

Figure 4.8. Schematics of a teleoperation system for *i*EAP grippers with a human hand with haptic feedback.

Figure 4.8 schematically illustrates haptic interaction systems based on sensor-integrated *i*EAP actuators and a wearable fingertip *i*EAP haptic feedback device.

We composed the system with three main components: a human hand wearing the sensing glove, soft gripper made of sensor-integrated actuators, and thimble-type haptic device for providing feedback to the fingertip. Each part is connected to another through the interface and cohesively operated inside a closed loop. When bending the finger while wearing the sensing glove, the sensor signal appears as a change in the electrical resistance, and a tracking control is generated to synchronize the finger motion with the actuator motion. This allows the user to intuitively give commands to the gripper. The contact states between gripper and the grasping object are transmitted to the user in real time via the haptic interface.

4.3.2. Finger-tracking control by teleoperation

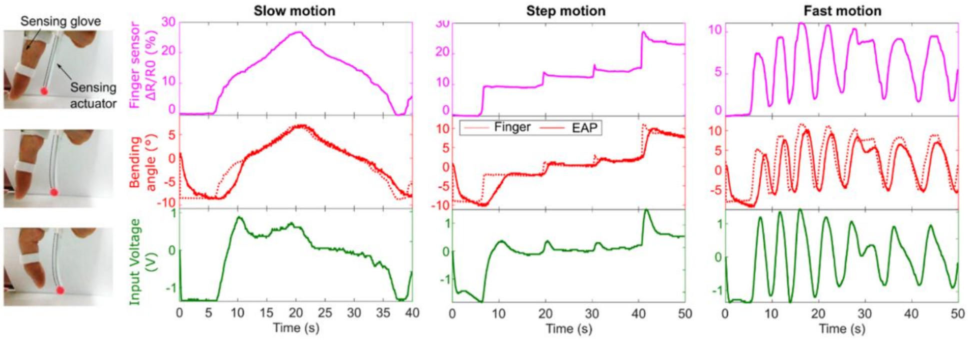

Figure 4.9. Teleoperation of the sensor-integrated *i*EAP actuator, following the motion of a human finger in real-time.

As shown in **Figure 4.9**, the sensor-integrated *i*EAP actuator is controlled to follow the joint motion of a human finger (see images), measured independently using a wearable sensing glove. The measured signal was transformed to the target bending angle of the *i*EAP actuator (dotted red curves) using pre-determined mapping in real time. The calculated bending angles were entered into the same MPC controller used in **chapter 4.2.2** and **Figure 4.5**, as a receding reference for each time step. As shown in the figure, the sensing actuator follows the slow (0.03 Hz), step (0.1 Hz), and fast (0.2 Hz) motions of the finger. The delay between the target trajectory generated from the finger and the controlled motion trajectory of the actuator is attributed to the size of the time window of the reference bending angles [133]; this can be resolved by reducing the window size. However, this will increase the tracking error because the identified dynamics in **Equation 4.6** cannot be fully utilized.

4.3.3. Demonstration

Experimental setup

Two sensor-integrated *i*EAP actuators (20 mm × 5 mm) were placed facing each other with a 15 mm gap. The gripper was fixed on the 2-dof moving stage to convey the ball from start point to goal point. The ball was made of polystyrene with the weight of ~50 mg. To simplify the system, the path of the gripper was set to advance towards the goal point. The user wearing sensing glove was asked to toggle a manual switch when he/she decided to start moving the gripper along the planned path. Range of the sensor signals from the sensing glove and the targeted maximum bending angles of the *i*EAP actuators were determined beforehand. The finger sensor signals and the bending angles were linearly mapped, enabling the calculation of the target bending angles for teleoperation from the user's joint motions. The haptic *i*EAP module was attached to the user's thumb, which was activated to vibrate at 10 Hz when the IMM estimator detected the contact between the *i*EAP actuator and the ball. The entire demonstration including the teleoperation and the haptic activation was automatically operated by an integrated system except for the positioning of the gripper towards the goal point.

Results

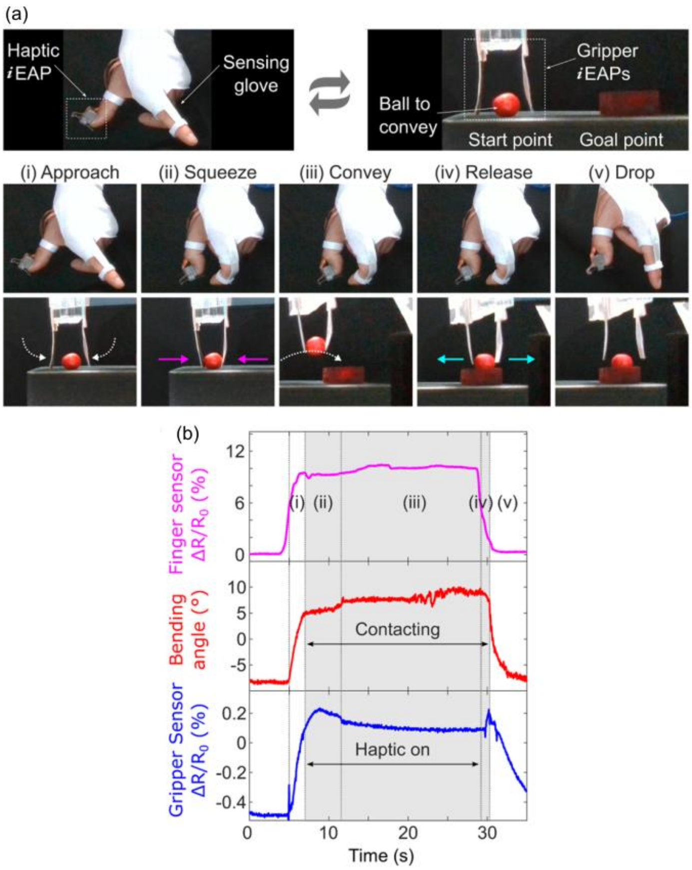

Figure 4.10. Demonstration of the teleoperation of a soft gripper: (a) Interactive teleoperation of sensor-integrated *i*EAP actuators with real-time haptic feedback for conveying a ball. Five steps to perform the task are shown. (b) Measured finger sensor signal, bending angle, and gripper sensor signal while completing the task.

The bottom panel of **Figure 4.10a** shows the interactive teleoperation of the gripper by the human hand in performing five tasks. First, the gripper approached the ball by tracking the target angles, which were calculated from the finger motion tracked using the sensing glove. When the gripper started to contact the ball, the user bent the fingers to squeeze the ball for a stable grasping motion. The user then conveyed the ball to the goal point to release and drop it.

Figure 4.10b shows the measured states of the system upon task completion. When the gripper was in contact with the ball, the sensor signal of the gripper changed significantly. Once this difference was detected by the IMM algorithm, the haptic *i*EAP module was activated to provide tactile feedback to the user. Based on this tactile feedback, the user could decide whether to squeeze further or move the ball to the goal point. When the ball was released from the gripper, the gripper signal showed a peak owing to frictional resistance and static attraction. Contact with the ball was communicated to the tip of the thumb as a tactile feedback signal by the haptic *i*EAP module.

Notably, in the absence of haptic feedback, users have to rely on visual information, making it difficult to confirm the stable grasping motion. For example, when gripping through point contact or when trying to grasp a fragile object, it is important to apply an appropriate level of grip force [134].

4.4. Discussion

In this chapter, we have been using *i*EAP actuators, which are lighter, safer, and have a smaller form factor compared to other types of actuators, to deliver haptic feedback for the interactive teleoperation of a soft gripper. It has been known to be difficult to use the *i*EAP as a haptic actuator due to its relatively smaller force and slower actuation speed compared to other types of actuators. Many review papers assumed that the force generated by the *i*EAP was not enough for cutaneous stimuli that are perceivable by humans [126,135]. However, recent progresses in the actuator technology are showing enhancement in the force level and the actuation speed, which widens the potential application area. In this section, we will discuss the practicability of using the *i*EAP actuators for haptics.

First of all, we will examine whether the force level shown in **Figure 4.7c** is sufficient for perception. In the field of haptics, human subject tests play an important role in proving the effectiveness of the stimuli rendered. However, we let the human subject test for our device to be a future work, but instead, here, we refer to the related literature to indirectly verify its effectiveness. Generally, force in order of 10—100 mN is considered to be a threshold for cutaneous haptic perception [135]. However, the threshold is highly dependent on the frequency of the signal. Also, Baelen et al. experimentally showed that the perception threshold (Just noticeable difference, JND) for asymmetric vibrotactile force in time and amplitude is lower than that for the symmetric one [136]. According to this research, the JND of the suggested asymmetric contact force was 0.094 mN at 2 Hz, which can be generated by our *i*EAP actuator. The sensitivity to detect the tactile stimulus becomes even better when visual information is provided during the grasping task in a virtual environment, just as in our teleoperation setup, as proven by Juravle et al. [137]. Furthermore, Zhao et al. observed the decreasing detectable voltage threshold of haptic DEA in higher frequency, even though is generates smaller blocking force [138]. Based on these works, we were able to conclude that our *i*EAP-based haptic device can generate enough force and frequency to deliver tactile stimulus. Furthermore, we can find a possibility of the enhancement of the performance by optimization of the blocking force and frequency of the *i*EAP.

For optimization of the blocking force and the frequency, diverse approaches can be employed such as improving the fabrication method for electrode or electrolyte and changing the dimensions. Depending on the various manufacturing methods, the blocking force of the iEAP actuators ranges from 0.98 to 198 mN according to a survey paper that was recently published [139]. One of the promising technologies for enhancing the blocking force is to add an encapsulation layer to the actuator. As implied in **Figure 4.1**, an additional layer degrades the actuation performance but also increases the stiffness of the structure, resulting in a larger blocking force. As shown in **Figure 4.11**, we experimentally confirmed this hypothesis by comparing the blocking force of the same *i*EAP actuator measured before and after coating the elastomer (Ecoflex 00-30) layer.

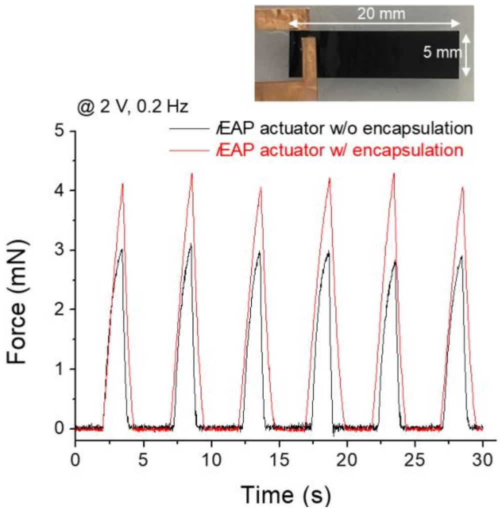

Figure 4.11. Increased blocking force of the *i*EAP actuator after encapsulation.

We also compared the blocking forces of the *i*EAP actuators that are encapsulated by using various materials or methods from the literature. Since the reported blocking forces from different publications have to be appropriately normalized to compensate for the dimensional variation, three different metrics were used as the normalization factor, as shown in **Table 4.1**.

Table 4.1. Blocking forces of various iEAP actuators with encapsulation technologies.

Ref.	F_{bl}	l	w	t	$\frac{F_{bl}}{wl}$	$\frac{F_{bl}}{wt^2/l}$	$\frac{F_{bl}}{t}$
					Normalized F_{bl} by		
Physical meaning	Blocking force	Length	Width	Thickness	Contact area	Dimensional factors in theory [146,147]	Thickness
Unit	Nm	mm	mm	mm	kPa	MPa	N/mm
Ours	2.5	16	3	0.15	52.1	592.6	88.9
[140]	6.5	54	20	0.3	6.0	195	58.5
[141]	9	40	5	0.7	45.0	147.0	102.8
[142]	70	15.1	10.2	1.2	454.5	72	86.3
[143]	0.4	3	0.8	0.2	166.7	37.5	7.5
[144]	3.2	25	3	0.32	42.7	260	83.3
[145]	4.5	20	5	0.34	45	155	52.9

Table 4.1 and [139] suggest a large space for designing the *i*EAP-based haptic actuators with different manufacturing and encapsulation technologies. As the encapsulation method suggested in **Figure 4.11** was not optimized at all, further study on the material or geometry of the coating layer would be another future work.

Chapter 5

Perception for Adapting Soft Grippers to Unknown Environment*

5.1. Introduction

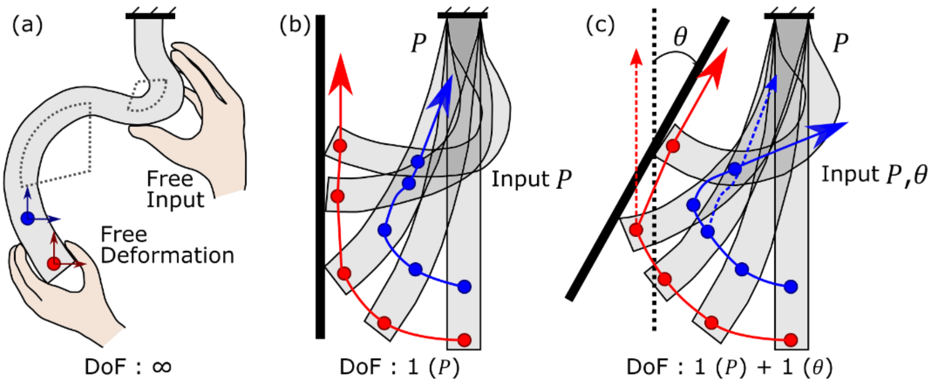

Figure 5.1. Degrees of freedom (DoF) of an elastic beam: (a) An elastic beam can be deformed freely with an infinite number of DoFs in general. However, when the control input of the beam and the environment are fixed, only a finite number of DoFs are necessary to describe its shape. (b) For a pneumatic bending actuator of one pressure input and a fixed environment (i.e., wall), only one variable is sufficient for describing the system. (c) If the environment has its own DoF, the system has an extra DoF.

* The contents in this chapter have been published in [148].

5.1.1. Motivation

Compared to conventional robots made of motors, rotational joints, and rigid linkages, soft robots are composed of compliant materials and structures. A remarkable feature of soft robots is that they can deform both actively and passively to conform to various shapes of objects to be gripped. From the kinematic point of view, soft robots can generate complex motions with high degrees of freedom (DoFs) at a small cost (in terms of the number of actuators or control inputs) by utilizing their inherent property of compliance [149,150,151]. Considering the necessity of versatile interactions between robots and environments, this feature is highly advantageous as robots can easily change their physical configurations depending on the surroundings and situations whether intentionally or unintentionally. Furthermore, the structural compliance allows for interactions with the environments in a passive and adaptive manner so that the safety of both the robots and the surroundings including humans can be guaranteed. These advantages of compliance have encouraged researchers to incorporate compliant mechanisms into various applications. Object manipulation is one of the most widely explored areas, and the first step of manipulation is to grip an object [152,153,154]. To successfully grip the target object in this case, the robotic system needs to adapt its shape to the object only with a limited number of active DoFs (i.e. actuators) [155,156,157].

5.1.2. Background and literature study

There has been an approach to address this problem using under-actuated robotic hands that can easily conform various objects with different shapes

[158,159,160]. In this case, most studies have focused on analyzing the static models of the robots to figure out the generated forces and the geometries for determining the best design parameters for given tasks [161,162]. A mechanically programmable design with mechanical selectors incorporated in an under-actuated robotic hand has also been proposed to extend the grasping capabilities [163]. However, the rigid link-joint structure inevitably constrained the motion of the robots and limited the reachable target regions in these approaches. Some researchers have partially adopted elastic elements into the structure to address the above limitation, in which the physical constraints can be averaged out at the desired configuration [164].

5.1.3. Dimension reduction and hybrid modeling for soft grippers

However, soft robotic hands that are fully (or mostly) composed of elastic materials have a much higher capability of handling various objects thanks to their unconstrained deformation with an infinite number of DoFs [165,166,167,168]. Although various types of soft robotic hands or fingers have been developed, analysis of the extended grasping capability has not been investigated enough yet. The difficulty comes from the complex configuration or the nonlinear kinematics of the structure with a large number of DoFs. Compared to a conventional rigid robot whose body configuration can be clearly expressed with a finite number of joint angles, the analytic expression for the configuration of a soft robot in general requires many approximations or a high computational power [169,170,171,172]. An accurate but fast analysis of the system if possible will be thus highly useful for performing high-level manipulation tasks. The good news is that we can describe the system only with a small number of state variables despite the large number of DoFs as long as the task or the environment is defined. To be specific, the number of the states can be determined by the dimension of the given environment. Therefore, instead of trying to develop a general infinite dimensional model for a soft robot, analyzing its reduced form based on the given environmental conditions will offer greater efficiency in modeling.

In the case of a simple elastic beam that could be a basic form of a soft gripper's finger, shown in **Figure 5.1**, an infinite number of curvature variables (continuous distribution) are necessary to describe the state (i.e. shape) of the beam (**Figure 5.1a**). However, once the control input and the environment of the system are defined, only a finite number of variables will be enough. For example, a pneumatic bending actuator with a single pressure input and a fixed environment (i.e. wall) (**Figure 5.1b**) needs only a single variable to express the state, since there exists only a single state. This means the distributed curvatures along the length of the finger are fully coupled with each other, and the coupled motion can be determined by the single input. Although the shape of the actuator can no longer be expressed by the single state if the environment has its own DoF (**Figure 5.1c**), it still requires a finite number of states. Therefore, the infinite dimensional configuration space of the elastic beam can now be reduced to a finite dimensional space, allowing us to analyze the system more accurately and efficiently, which is highly useful in practical applications with soft robots.

In this chapter, a gripper system composed of a soft robotic finger and an object will be expressed as a dynamic system with a state variable x and an input u. In general, the state evolution of a continuous system can be written with a differential equation as

$$\dot{x} = f(x, u). \tag{5.1}$$

However, in the case of the system in **Figures 5.1b** and **5.1c**, the motion of the finger starts to deviate from its original trajectory upon contact even though the trajectories shown in the figure are continuous. Such system with two distinguished states can be simply described with an additional discrete state variable as

$$\dot{x} = f(q, x, u). \tag{5.2}$$

The variable q indicates whether the system (i.e. finger) is in contact with the environment (i.e. wall) or not. The system described in **Equation 5.2** is called a hybrid system, in which there exist both continuous and discrete state variables [173,174]. This approach has been frequently adopted for analyzing motions in conventional robotics that switch their states or "modes" of the motion [175,176,177].

Given the system expressed in a hybrid model, comes back the problem to estimate the hybrid states. In other words, a sensor (or a limited number of sensors) needs to both detect a contact and estimate the shape of the finger. Although visual tracking systems have been widely used as a method of feedback in this type of problems, they are sometimes limited due to the need of additional devices or spaces, and some of them are even slow, expensive and inaccurate [178,179,180,181]. In this work, by taking advantage of the deformable feature of the soft robot, we estimate the high dimensional but coupled states of the system using a single embedded proprioceptive soft sensor [182,183,184,185]. The concept of proprioception comes from biological muscle systems, where a muscular unit internally detects its stretch or stress by the embedded sensing elements inside, such as muscle spindles or Golgi tendon organs [186,187]. We first understand how the deformations (outputs) are distributed along the finger according to the state, and then we suggest the estimation strategy based on the mapping from the state to the outputs.

5.1.4. Overview

The chapter starts with a simplified problem and its modeling of the soft gripping system, followed by the definitions of the state space for the hybrid system and the task to be performed. Experiments were then conducted to characterize the deformation according to the input of the system. The result determines the sensor placement and the estimation strategy. Finally, the control result for the gripping task is presented, which validates the core contribution of this study: Estimation of hybrid states of a soft robotic system using a proprioceptive sensing mechanism.

5.2. System definition and modeling

5.2.1. A robotic gripper

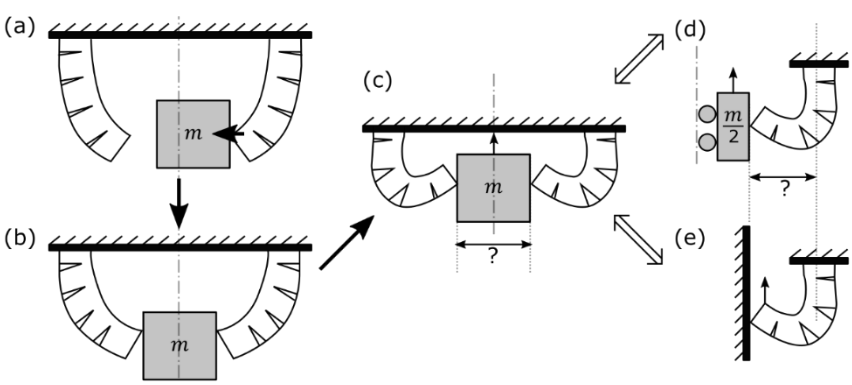

Figure 5.2. Definition of an object manipulation problem with a soft pneumatic gripper: (a) An object at an arbitrary position between two fingers can be (b) aligned to the center line by increasing the internal pressures of both fingers equally. (c) The gripping motion by the two fingers is equivalent to (d) a lifting-up motion of half of the object in the vertical direction or to (e) a climbing-up motion of the fingertip on a frictionless wall assuming both the force generated by the finger and the friction between the finger and the object are large enough.

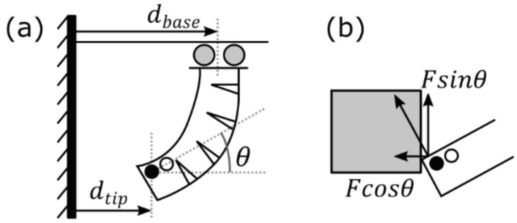

Figure 5.3. Definition of task space variables: (a) Definition of the coordinate system and the configuration variables. (b) The tip orientation (θ) of the finger is important as it determines the direction of the gripping force.

The problem we are interested in modeling with a hybrid system approach is a soft robotic gripper with a simple manipulation task of lifting up an object, as described in **Figure 5.2**. A robotic gripper with two soft pneumatic actuators (i.e. fingers) and an object to be gripped are shown in **Figure 5.2a**. We assume that the shape of the target object is cubic for simplicity in this problem but leave the size and the position of the object unknown. To grip the object, the actuators can move in the horizontal direction. When we pressurize both fingers, the object is moved to the center between the two fingers (**Figure 5.2b**). If the pressure further increases, the bending motion of the fingers generates forces in both the horizontal and the vertical directions, resulting in lifting up the object (**Figure 5.2c**). We can simplify the system to a half based on the symmetry, replacing the object with a new one that weighs a half of the original object, and can move the new object freely only in the vertical direction (**Figure 5.2d**). Assuming the mass of the object is small and the force generated by the finger and the friction between the fingertip and the object are both large enough, we can consider only the kinematics of the finger. Then, the system for analysis and modeling is equivalent to a single pneumatic bending actuator climbing up a fixed vertical wall without friction (**Figure 5.2e**).

The simplified system with variables is shown in **Figure 5.3**. The only difference in this configuration from **Figure 5.2e** is that the base has an active DoF in the horizontal direction. Depending on the distance to the wall (or the object), the base of the finger can approach or retreat from the wall to find an optimal location for successfully climbing up (i.e. gripping the object). d_{base} and d_{tip} are the distances to the wall from the base and from the tip of the finger, respectively, and θ is the bending angle of the finger measured by the black and white dots at the tip about the horizontal axis, which is important for successful gripping since it determines the direction of the force (**Figure 5.3b**).

5.2.2. States and measurements of the system

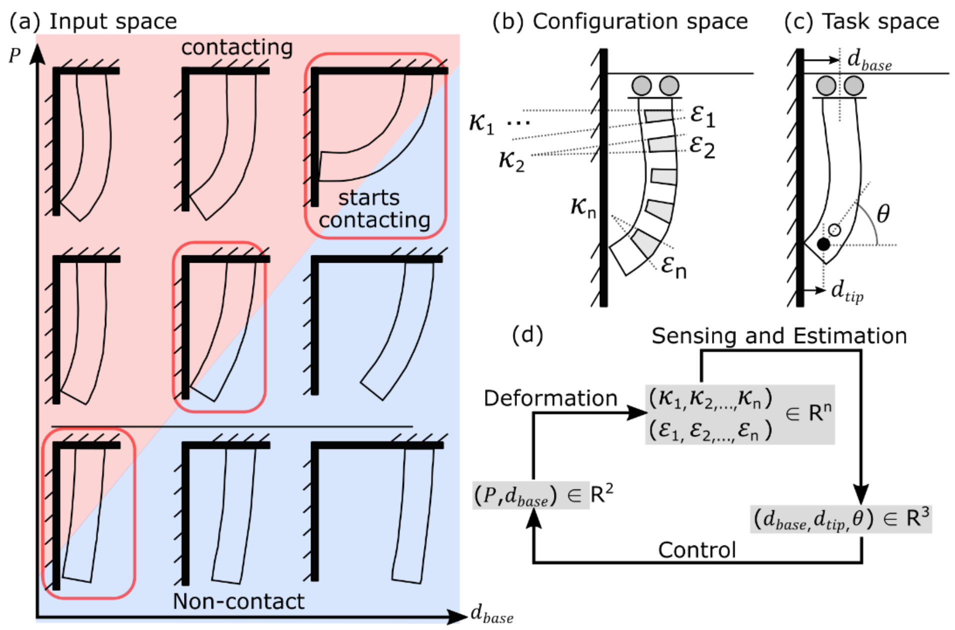

Figure 5.4. Three-state spaces of the system: (a) Input space (P, d_{base}) and the shapes of the actuator with different input pairs. A contact occurs in the upper-left region (pink area) of the plot. (b) The configuration space of the actuator can be expressed with n piecewise constant curvatures or strains. (c) The task space of the actuator. (d) The variables in each space can be transformed into those in the other spaces. The loop schematically describes how the estimation and control of the system occurs.

To successfully complete the gripping task, the system needs to find the right values for d_{base} and θ. Since θ is determined by the input pressure P to the actuator although d_{base} can be directly adjusted, P and d_{base} become the system inputs. To close the loop for control, we now need real-time information on d_{tip} and θ for estimating the control variables d_{base} and θ. Although they can be easily measured by visual tracking, incorporating vision data into an on-line controller makes a system slow, bulky and expensive in general. We thus used a simple proprioceptive soft sensor embedded in the finger for measuring local strains, to estimate d_{tip} and θ in real time, which will be discussed later.

By adjusting the system inputs P and d_{base}, we can achieve different physical configurations of the finger, as shown in **Figure 5.4a**. A contact between the tip and the wall can be made by increasing P or by decreasing d_{base}, and the configurations of the finger that just start making a contact are shown in the diagonal elements in red circles. **Figure 5.4b** shows the actuator bending and making a contact with the wall. The shape of the finger can be determined by the curvature distribution along the length, which can be discretized into the n piecewise constant curvatures. The n curvature values can be obtained from n strains of the corresponding segments on the finger. Since it is enough to estimate the task space variables (**Figure 5.4c**) if the measurable dimension of the configuration space is larger than the dimension of the input space, we can utilize the estimated values for control. The overall procedure is described in **Figure 5.4d**.

5.3. Hybrid system analysis

In this section, we formally define the system in **Figure 5.3** and suggest a control strategy for gripping. The system cannot be described as a simple continuous system, since its dynamics and the sensor responses are different depending on whether there is a contact or not. We first define three discrete states of the actuator.

5.3.1. Discrete states for the actuator

$$\boldsymbol{q} = (q_1, q_2, q_3) \in \mathbb{Q} \tag{5.3}$$

$$
\begin{aligned}
\mathbb{Q} = \quad & \{(\text{non-contact, pressurize, stay}), \\
& (\text{contact, pressurize, stay}), \\
& (\text{non-contact, depressurize, approach}), \\
& (\text{non-contact, depressurize, retreat})\}
\end{aligned} \tag{5.4}
$$

where $q_1 \in$ {non-contact, contact}

: contact status of the finger with the wall,

$q_2 \in$ {pressurize, depressurize}

: status of pressure input to the finger,

and $q_3 \in$ {approach, retreat, stay}

: motion of the finger base.

The discrete states have only four values, as shown in **Equation 5.4**. The system undergoes discrete 'transition' or 'jump' from one state to another. In between the jumps, i.e. while the system is not moving in a single discrete state, the evolution of the continuous states occurs, which needs to be defined.

5.3.2. Continuous states

$$X = \left(P, d_{base}, d_{tip}, \theta, \tau\right) \in \mathbb{R}^5 \tag{5.5}$$

where $P \in [0, P_{max}]$: Input pressure,

$d_{base} \in \mathbb{R}_+$: finger base position (distance from the wall),

$d_{tip} \in \mathbb{R}_+$: fingertip position,

$\theta \in \mathbb{R}$: fingertip orientation (angle),

and $\tau \in \mathbb{R}_+$: internal clock time between transitions.

With the defined discrete and continuous states above, the gripping task can be formulated.

5.3.3. Task

$$
\begin{aligned}
&\text{Reach} \quad \tau > T_{move} \\
&\text{While} \quad \big(q = (contact, pressurize, stay)\big) \\
&\qquad\quad\ \wedge (\theta \leq \theta_{max}) \\
&\qquad\quad\ \wedge (P \leq P_{max})
\end{aligned}
\tag{5.6}
$$

It is regarded as a success when the actuator climbs up the wall (i.e. pressurizing) for a longer period than T_{grip} while maintaining the contact in the upward direction ($\theta \leq \theta_{max}$), where θ determines the direction of the force from **Figure 5.3**. Since the upper limit of the angle guarantees the lifting up motion of the actuator, we can assume the gripper is carrying out both grasping and lifting motions. However, the functional requirements could be different depending to the situations while the formulated task defined here represents only one example among many. To complete the task, we have to control the system so that the state evolves in a proper direction. The control input variables, either discrete or continuous, are defined here.

5.3.4. Inputs

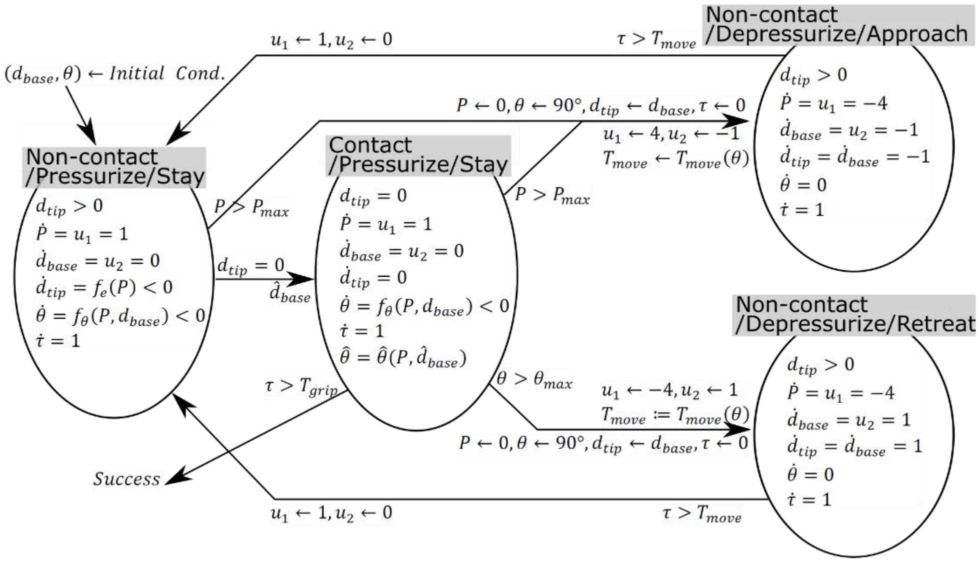

Figure 5.5. Hybrid system with four discrete states: The transitions between the states are expressed with arrows. A guard condition to enable a transition to another state was provided in the beginning (tail of the arrow) of each transition, and a reset map for the state after the transition was provided at the end (head of the arrow) of the transition. Continuous evolution of continuous states is formulated inside each discrete state.

$$u = (u_1, u_2, T_{move})$$

$u_1 \in \{1, -4\}$: Pressure differential (pressurize, depressurize)

$u_2 \in \{1, -1, 0\}$: Base position (distance) differential (approach, retreat, stay) (5.7)

$T_{move} \in \mathbb{R}_+$: Time for base moving (5.8)

In **Figure 5.5**, the transitions between the discrete states are represented by the arrows and the continuous evolution (dynamics) is formulated inside the states. The condition for the transition and the reset map of each transition is shown in the beginning (tail) and the end (head) of the arrow, respectively.

5.3.5. Continuous evolutions

Increase or decrease of the internal pressure of the finger is determined by u_1 ($\dot{P} = u_1$), and the relative motion between the wall and the actuator is determined by u_2 and T_{move}. Before the internal clock ($\dot{\tau} = 1$) reaches T_{move}, the wall moves in the direction of u_2. The remaining variables d_{tip} and θ evolve in an autonomous manner inside each state.

5.3.6. Guard Condition, Reset Map, and Discrete Transitions

1. (*non-contact, pressurize, stay) → (non-contact, depressurize, approach*): If the internal pressure of the finger reaches the maximum value before contact occurs, it means that the finger is located too far away from the wall to grip the object. The finger approaches the wall for T_{move} with depressurization (transition occurs). Since there is no measured θ at this point, T_{move} is set as a preset constant.

2. (*non-contact, pressurize, stay*) → (*contact, pressurize, stay*): During the state (*non-contact, pressurize, stay*), the sensor signal keeps being evaluated to detect the contact. When a contact is detected, the position of the finger base is estimated ($\hat{d}_{base}$) from the input pressure at the moment and stored. The transition occurs, and the tip orientation is estimated ($\hat{\theta} = \theta(P, \hat{d}_{base})$).

3. (*contact, pressurize, stay*) → Task completion: While maintaining a contact, increase of the input pressure for T_{grip} means a success of the task.

4. (*contact, pressurize, stay*) → (*non-contact, depressurize, approach*): If the input pressure reaches the maximum value before T_{grip}, it means that the actuator is too far away from the wall to grip the object. The actuator then approaches the wall for

T_{move} with depressurization (transition occurs). The estimated $\hat{\theta}$ in the former state determines the duration to move (T_{move}).

5. (*contact, pressurize, stay*) → (*non-contact, depressurize, retreat*): If the estimated $\hat{\theta}$ is larger than θ_{max}, it means that the finger is too far away from the wall to grip the object. The actuator retreats from the wall for T_{move} with depressurization (transition occurs). The estimated $\hat{\theta}$ in the former state determines the duration to move (T_{move}).

6. (non-contact, depressurize, approach) / (non-contact, depressurize, retreat) → (non-contact, pressurize, stay): After adjusting the distance (d_{base}), go back to the initial state and repeat the procedure.

5.4. Sensor placement, contact detection, and estimation

Control of the above system (i.e. determining $u_1, u_2,$ and T_{move}) requires estimation of the continuous states. The internal pressure *P* and the clock τ can be measured directly from the pressure regulator of the pneumatic pump and from the control loop, respectively. However, the geometric states of the actuator, such as the base and the tip positions (d_{base} and d_{tip}) and the orientation (θ), need to be estimated from the measurement of physical deformation, which requires a soft sensor to be embedded in the actuator. As discussed in **Figures 5.4a** and **5.4b**, the two-dimensional inputs (*P* and d_{base}) determine the configuration of the actuator whose shape can be expressed by *n*-dimensional curvature distribution. In this work, we set five candidate locations for the soft sensor (i.e. *n*=5) that are equally spaced along the length of the actuator, and then find the best location among the five by experimentally characterizing the task and the configuration spaces of the actuator. After embedding the sensor at the selected location in the actuator, the task state variables are estimated using the characterization data of the soft sensor, and the estimated values are compared with the reference values.

5.4.1. Experimental setup and prototype

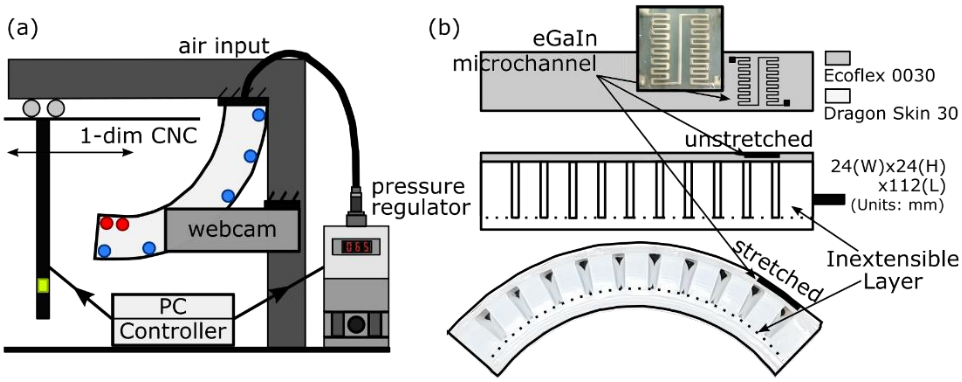

Figure 5.6. Experimental setup for testing: (a) Experimental setup. (b) Design of the soft actuator used in the experiment with an embedded proprioceptive soft sensor.

The experimental setup is shown in **Figure 5.6a**. To determine the sensor location, we used a vision tracking system first. The distance between the wall and the finger base (d_{base}) can be controlled by moving the horizontal position of the finger. However, for more accurate tracking of the finger motion, the position of the finger was fixed to maintain the same distance to the camera. We instead moved the wall installed on one-dimensional motorized stage, pretending the motion of the finger base. For vision tracking, multiple markers were attached on the actuator body and the wall. The green marker on the wall determines the origin of the system and the distance to the base (d_{base}). The red markers at the tip determine the position

(d_{tip}) and the orientation (θ) of the fingertip. The blue markers are for measuring local strains of the five candidate locations along the length of the actuator.

The design of the finger used in the experiment is shown in **Figure 5.6b**. On the top side of a pneu-net bending actuator [188], an extra silicone layer was attached for embedding a soft strain sensor [189,190]. The extra layer was made of a much softer elastomer material (Ecoflex 00-30, Smooth-On, 100% modulus: 69 kPa) than that of the remaining body of the finger (Dragon Skin 30, Smooth-On, 100% modulus: 593 kPa) so that the effect of the sensor layer on the bending stiffness is negligible. On the surface of the extra layer, embedded a microchannel filled with conductive fluid (eutectic gallium-indium, eGaIn) [190,191,192]. When the actuator is internally pressurized, bending occurs along the finger body with the inextensible layer on the bottom side of the finger being a neutral axis. Since the sensor layer on top is located off the neutral axis, the embedded microchannel is stretched with bending, resulting in increases of its electrical resistance that can be easily converted to a strain value.

5.4.2. Characterization of task and configuration spaces

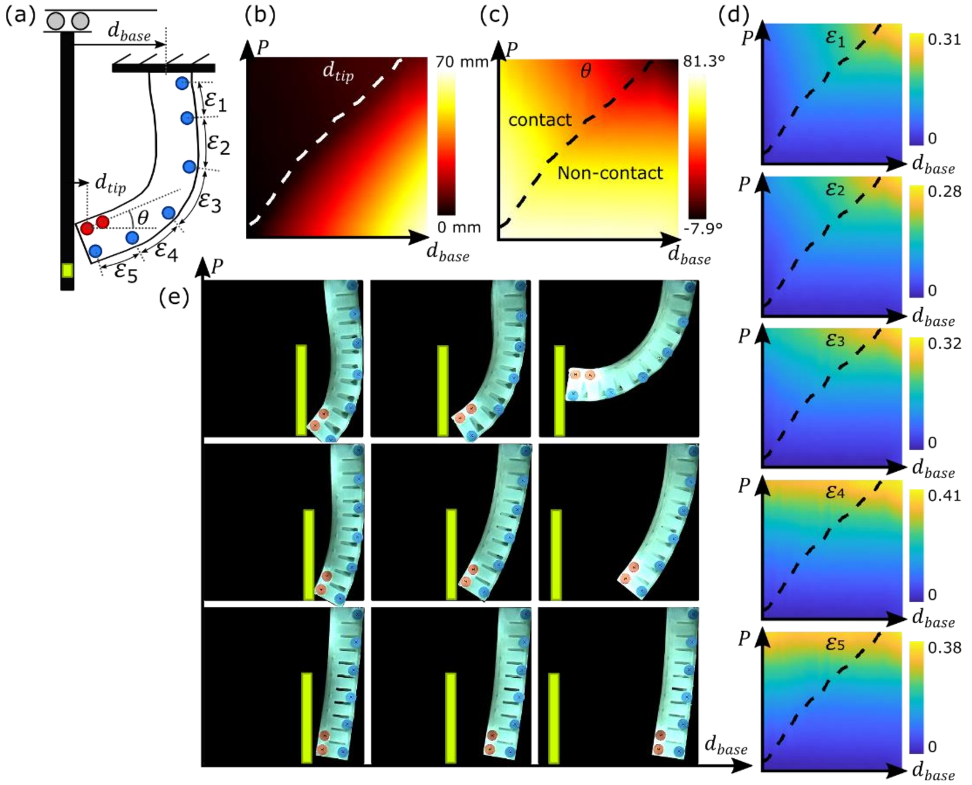

Figure 5.7. Characterization of the task and the configuration spaces: (a) Finger model with five sensor location candidates. Color map plots of (b) the position and (c) the orientation of the fingertip and (d) the strains at the five sensor locations with varied input pairs of P and d_{base}. The dotted lines are the boundaries of contact, which were determined from the tip position (d_{tip}) by vision data. (e) Shapes of an actual finger prototype with varied input pairs of P and d_{base}.

Figure 5.7 shows the characterization result with colormaps of the task space variables (d_{tip} and θ) and the configuration space variables ($\epsilon_1 - \epsilon_5$). All the data for characterization were collected by vision tracking in this stage. **Figure 5.7a** shows the finger model with five candidate locations for embedding a soft strain sensor. The dotted lines on the colormaps in **Figures 5.7b–5.7d** are the contact boundaries, where the fingertip starts to make a contact with the wall, determined by the tip position (i.e. $d_{tip} = 0$) from the vision data. As expected, only a small input pressure is required to make a contact if d_{base} is small, but a higher input pressure is necessary for a larger d_{base} for a contact (**Figure 5.7b**). Also, the tip orientation (θ) continuously changes along the contact boundary (**Figure 5.7c**). The strain plots in **Figure 5.7d** show that the closer to the base the sensor is located, the more the sensor signal is affected by d_{base}, indicating that ϵ_1 is the most effective location to estimate d_{base}, since we already know P as an input pressure. Therefore, we can reliably estimate the configuration variables, d_{base} and θ from ϵ_1 and P, respectively. **Figure 5.7e** shows the different behaviors of the actual finger prototype with varied input pairs of d_{base} and P, consistent with **Figures 5.7b** and **5.7c**.

5.4.3. Estimation of task space variables with embedded soft sensor

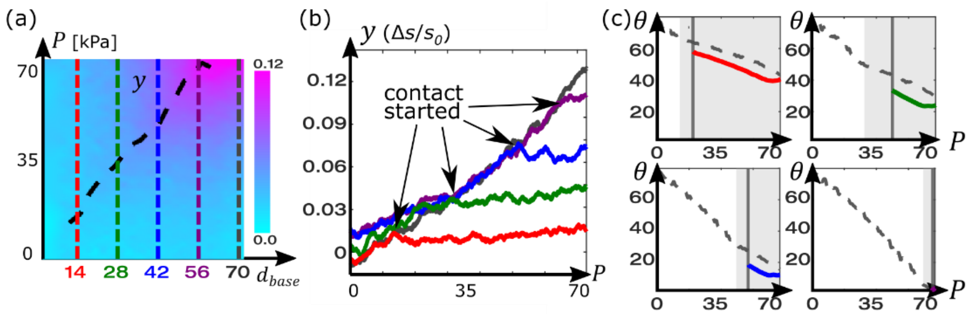

Figure 5.8. Estimation of the state variables: a) Sensor signal plot at the selected sensor location (ϵ_1 in **Figure 5.7a**). The signal is similar to the predicted result in **Figure 5.7b**. b) Sensor signals at several finger base positions (d_{base}). The drak grey curve of free motion (d_{base} = 70 mm) can be a reference signal for detecting a contact. c) Estimation results. There are delay and errors with underestimation in detecting a contact and estimating θ, which is due to the positive threshold used in the detection method.

Following the result in Section 4.2, a soft strain sensor was embedded at the location of ϵ_1 in **Figure 5.7a**. **Figure 5.8a** is the colormap plot of the embedded sensor signal, which looks similar to ϵ_1 plot in **Figure 5.7d**. For five different d_{base} values, the sensor signals (y) are plotted again in **Figure 5.8b**. If the distance is large enough (d_{base} = 70 mm), no contact occurs even though the pressure is increased to the maximum value, as shown with the dark gray curve in **Figure 5.8b**. As the distance (d_{base}) decreases, the fingertip starts to make a contact at certain pressure levels, and the contact pressure level decreases as d_{base} decreases. From these contact starting points, the sensor signal starts to deviate from the dark gray curve.

We now set the dark gray curve as a reference signal and let the internal pressure of the actuator increase when the base position (d_{base}) is given. If the deviation is larger than a certain threshold, we can say that a contact is occurring. Plugging the pressure value at this point into the regression model of the dotted contact boundary in **Figure 5.7**, we can estimate the distance ($\hat{d}_{base}$). Now having the $\hat{d}_{base}$ value, we can calculate the estimated $\hat{\theta}$ from the colormap in **Figure 5.7c**.

With this strategy, we estimated the value of θ on-line for the four distances in **Figure 5.8a** except for the reference (d_{base} = 70 mm) curve. During estimation, only the sensor signal, the reference signal (dark gray curve), and the regression models (the θ map and the dotted boundary in **Figure 5.7c**) were used, and no vision data was referred. **Figure 5.8c** show the result. The dotted gray line is the reference value, which was calculated from the vision data after the experiment. The shaded region represents the reference contact region. The vertical lines indicate the input pressures, where the contacts start to occur, detected on-line (i.e. the points where the sensor signal starts to deviate from the reference more than the threshold). Estimation of the θ starts after this point.

Although estimation was reliable, there was a delay in detecting the contact. In other words, the vertical line appears at a slightly higher pressure than the left boundary of the shaded region in **Figure 5.8c**. This is because we set the threshold for the deviation larger than 0. Although the delay can be reduced by lowering the threshold, a certain level of a positive threshold is necessary relative to the noise level of the sensor. The error of the estimated θ can be described in the same context. If there is a delay in contact detection, it means that the pressure where the contact is detected is larger than the actual starting level. In the same way, we find the $\hat{d}_{base}$ value larger than the true value from the contact boundary of **Figure 5.7c**. Referring to the θ map in **Figure 5.7c**, large pressure and $\hat{d}_{base}$ makes the final estimation of the θ smaller than the true value. Those errors can be compensated by tuning the gain or the offset when making a feedback input with $\hat{\theta}$. The algorithm and the result of closed-loop control using $\hat{\theta}$ are discussed in the next section.

5.5. Control

5.5.1. Control strategy

The pseudo code in Algorithm 1 shows the implementation of the state evolution, transitions, task completion, feedback input and the control strategy described from Sections 3 and 4.

Algorithm 1. Control algorithm

get reference sensor signal of free motion $y(P)$

move the wall to the initial position

Initialstate is (non-contact/pressurize/stay)

$u_1 \leftarrow 1,\ u_2 \leftarrow 0$

while not SUCCEED

 update internal time $\tau \leftarrow \tau + d\tau$

 update pressure $P \leftarrow P + u_1 P$

 update wall position $d_{base} \leftarrow d_{base} + u_2 d_{base}$

 read sensor signal y

 if state is (non-contact/pressurize/stay)

  if $P \geq P_{max}$

   update $u_1 \leftarrow -4,\ u_2 \leftarrow -1,\ T_{move} \leftarrow 10$

   go to state (non-contact/depressurize/approach)

  if $|y(P) - ref(P)| > threshold$

   calculate $\hat{d}_{base} = \hat{d}_{base}(P)$

   go to state (contact/pressurize/stay)

 else if state is (contact/pressurize/stay)

  calculate $\hat{\theta}(P, \hat{d}_{base})$

  if $\tau \geq T_{grip}$

   SUCCEED

  if $P \geq P_{max}$

   update $u_1 \leftarrow -4,\ u_2 \leftarrow -1,\ T_{move} \leftarrow K_1 \hat{d}_{base}$

go to state (non-contact/depressurize/approach)

if $\hat{\theta} \geq \theta_{max}$

update $u_1 \leftarrow -4,\ u_2 \leftarrow 1,\ T_{move} \leftarrow K_2\hat{\theta}$

go to state(non-contact/depressurize/retreat)

else if state is (non-contact/depressurize/approach)

if $\tau \geq T_{move}$

update $u_1 \leftarrow 1,\ u_2 \leftarrow 0$

go to (non-contact/pressurize/stay)

else if state is (non-contact/depressurize/retreat)

if $\tau \geq T_{move}$

update $u_1 \leftarrow 1,\ u_2 \leftarrow 0$

go to (non-contact/pressurize/stay)

5.5.2. Results

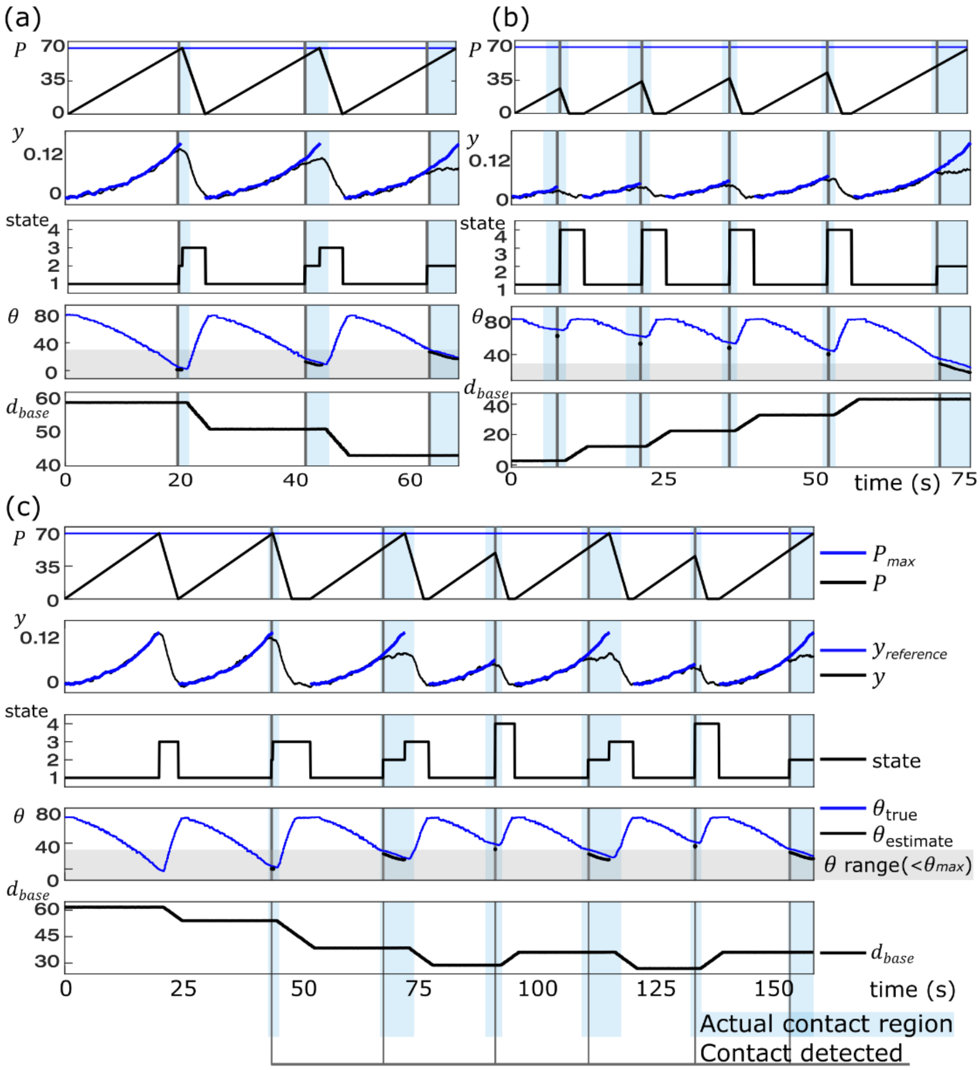

Figure 5.9. Control results: (a,b) θ_{max}= 36°, feedback input T_{move} = 4, and c) θ_{max} = 30°, feedback input $T_{move} = 4 + 0.05(\theta_{desired} - \hat{\theta})$. At the ends of all three cases, the gripper successfully completed the gripping task.

Using the above algorithm, we conducted control experiments for three different initial conditions and feedback inputs (**Figure 5.9**). In each subfigure, the first two subplots show the input pressure (P) and the sensor signal (y) with the reference signal (blueline) of the non-contact free motion. When the sensor signal starts to deviate from the reference signal (vertical line), the pressure at the moment is stored and $\hat{d}_{base}$ is calculated from the regression model (dotted line of **Figure 5.7c**). In the third subplot, the four discrete states in **Equation 5.4** (and **Figure 5.5**) are shown with four integer values from 1 to 4 in order. While maintaining the contact in the state (*contact/pressurizing/staying*), θ is estimated. The estimated value $\hat{\theta}$ determines whether to jump out of the current state or not and the feedback input for the next state. The blue shaded region is the true contact region. The gray region of the θ plot shows the allowable θ range as defined in the task. The blue line in the same plot shows the true θ value. As predicted from **Figure 5.8**, the detection has the delay and the estimated $\hat{\theta}$ has negative errors. In the case of **Figures 5.9a** and **5.9b**, the input T_{move} was set as a constant value, which determines the distance to move to the wall. In other words, the $\hat{\theta}$ value only affected the discrete inputs of u_1 and u_2 that determine the "direction" of the input but not the continuous input for the "magnitude". The finger moved with a small incremental step for each transition.

Figure 5.9a shows the case of a "too far" initial condition (Supporting Video 1). While increasing the pressure in the state 1 (*non-contact/pressurize/stay*), the finger made a contact. After detecting the contact, the state transition was made to the state 2, (*contact/pressurize/stay*). In the state 2, before the clock reaches T_{grip} (= 5 seconds) the pressure was saturated and the controller jumped to the state 3 (*non-contact/depressurize/approach*) for reducing the distance. After repeating the process once again, d_{base} was adjusted to the proper value and completed the task.

Figure 5.9b is the case of a "too close" initial condition (Supporting Video 2). The contact occurred while the pressure was increased (from the state 1 to the state 2). Just after the transition occurred, however, the $\hat{\theta}$ turned out to be larger than the $\theta_{max}(= 36°)$ so the state immediately moved to the state 4 (*non-contact/depressurize/retreat*). This adjustment process was repeated four times before the task was completed.

In the above two cases the $\hat{\theta}$ was not reflected to the magnitude of the feedback input. The magnitude was preset to a small incremental value so that the trajectory of d_{base}, the "solution" of the system, can "converge" to the desired value. However, this strategy does not guarantee the convergence of the solution in general if the target range is small. Also, if the target is too far away from the finger in the initial condition, the convergence is very slow.

In **Figure 5.9c**, the target condition was harsher, i.e. the $\theta_{max} = 30°$ (Supporting Video 3). The control input, T_{move}, was determined by the difference of the target value of θ from the estimated value multiplied and added by a gain and an offset, respectively. The trajectory of the solution d_{base} was converged into the allowable position after oscillation between the state 3 and the state 4.

5.6. Discussion

The entire process of system description, analysis and control of the soft pneumatic gripping system described in this work was fundamentally aimed to find the optimal position and orientation of the fingertip to successfully grip an unknown object by evaluating the relative angle at the contact point. More specifically, our approach tries to place the contact force at the fingertip inside the friction cone of the object surface [170,193,194]. To deliver this key concept, we assumed a simple system of a cubic object and one-dimensional interaction (**Figure 5.3**). In this simplified system, the surface normal of the object is always fixed and the fingertip force lies on the one-dimensional trajectory (red line of **Figure 5.1b**). To place the fingertip force inside the fixed friction cone, control of the finger base position (d_{base}) while evaluating the angle between the fixed surface normal and the force was suggested as a strategy. The angle can be estimated by sensing the local strain of the finger while contact occurs.

However, if we generalize our approach for more complex applications, the surface normal of the object is not fixed anymore and rather unknown, which means we have more states to estimate and control. To address this, we need to add more sensors, such as fingertip force sensors [192,195] in addition to strain sensors, or increase the control dimension with additional DoFs of the gripper base. In addition, the current model of a single-finger system should be extended to a multi-fingered gripper to accommodate the arbitrary shape of the object [165,166,167]. In this case, the structural compliance of the soft gripper will be a great benefit in preventing the system from being bulky with too many DoFs or fingers, since the gripper can easily adapt its shape to and conform the object.

Furthermore, it is always possible for the object to slip during the gripping process, caused by different reasons, such as the weight or the surface curvature of the object, in practical applications. This will introduce uncertainties to the suggested model, and it will be impossible to include all the possibilities in the model. However, monitoring the history of the sensor signals or the motion of the robot may provide useful information to address this issue, which is often used in hysteresis analysis [196,197,198], and it will be one of the areas of future work.

Chapter 6

Conclusion

Beyond the monotonous operation of rigid robots in standardized environments, which was the main focus of the traditional robot industry, the adaptive interaction between humans, robots, and environments that are unstructured or unknown has endless possibilities for use in the field of robotics. With the aim of making the robots friendly to humans and adaptive to the surrounding environments by improving the close human-robot-environment interaction, this thesis discussed the development from elemental technology to integrated systems, based on soft materials.

The thesis presented the practical issues that arise from the realization of the grand challenge. First of all, accurate perception of the systems is essential for the close connection between the human, robot, and environment. To solve this problem with enhanced sensor technology, in Chapter 2, the multi-material sensor structure was proposed for improving the sensitivity of the soft strain sensors. This structure produced a sensor resolution more than three times that of the conventional structure. This allowed the sensor to detect the tremor of a human finger, with less than 1 mm-fingertip displacement. The working principle of sensitivity enhancement, definition of the design parameters, modeling, and experimental validation were discussed in the chapter.

The remaining chapters respectively tried to build a tight and robust connection between the human, robot, and environment. Chapter 3 focused on the sensing of human hands. Hands are the body parts that most actively and elaborately interact with the environment but have such a complex structure and function, and therefore complete sensing technology for them does not yet exist. In other words, achieving both the accuracy of sensing and the simplicity of the structure, which are the essential conditions for ensuring high performance while interacting with the robot or the environment, are the technical problems that have not yet been solved. In the chapter, a soft wearable glove based on the multi-material structure and the collection of highly accurate ground truth data through motion capture was suggested as a solution. The proposed system showed exceptionally higher quantitative and qualitative accuracy compared to previously developed systems and also demonstrated its practical use for various virtual applications.

Chapter 4 aimed to connect humans and soft robots in a closed loop. In other words, once the human movements and intentions are captured and delivered to the robot, the robot must respond accordingly, and the information about this response must be transmitted back to the human. To implement this framework, the robot's self-sensing functionality for accurate control of its motion and a haptic interface to transmit the information to the human are required. In the chapter, for a soft actuator in the spotlight for its compact structure and small driving power, self-sensing and teleoperation were implemented by embedding the soft sensor to measure its deformation. Also, by developing a haptic device based on the actuator which takes advantage of the compact form factor of it, accurate teleoperation of the soft gripper and transfer of the information to the operator were completed. The feasibility of an accurate human-soft robot interaction system was demonstrated by applying the proposed system to a practical pick-and-place scenario.

Chapter 5 tried to connect the robots and the environment to complete the final link of human-robot-environment interaction, and to accomplish the major goal of the entire thesis. Despite the compliant characteristic of the soft robot ensuring safety, the resulting high complexity has limited the interaction between the robot and the surrounding environment to be passive and inaccurate. In the chapter, a framework to detect complex changes in soft robotic systems due to the environment was proposed, based on the hybrid analysis which can describe the systems with some discrete variables. In the framework, the robot was able to autonomously perceive and adapt to the surrounding environment by self-sensing its own states. As an example, the problem of grasping an unknown object was defined. By adopting the framework, the soft gripper was able to infer the size of the target object using the embedded sensor, autonomously adjust its position based on the inference, and finally complete the grasping task.

I hope this thesis serves as a small step toward realizing borderless interaction between humans, robots, and environments, and further toward the convenience and safety of humanity.

Bibliography

1. T. B. Sheridan, "Human–robot interaction: status and challenges," Human factors, 58(4), 525-532, 2016.
2. P. A. Lasota, T. Fong, and J. A. Shah. "A survey of methods for safe human-robot interaction," Foundations and Trends® in Robotics, 5(4), 261-349, 2017.
3. M. Vukobratovic, "Robot-environment dynamic interaction survey and future trends," Journal of Computer and Systems Sciences International, 49, 329-342, 2010.
4. L. Han, W. Xu, P. Kang, and H. Yuan, "Unified Neural Adaptive Control for Multiple Human–Robot–Environment Interactions," IEEE Transactions on Industrial Informatics, 17(2), 1166-1175, 2020.
5. P. Chotiprayanakul, "Effective methods for human-robot-environment interaction by means of haptic robotics", Doctoral dissertation, 2012.
6. S. Xiao, C. Wang, Y. Shi, J. Yu, L. Xiong, C. Peng, and L. Yang, "Visual optimization of ultrasound-guided robot-assisted procedures using variable impedance control," 2021 WRC Symposium on Advanced Robotics and Automation (WRC SARA), pp. 128-133, 2021.
7. S. D. Sierra, M. F. Jiménez, M. C. Múnera, A. Frizera-Neto, and C. A. Cifuentes, "Remote-operated multimodal Interface for therapists during Walker-assisted gait rehabilitation: A preliminary assessment," 2019 14th ACM/IEEE International Conference on Human-Robot Interaction (HRI) pp. 528-529, 2019.
8. M. F. Jimenez, R. C. Mello, T. Bastos, T., and A. Frizera, "Assistive locomotion device with haptic feedback for guiding visually impaired people," Medical Engineering & Physics, 80, 18-25, 2020.
9. Y. Jiang, S. Yin, J. Dong, and O. Kaynak, "A review on soft sensors for monitoring, control, and optimization of industrial processes," IEEE Sensors Journal, 21(11), 12868-12881, 2020.
10. M. Amjadi, K.U. Kyung, I. Park, and M. Sitti, "Stretchable, skin-mountable, and wearable strain sensors and their potential applications: A review," Advanced Functional Materials, 26 (11), 1678–1698, 2016.
11. G. Beattie and H. Shovelton, "An exploration of the other side of semantic communication: How the spontaneous movements of the human hand add crucial meaning to narrative", Semiotica, 184-1/4, 33-51, 2011.
12. L. Gupta and S. Ma, "Gesture-based interaction and communication: automated classification of hand gesture contours," IEEE Transactions on Systems, Man, and Cybernetics, Part C (Applications and Reviews), 31(1), 114-120, 2001.
13. C. Lugaresi, J. Tang, H. Nash, C. McClanahan, E. Uboweja, M. Hays, and M. Grundmann, "Mediapipe: A framework for building perception pipelines," arXiv preprint arXiv:1906.08172, 2019.
14. F. Weichert, D. Bachmann, B. Rudak, and D. Fisseler, "Analysis of the accuracy and robustness of the leap motion controller," Sensors, 13(5), 6380-6393, 2013.
15. https://www.manus-meta.com/ (accessed: Jan 20th, 2024).

16. https://stretchsense.com/ (accessed: Jan 20th, 2024).
17. M. Pan, Y. Tang, Y., and H. Li, "State-of-the-art in data gloves: A review of hardware, algorithms, and applications," IEEE Transactions on Instrumentation and Measurement, 2023.
18. Y. -L. Park, B.R. Chen, and R.J. Wood, "Design and fabrication of soft artificial skin using embedded microchannels and liquid conductors," IEEE Sens. J. 12 (8), 2711–2718, 2012.
19. M. G. Kim, H. Alrowais, S. Pavlidis, and O. Brand, "Size-scalable and high-density liquid-metal-based soft electronic passive components and circuits using soft lithography," Adv. Funct. Mater. 27 (3), 1604466, 2017.
20. D. Y. Choi, M. H. Kim, Y. S. Oh, S. H. Jung, J. H. Jung, H. J. Sung, H. W. Lee, and H. M. Lee, "Highly stretchable, hysteresis-free ionic liquid-based strain sensor for precise human motion monitoring," ACS Appl. Mater. Interfaces 9 (2), 1770–1780, 2017.
21. M. G. Kim, H. Alrowais, O. Brand, "3D-integrated and multifunctional all soft physical microsystems based on liquid metal for electronic skin applications," Adv. Electron. Mater. 4 (2), 1700434, 2018.
22. Y. Mengüç, Y. -L. Park, H. Pei, D. Vogt, P. M. Aubin, E. Winchell, L. Fluke, L. Stirling, R. J. Wood, and C. J. Walsh, "Wearable soft sensing suit for human gait measurement," Int. J. Robot. Res. 33 (14), 1748–1764, 2014.
23. Y. Yoon, S. Kim, D. Kim, S.K. Kauh, and J. Lee, "Four degrees-of-freedom direct writing of liquid metal patterns on uneven surfaces," Adv. Mater. Technol. 4 (2), 1800379, 2019.
24. S. Kim, J. Oh, D. Jeong, and J. Bae, "Direct wiring of eutectic gallium–indium to a metal electrode for soft sensor systems," ACS Appl. Mater. Interfaces 11 (22), 20557–20565, 2019.
25. H. Wang, M. Totaro, L. Beccai, "Toward perceptive soft robots: Progress and challenges," Adv. Sci. 5 (9), 1800541, 2018.
26. J. Morrow, H. S. Shin, C. Phillips-Grafflin, S. H. Jang, J. Torrey, R. Larkins, S. Dang, Y. -L. Park, and D. Berenson, "Improving soft pneumatic actuator fingers through integration of soft sensors, position and force control, and rigid fingernails," in 2016 IEEE International Conference on Robotics and Automation (ICRA), IEEE, pp. 5024–5031, 2016.
27. V. Wall, G. Zöller, and O. Brock, "A method for sensorizing soft actuators and its application to the rbo hand 2," in 2017 IEEE International Conference on Robotics and Automation (ICRA), IEEE, pp. 4965–4970, 2017.
28. L. Y. Zhou, Q. Gao, J. F. Zhan, C. Q. Xie, J. Z. Fu, Y. He, "Three-dimensional printed wearable sensors with liquid metals for detecting the pose of snakelike soft robots," ACS Appl. Mater. Interfaces 10 (27), 23208–23217, 2018.
29. T. T. Hoang, P. T. Phan, M. T. Thai, N. H. Lovell, and T. N. Do, "Bio-inspired conformable and helical soft fabric gripper with variable stiffness and touch sensing," Adv. Mater. Technol. 5 (12), 2000724, 2020.
30. H. J. Kim, C. Son, B. Ziaie, "A multiaxial stretchable interconnect using liquid alloy-filled elastomeric microchannels," Appl. Phys. Lett. 92 (1), 011904, 2008.

31. Y. -L. Park, C. Majidi, R. Kramer, P. Bérard, R. J. Wood, “Hyperelastic pressure sensing with a liquid-embedded elastomer,” J. Micromech. Microeng. 20 (12),125029, 2010.
32. T. V. Neumann, M. D. Dickey, “Liquid metal direct write and 3D printing: A review,” Adv. Mater. Technol. 5 (9), 2000070, 2020.
33. G. Shin, B. Jeon, Y. -L. Park, “Direct printing of sub-30 μm liquid metal patterns on three-dimensional surfaces for stretchable electronics,” J. Micromech. Microeng. 30 (3), 034001, 2020.
34. L. Mullins, “Softening of rubber by deformation,” Rubber Chem. Technol. 42 (1), 339–362, 1969.
35. J. Diani, B. Fayolle, P. Gilormini, “A review on the mullins effect,” Eur. Polym. J. 45 (3), 601–612, 2009.
36. P. L. S. Martins, R. M. Natal Jorge, A. J. M. Ferreira, “A comparative study of several material models for prediction of hyperelastic properties: Application to silicone-rubber and soft tissues,” Strain 42 (3), 135–147, 2006.
37. M. Shahzad, A. Kamran, M. Z. Siddiqui, M. Farhan, “Mechanical characterization and FE modelling of a hyperelastic material,” Mater. Res. 18, 918–924, 2015.
38. S. Din, W. Xu, L. K. Cheng, S. Dirven, “A stretchable multimodal sensor for soft robotic applications,” IEEE Sens. J. 17 (17), 5678–5686, 2017.
39. M. Tatari, A. Mohammadi Nasab, K.T. Turner, W. Shan, “Dynamically tunable dry adhesion via subsurface stiffness modulation,” Adv. Mater. Interfaces 5 (18), 1800321, 2018.
40. A. Luo, A. M. Nasab, M. Tatari, S. Chen, W. Shan, K. T. Turner, “Adhesion of flat-ended pillars with non-circular contacts,” Soft Matter 16 (41), 9534–9542, 2020.
41. R. Brighenti, A. Spagnoli, A. Carpinteri, F. Artoni, “Notch effect in highly deformable material sheets,” Thin-Walled Struct. 105, 90–100, 2016.
42. N. W. Bartlett, M. T. Tolley, J. T. B. Overvelde, J. C. Weaver, B. Mosadegh, K. Bertoldi, G. M. Whitesides, R. J. Wood, “A 3D-printed, functionally graded soft robot powered by combustion,” Science 349 (6244), 161–165, 2015.
43. A. Atalay, V. Sanchez, O. Atalay, D. M. Vogt, F. Haufe, R. J. Wood, and C. J. Walsh, “Batch fabrication of customizable silicone-textile composite capacitive strain sensors for human motion tracking,” Advanced Materials Technologies, 2(9), 1700136, 2017.
44. Y. Park and J. Bae, “A three-dimensional finger motion measurement system of a thumb and an index finger without a calibration process,” Sensors, 20(3), 756, 2020.
45. H. O. Michaud, L. Dejace, S. De Mulatier, and S. P. Lacour, “Design and functional evaluation of an epidermal strain sensing system for hand tracking,” in 2016 IEEE/RSJ International Conference on Intelligent Robots and Systems (IROS) pp. 3186-3191, IEEE, 2016.
46. F. L. Hammond, Y. Mengüç, and R. J. Wood, “Toward a modular soft sensor-embedded glove for human hand motion and tactile pressure measurement,” in 2014 IEEE/RSJ International Conference on Intelligent Robots and Systems, pp. 4000-4007, IEEE, 2014.
47. F. Lorussi, E. P. Scilingo, M. Tesconi, A. Tognetti, and D. De Rossi, “Strain sensing fabric for hand posture and gesture monitoring,” IEEE transactions on information

technology in biomedicine, 9(3), 372-381, 2005.

48. T. F. O'Connor, M. E. Fach, R. Miller, S. E. Root, P. P. Mercier, and D. J. Lipomi, "The Language of Glove: Wireless gesture decoder with low-power and stretchable hybrid electronics," PloS one, 12(7), e0179766, 2017.
49. M. M. Sturman, D. E. Vaillancourt, D. M. Corcos, "Effects of aging on the regularity of physiological tremor," J. Neurophysiol. 93 (6), 3064–3074, 2005.
50. H. Ryu, S. Park, J. J. Park, and J. Bae, "A knitted glove sensing system with compression strain for finger movements," Smart Materials and Structures, 27(5), 055016, 2018.
51. M. R. Cutkosky, "On grasp choice, grasp models, and the design of hands for manufacturing tasks," *IEEE Transactions on Robotics and Automation* **5**, 269-279, 1989.
52. F. Gonzalez, F. Gosselin, and W. Bachta, "Analysis of hand contact areas and interaction capabilities during manipulation and exploration," *IEEE Transactions on Haptics* **7**, 415-429, 2014.
53. P. M. Ferreira, J. S. Cardoso, and A. Rebelo, "On the role of multimodal learning in the recognition of sign language," *Multimedia Tools and Applications* **78**, 10035-10056, 2019.
54. R. Li, W. Hongyu and L. Zhenyu, "Survey on mapping human hand motion to robotic hands for teleoperation," *IEEE Transactions on Circuits and Systems for Video Technology* **32**, 2647-2665, 2021.
55. J. S. Kim, B. K. Kim, M. Jang, K. Kang, D. E. Kim, B. K. Ju, J. Kim, "Wearable hand module and real-time tracking algorithms for measuring finger joint angles of different hand sizes with high accuracy using FBG strain sensor," *Sensors* **20**, 1921, 2020.
56. S. Kim, J. Oh, D. Jeong, W. Park, J. Bae, "Consistent and reproducible direct ink writing of eutectic gallium–indium for high-quality soft sensors," *Soft Robotics* **5**, 601-612, 2018.
57. A. Erol, G. Bebis, M. Nicolescu, R. D. Boyle, X. Twombly, "Vision-based hand pose estimation: A review," *Computer Vision and Image Understanding* **108**, 52-73, 2007.
58. G. Shin, S. Lee, and Y. -L. Park, "Selective patterning of conductive elastomers embedded with silver powders and carbon nanotubes for stretchable electronics," *IEEE Robotics and Automation Letters* **7**, 4983-4990, 2022.
59. Y. Park, J. Jung, Y. Lee, D. Lee, J. J. Vlassak, Y. -L. Park, "Liquid-metal micro-networks with strain-induced conductivity for soft electronics and robotic skin," *npj Flexible Electronics* **6**, 81, 2022.
60. Y. Kim, P. C. W. Kim, R. Selle, A. Shademan, A. Krieger, "Experimental evaluation of contact-less hand tracking systems for tele-operation of surgical tasks," in 2014 IEEE International Conference on Robotics and Automation (ICRA), 3502-3509, IEEE, 2014.
61. C. Mizera, T. Delrieu, V. Weistroffer, C. Andriot, A. Decatoire, J. P. Gazeau, "Evaluation of hand-tracking systems in teleoperation and virtual dexterous manipulation," *IEEE Sensors Journal* **20**, 1642-1655, 2019.
62. J. Connolly, J. Condell, B. O'Flynn, J. T. Sanchez, P. Gardiner, "IMU sensor-based electronic goniometric glove for clinical finger movement analysis," *IEEE Sensors Journal* **18**, 1273-1281, 2017.

63. N. Miyata, M. Kouchi, T. Kurihara, M. Mochimaru, “Modeling of human hand link structure from optical motion capture data,” in 2004 IEEE/RSJ International Conference on Intelligent Robots and Systems (IROS), **3**. IEEE, 2004.
64. J. -B. Chossat, Y. Tao, V. Duchaine, Y. -L. Park, “Wearable soft artificial skin for hand motion detection with embedded microfluidic strain sensing,” in 2015 IEEE International Conference on Robotics and Automation (ICRA), 2568-2573, IEEE, 2015.
65. I. Sarakoglou, A. Brygo, D. Maxxanti, N. G. Hernandez, D. G. Caldwell, N. G. Tsagarakis, “Hexotrac: A highly under-actuated hand exoskeleton for finger tracking and force feedback,” in 2016 IEEE/RSJ International Conference on Intelligent Robots and Systems (IROS), 1033-1040, IEEE, 2016.
66. C. K. Mummadi F. P. P. Leo, K. D. Verma, S. Kasireddy, P. M. Scholl, J. Kempfle, and K. V. Laerhoven, “Real-time and embedded detection of hand gestures with an IMU-based glove,” *Informatics* **5**, 28, 2018.
67. D. Kim, J. Kwon, S. Han, Y. -L. Park, S. Jo, “Deep full-body motion network for a soft wearable motion sensing suit,” *IEEE/ASME Transactions on Mechatronics* **24**, 56-66, 2018.
68. K. -Y. Chen, N. P. Shwetak and K. Sean, “Finexus: Tracking precise motions of multiple fingertips using magnetic sensing,” in *Proceedings of the 2016 CHI Conference on Human Factors in Computing Systems*, 1504-1514, 2016.
69. C. D. Metcalf, R. Robinson, A. J. Malpass, T. P. Bogle, T. A. Dell, C. Harris, S. H. Demain, “Markerless motion capture and measurement of hand kinematics: validation and application to home-based upper limb rehabilitation,” *IEEE Transactions on Biomedical Engineering* **60***,* 2184-2192, 2013.
70. T. Schubert, K. Eggensperger, A. Gkogkidis, F. Hutter, T. Ball, W. Burgard, “Automatic bone parameter estimation for skeleton tracking in optical motion capture,” in 2016 IEEE International Conference on Robotics and Automation (ICRA), 5548-5554 IEEE, 2016.
71. S. Yuan, Q. Ye, B. Stenger, S. Jain, T. K. Kim, “Bighand2. 2m benchmark: Hand pose dataset and state of the art analysis”, *Proceedings of the IEEE Conference on Computer Vision and Pattern Recognition*, 2017.
72. I. Rhiu and W. Kim. “Estimation of stature from finger and phalange lengths in a Korean adolescent”, *Journal of Physiological Anthropology* **38**, 13 2019.
73. T. Pham, P. N. Pathirana, H. Trinh, P. Fay, “A non-contact measurement system for the range of motion of the hand,” *Sensors* **15**, 18315-18333, 2015.
74. D. DeMers and K. Kreutz-Delgado, “Inverse kinematics of dexterous manipulators,” *Neural Systems for Robotics.* Academic Press. 75-116, 1997.
75. A. -A. Samadani, D. Kulic, R. Gorbet. “Multi-constrained inverse kinematics for the human hand,” in 2012 Annual International Conference of the IEEE Engineering in Medicine and Biology Society (EMBC), 6780-6784, IEEE, 2012.
76. A. Aristidou, “Hand tracking with physiological constraints,”. *The Visual Computer* **34**, 213-228, 2018.
77. Y. Lee, W. Do, H. Yoon, J. Heo, W. H. Lee, D. Lee, “Visual-inertial hand motion tracking with robustness against occlusion, interference, and contact,” *Science Robotics* **6**, eabe1315, 2021.
78. C. R. Mason, J. E. Gomez, T. J. Ebner, “Hand synergies during reach-to-grasp,”. Journal

of neurophysiology, 86(6), 2896-2910, 2001.
79. M. Santello, M. Flanders, J. F. Soechting, "Postural hand synergies for tool use," Journal of neuroscience, 18(23), 10105-10115, 1998.
80. J. Lin, Y. Wu, T. S. Huang, "Modeling the constraints of human hand motion," in Proceedings workshop on human motion, 121-126. IEEE, 2000.
81. G. D. Kessler, L. F. Hodges, N. Walker, "Evaluation of the CyberGlove as a whole-hand input device," ACM Transactions on Computer-Human Interaction (TOCHI), 2(4), 263-283, 1995.
82. M. Wang, "Non-Invasive Vision-Based Measurement of Hand Kinematics and Interaction," Doctoral dissertation, Massachusetts Institute of Technology, 2023.
83. P. Cerveri, E. De Momi, N. Lopomo, G. Baud-Bovy, R. M. L. Barros, and G. Ferrigno, "Finger kinematic modeling and real-time hand motion estimation," Annals of biomedical engineering, 35, 1989-2002, 2007.
84. C. Buizza, Y. Demiris, "Rotational Adjoint Methods for Learning-Free 3D Human Pose Estimation from IMU Data", in 2020 25th International Conference on Pattern Recognition (ICPR), 7868-7875. IEEE, 2021.
85. Y. Feng, M. Zhong, and F. Dong, "Research on Monocular-Vision-Based Finger-Joint-Angle-Measurement System," *Sensors* **22**, 7276, 2022.
86. A. Wetzler, R. Slossberg, and R. Kimmel, "Rule of thumb: Deep derotation for improved fingertip detection,". *arXiv preprint* arXiv:1507.05726, 2015.
87. L. Hoyet, K. Ryall, R. McDonnell, C. O'Sullivan, "Sleight of hand: perception of finger motion from reduced marker sets," *Proceedings of the ACM SIGGRAPH Symposium on Interactive 3D Graphics and Games*, 79-86, 2012.
88. J. S. Supancic, G. Rogez, Y. Yang, J. Shotton, D. Ramanan, "Depth-based hand pose estimation: data, methods, and challenges," *Proceedings of the IEEE International Conference on Computer Vision*, 1868-1876, 2015.
89. B. -S. Lin, I. J. Lee, S. Y. Yang, Y. C. Jo, J. Lee, J. L. Chen, "Design of an inertial-sensor-based data glove for hand function evaluation," *Sensors* **18**, 1545, 2018.
90. https://www.senseglove.com/ (accessed: Jan 20th, 2024).
91. X. Gu, Y. Zhang, W. Sun, Y. Bian, D. Zhou, P. O. Kristensson, "Dexmo: An inexpensive and lightweight mechanical exoskeleton for motion capture and force feedback in VR," *Proceedings of the 2016 CHI Conference on Human Factors in Computing Systems*, 2016.
92. M. D. Dickey, R. C. Chiechi, R. J. Larsen, E. A. Weiss, D. A. Weitz, G. M. Whitesides, "Eutectic gallium-indium (EGaIn): a liquid metal alloy for the formation of stable structures in microchannels at room temperature," *Advanced Functional Materials* **18**, 1097-1104, 2008.
93. D. Kim, M. Kim, J. Kwon, Y. -L. Park, S. Jo, "Semi-supervised gait generation with two microfluidic soft sensors," *IEEE Robotics and Automation Letters* **4**, 2501-2507, 2019.
94. M. Amjadi, A. Pichitpajongkit, S. Lee, S. Ryu, and I. Park, "Highly stretchable and sensitive strain sensor based on silver nanowire–elastomer nanocomposite,". *ACS Nano* **8**, 5154-5163, 2014.

95. S. Kim, J. Oh, D. Jeong, J. Bae, "Direct wiring of eutectic gallium–indium to a metal electrode for soft sensor systems," *ACS Applied Materials & Interfaces* **11**, 20557-20565, 2019.
96. Y. -L. Park, B. -R Chen, and R. J. Wood, "Design and fabrication of soft artificial skin using embedded microchannels and liquid conductors," *IEEE Sensors journal* **12**, 2711-2718, 2012.
97. M. Park, T. Park, and Y. -L Park, "Parametric analysis of multi-material soft sensor structures for enhanced strain sensitivity," *Extreme Mechanics Letters* **60**, 101983, 2023.
98. L. Reissner, G. Fischer, R. List, P. Giovanoli, M. Calcagni, "Assessment of hand function during activities of daily living using motion tracking cameras: A systematic review," *Proceedings of the Institution of Mechanical Engineers, Part H: Journal of Engineering in Medicine* **233**, 764-783, 2019.
99. K. -S. Lee and M. -C. Jung, "Quantitative comparison of marker attachment methods for hand motion analysis," *International Journal of Occupational Safety and Ergonomics* **21**, 30-38, 2015.
100. K. -S. Lee and M. -C. Jung, "Ergonomic evaluation of biomechanical hand function," *Safety and health at work* **6**, 9-17, 2015.
101. J. M. Blackstone, "Children and gender-differences in exposure and how anthropometric differences can be incorporated into the design of computer input devices," *Scandinavian Journal of Work, Environment & Health*, 26-32, 2007.
102. K. Dandekar, I. B. Raju, and M. A. Srinivasan, "3-D finite-element models of human and monkey fingertips to investigate the mechanics of tactile sense," *J. Biomech. Eng.* **125**, 682-691, 2003.
103. P. Cerveri, E. D. Momi, N. Lopomo, G. Baud-Bovy, R. M. L. Barros, G. Ferrigno, "Finger kinematic modeling and real-time hand motion estimation," Annals of biomedical engineering **35**, 1989-2002, 2007.
104. I. M. Bullock, B. Júlia Borràs, and A. M. Dollar, "Assessing assumptions in kinematic hand models: a review," in 2012 4th IEEE RAS & EMBS International Conference on Biomedical Robotics and Biomechatronics (BioRob), 139-146, IEEE, 2012.
105. J. Lin, W. Ying, and T. S. Huang, "Modeling the constraints of human hand motion", *Proceedings Workshop on Human Motion*, 121-126, IEEE, 2000.
106. J. S. Dai, "Euler–Rodrigues formula variations, quaternion conjugation and intrinsic connections," *Mechanism and Machine Theory* **92**, 144-152, 2015.
107. J. C. Case, E. L. White, and R. K. Kramer, "Soft material characterization for robotic applications," *Soft Robotics* **2**, 80-87, 2015.
108. J. V. Stone, "Bayes' rule: a tutorial introduction to Bayesian analysis," Sebtel Press, 2013.
109. DW Kim, M. Park, and Y. -L Park, "Probabilistic modeling and Bayesian filtering for improved state estimation for soft robots," *IEEE Transactions on Robotics* **37**, 1728-1741, 2021.
110. N. Kantas, A. Doucet, S. S. Singh, J. Maciejowski, N. Chopin, "On particle methods for parameter estimation in state-space models," *Statistical Science* **30**, 328-351, 2015.
111. J. Durbin and S. J. Koopman, "Monte Carlo maximum likelihood estimation for non-Gaussian state space models," *Biometrika* **84**, 669-684, 1997.
112. E. J. Weiss and M. Flanders, "Muscular and postural synergies of the human hand," *Journal of Neurophysiology* **92**, 523-535, 2004.

113. M. Santello, M. Bianchi, M. Gabiccini, E. Ricciardi, G. Salvietti, D. Prattichizzo, M. Ernst, A. Moscatelli, H. Jorntell, A. M. L. Kappers, K. Kyriakopoulos, A. Albu-Schaffer, C. Castellini, A. Bicchi, "Hand synergies: Integration of robotics and neuroscience for understanding the control of biological and artificial hands," *Physics of Life Reviews* **17**, 1-23, 2016.
114. L. Noy, J. Friedman, and T. Flash, T. "Evaluating the reconstruction of virtual hand movements from real hand movements measured using a data-glove," 2011.
115. A. Tkach, A. Tagliasacchi, E. Remelli, M. Pauly, and A. Fitzgibbon, "Online generative model personalization for hand tracking,". ACM Transactions on Graphics (ToG), 36(6), 1-11, 2017.
116. T. Sharp, C. Keskin, D. Robertson, J. Taylor, J. Shotton, D. Kim, C. Rhemann, I. Leichter, A. Vinnikov, Y. Wei, D. Freedman, P. Kohli, E. Krupka, A. Fitzgibbon, and Izadi, S. "Accurate, robust, and flexible real-time hand tracking," in Proceedings of the 33rd annual ACM conference on human factors in computing systems pp. 3633-3642, 2015.
117. H. Ham, M. Park, T. Park, X. Gao, Y. -L. Park, and M. J. Park, "Teleoperation of Soft Robots with Real-Time Fingertip Haptic Feedback Using Small Batteries," Advanced Materials Technologies, 2300070, 2023.
118. M. Raessa, J. C. Y. Chen, W. W. Wan, K. Harada, "Human-in-the-loop manipulation planning for collaborative assembly," *IEEE Trans. Autom. Sci. Eng.*, **17**, 1800, 2020.
119. M. El-Atab, R. B. Mishra, F. Al-Modaf, L. Joharji, A. A. Alsharif, H. Alamoudi, M. Diaz, N. Qaiser, M. M. Hussain, "Soft actuators for soft robotic applications: A review," Advanced Intelligent Systems, 2(10), 2000128, 2020.
120. M. Li, A. Pal, A. Aghakhani, A. Pena-Francesch, and M. Sitti, "Soft actuators for real-world applications," Nature Reviews Materials, 7(3), 235-249, 2022.
121. W. Zhang, J. Hong, S. Ahmed, Z. Ounaies, and M. Frecker, "A two-stage optimization procedure for the design of an EAP-actuated soft gripper," in International Design Engineering Technical Conferences and Computers and Information in Engineering Conference, 59247, p. V05BT07A051, American Society of Mechanical Engineers, 2019.
122. C. Pagano and I. Fassi, "EAP as actuator for a gripper with variable curvature," in Electroactive Polymer Actuators and Devices (EAPAD), 6524, pp. 347-358, SPIE, 2007.
123. C. Briggs, T. Cheng, M. Meredith, P. N. Vicars, L. Rasmussen, A. Zhong, "Synthetic Muscle Electroactive Polymer (EAP) pressure sensing and controlled shape-morphing for robotic grippers," in Electroactive Polymer Actuators and Devices (EAPAD) XXIII 11587, pp. 110-118, SPIE, 2021.
124. L. Rasmussen, P. N. Vicars, C. Briggs, T. Cheng, E. A. Clancy, S. Carey, and B. Secino, "Synthetic Muscle electroactive polymer (EAP) shape-morphing and pressure sensing for robotic grippers," in Electroactive Polymer Actuators and Devices (EAPAD) XXII, 11375, pp. 7-14, SPIE, 2020.
125. R. Mutlu, G. Alici, W. Li, *IEEE Trans. Syst. Man, Cybern.: Syst.*, **47**, 2562, 2016.
126. J. Yin, R. Hinchet, H. Shea, C. Majidi, *Adv. Funct. Mater.*, **31**, 2007428, 2021.
127. Z. Liao, M. Hossain, X. Yao, X., "Ecoflex polymer of different Shore hardnesses: Experimental investigations and constitutive modelling," Mechanics of Materials, 144,

103366, 2020.
128. V. L. Tagarielli, R. Hildick-Smith, J. E. Huber, "Electro-mechanical properties and electrostriction response of a rubbery polymer for EAP applications," International Journal of Solids and Structures, 49(23-24), 3409-3415, 2012.
129. D. Kim, Y. Yoon, S. K. Kauh, J. Lee, *Adv. Funct. Mater.*, **28**, 1800380, 2018.
130. J. C. Case, E. L. White, R. K. Kramer, "Soft material characterization for robotic applications," *Soft Rob.*, **2**, 80, 2015.
131. L. Mullins, "Softening of rubber by deformation," *Rubber Chem. Technol.*, **42**, 339, 1969.
132. E. F. Camacho, C. B. Alba, "Model Predictive Control," *Springer Science & Business Media*, 2013.
133. Y. Zhang, H. Liu, T. Ma, L. Hao, Z. Li, "A comprehensive dynamic model for pneumatic artificial muscles considering different input frequencies and mechanical loads," *Mech. Syst. Sig. Process.*, **148**, 107133, 2021.
134. G. Bubak, A. Ansaldo, D. Gendron, L. Brayda, L. Ceseracciu, D. Ricci, "Parylene coated carbon nanotube actuators for tactile stimulation," in *Proc. SPIE* 2015, **9430**, 94300V, 2015.
135. C. Hatzfeld and T. A. Kern, "Engineering haptic devices," Springer London Limited, 2016.
136. D. Van Baelen, J. Ellerbroek, M. M. Van Paassen, D. A. Abbink, and M. Mulder, "Just feeling the force: Just noticeable difference for asymmetric vibrations," in 2020 IEEE International Conference on Human-Machine Systems (ICHMS), 1-6, IEEE, 2020.
137. G. Juravle, F. L. Colino, X. Meleqi, G. Binsted, and A. Farnè, "Vision facilitates tactile perception when grasping an object," Scientific Reports, 8(1), 15653, 2018.
138. H. Zhao, A. M. Hussain, A. Israr, D. M. Vogt, M. Duduta, D. R. Clarke, and R. J. Wood, "A wearable soft haptic communicator based on dielectric elastomer actuators,". Soft robotics, 7(4), 451-461, 2020.
139. Q. He, G. Yin, D. Vokoun, Q. Shen, J. Lu, X. Liu, X. Xu, M. Yu, and Z. Dai, "Review on improvement, modeling, and application of ionic polymer metal composite artificial muscle," Journal of Bionic Engineering, 19(2), 279-298, 2022.
140. B. Kim, D. H. Kim, J. Jung, and J. O. Park, "A biomimetic undulatory tadpole robot using ionic polymer–metal composite actuators," Smart materials and structures, 14(6), 1579, 2005.
141. S. J. Kim, I. T. Lee, H. Y. Lee, and Y. H. Kim, "Performance improvement of an ionic polymer–metal composite actuator by parylene thin film coating," Smart materials and structures, 15(6), 1540, 2006.
142. S. J. Kim, C. Cho, and Y. H. Kim, "Polymer packaging for arrayed ionic polymer–metal composites and its application to micro air vehicle control surface," Smart Materials and Structures, 18(11), 115009, 2009.
143. G. H. Feng, G. H. and S. Y. Hou, "Investigation of tactile bump array actuated with ionic polymer–metal composite cantilever beams for refreshable braille display application," Sensors and Actuators A: Physical, 275, 137-147, 2018.

144.H. Lei, W. Li, and X. Tan, “Encapsulation of ionic polymer-metal composite (IPMC) sensors with thick parylene: Fabrication process and characterization results,” Sensors and Actuators A: Physical, 217, 1-12, 2014.
145.F. Wang, X. Zhang, L. Ma, Z. Zhang, L. Han, C. Zeng, B. Shi, and D. Guo, “Facile and effective repair of Pt/Nafion IPMC actuator by dip-coating of PVP@ AgNPs,” Nanotechnology, 32(38), 385502, 2021.
146.Q. M. Wang and L. E. Cross, “Tip deflection and blocking force of soft PZT-based cantilever RAINBOW actuators,” Journal of the American Ceramic Society, 82(1), 103-110, 1999.
147.M. J. Lodeiro, M. Stewart, and M. G. Cain, “Displacement and blocking force measurements of piezoelectric macroactuators”, 2005.
148.M. Park, B. Jeong, and Y. -L. Park, “Hybrid system analysis and control of a soft robotic gripper with embedded proprioceptive sensing for enhanced gripping performance,” Advanced Intelligent Systems, 3(3), 2000061, 2021.
149.R. Mukherjee, D. Chen, “Control of free-flying underactuated space manipulators to equilibrium manifolds,” *IEEE Trans. Rob.*, **9**, 561, 1993.
150.K. C. Galloway, K. P. Becker, B. Phillips, J. Kirby, S. Licht, D. Tchernov, R. J. Wood, D. F. Gruber, “Soft robotic grippers for biological sampling on deep reefs,” *Soft Rob.*, **3**, 23, 2016.
151.N. Kumar, G. Krishnan, “Towards pneumatic spiral grippers: Modeling and design considerations,” *Soft Rob.*, **5**, 695, 2018.
152.M. R. Cutkosky, “Robotic Grasping and Fine Manipulation,” Springer Science & Business Media, 6, 2012.
153.M. R. Cutkosky, “On grasp choice, grasp models, and the design of hands for manufacturing tasks,” *IEEE Trans. Rob. Autom.*, **5**, 269, 2989.
154.A. Bicchi, “Hands for dexterous manipulation and robust grasping: A difficult road toward simplicity,” *IEEE Trans. Rob. Autom.*, **15**, 652, 2000.
155.S. Hirose, Y. Umetani, “The development of soft gripper for the versatile robot hand,” *Mech. Mach. Theory.*, **13**, 351, 1978.
156.R. Tomovic, G. Bekey, W. Karplus, “A strategy for grasp synthesis with multifingered robot hands,” in *Proc. 1987 Int. Conf. on Robotics and Automation (ICRA)*, 4, p. 83, 1987.
157.M. Rakić, “Multifingered robot hand with self-adaptability,” *Rob. Comput. Integr. Manuf.*, **5**, 269, 1989.
158.L. Birglen, T. Laliberte, C. M. Gosselin, “Underactuated Robotic Hands”, 40, Springer, , 2007.
159.S. Montambault, C. M. Gosselin, “Analysis of underactuated mechanical grippers,” J. Mech. Des., 123, 367, 2001.
160.D. M. Aukes, B. Heyneman, J. Ulmen, H. Stuart, M. R. Cutkosky, S. Kim, P. Garcia, A. Edsinger, “Design and testing of a selectively compliant underactuated hand,” Int. J. Robot. Res., 33, 721, 2014.
161.A. G. Zisimatos, M. V. Liarokapis, C. I. Mavrogiannis, K. J. Kyriakopoulos, “Open-

source, affordable, modular, light-weight, underactuated robot hands," in 2014 Proc. IEEE/RSJ Int. Conf. on Intelligent Robots and Systems (IROS), p. 3207, 2014.
162. H. Dong, E. Asadi, C. Qui, J. Dai, I. M. Chen, "Geometric design optimization of an under-actuated tendon-driven robotic gripper," Robot. Comput. Integr. Manuf., 50, 80, 2018.
163. M. Baril, T. Lalibertem, C. Gosselin, F. Routhier, "On the design of a mechanically programmable underactuated anthropomorphic prosthetic gripper," J. Mech. Des., 135, 121008, 2013.
164. N. Rojas, R. R. Ma, A. M. Dollar, "The GR2 gripper: An underactuated hand for open-loop in-hand planar manipulator," IEEE Trans. Rob., 32, 3, 2016.
165. J. Shintake, V. Cacucciolo, D. Floreano, H. Shea, "Soft robotic grippers," Adv. Mater., 30, 1707035, 2018.
166. Z. Wang, Y. Torigoe, S. Hirai, "A prestressed soft gripper: design, modeling, fabrication, and tests for food handling," IEEE Rob. Autom. Lett., 2, 1909, 2017.
167. R. Deimel, O. Brock, "A novel type of compliant and underactuated robotic hand for dexterous grasping," Int. J. Rob. Res., 35, 161, 2016.
168. M. Manti, T. Hassan, G. Passetti, N. D'Elia, C. Laschi, M. Cianchetti, "A bioinspired soft robotic gripper for adaptable and effective grasping," Soft Rob., 2, 107, 2015.
169. R. M. Murray, Z. Li, S. S. Sastry, A Mathematical Introduction to Robotic Manipulator, CRC Press, Boca Raton, FL 1994.
170. K. M. Lynch, F. C. Park, Modern Robotics: Mechanics, Planning, and Control, Cambridge University Press, New York, NY 2017.
171. A. D. Marchese, D. Rus, "Design, kinematics, and control of a soft spatial fluidic elastomer manipulator," Int. J. Rob. Res., 35, 840, 2016.
172. C. Duriez, "Control of elastic soft robots based on real-time finite element method," in Proc. 2013 IEEE Int. Conf. on Robotics and Automation (ICRA), p. 3982, 2013.
173. M. S. Branicky, Introduction to Hybrid Systems, Springer, Boston, MA 2005.
174. P. J. Antsaklis, J. A. Stiver, M. Lemmon, Hybrid System Modeling and Autonomous Control Systems, Springer, Berlin, Germany, 366–392, 1992.
175. X. Zhou, C. Majidi, O. M. O'Reilly, "Flexing into motion: A locomotion mechanism for soft robots," Int. J. Non Linear Mech., 74, 7, 2015.
176. X. Zhou, C. Majidi, O. M. O'Reilly, "Soft hands: An analysis of some gripping mechanisms in soft robot design," Int. J. Solids Struct., 64, 155, 2015.
177. T. Schlegl, M. Buss, "Hybrid closed-loop control of robotic hand regrasping," in Proc. 1998 IEEE Int. Conf. on Robotics and Automation (ICRA), 3206, 1998.
178. Y. Nakabo, T. Mukai, K. Asaka, "Kinematic modeling and visual sensing of multi-DOF robot manipulator with patterned artificial muscle," in Proc. 2005 IEEE Int. Conf. on Robotics and Automation (ICRA), 4315, 2005.
179. V. Ortenzi, N. Marturi, M. Mistry, J. Kuo, R. Stolkin, "Vision-based framework to estimate robot configuration and kinematic constraints," IEEE/ASME Trans. Mechatron., 23, 2402, 2018.
180. Z. Zhang, J. Dequidt, C. Duriez, "Vision-based sensing of external forces acting on soft

robots using finite element method," IEEE Robot. Autom. Lett., 3, 1529, 2018.
181. P. Renaud, E. Cervera, P. Martiner, "Towards a reliable vision-based mobile robot formation control", in Proc. 2004 IEEE/RSJ Int. Conf. on Intelligent Robots and Systems (IROS), 3176, 2004.
182. J. Wirekoh, L. Valle, N. Pol, Y.-L. Park, "Sensorized, flat, pneumatic artificial muscle embedded with biomimetic microfluidic sensors for proprioceptive feedback," Soft Rob., 6, 768, 2019.
183. J. Jung, M. Park, D. Kim, Y.-L. Park, "Optically sensorized elastomer air chamber for proprioceptive sensing of soft pneumatic actuators," IEEE Rob. Autom. Lett., 3, 2333, 2020.
184. I. M. Van Meerbeek, C. M. De Sa, R. F. Shepherd, "Soft optoelectronic sensory foams with proprioception," Science Robotics, 3, eaau2489, 2018.
185. B. S. Homberg, R. K. Katzschmann, M. R. Dogar, D. Rus, "Robust proprioceptive grasping with a soft robot hand," Auton. Robot., 43, 681, 2019.
186. E. N. Marieb, K. Hoehn, Human Anatomy & Physiology, 11th ed., Pearson, London, UK 2018.
187. G. Chalmers, "Strength training: Re-examination of the possible role of golgi tendon organ and muscle spindle reflexes in proprioceptive neuromuscular facilitation muscle stretching," Sports Biomech., 3, 159, 2004.
188. B. Mosadegh, P. Polygerinos, C. Keplinger, S. Wennstedt, R. F. Shepherd, U. Gupta, J. Shim, K. Bertoldi, C. J. Walsh, G. M. Whitesides, "Pneumatic networks for soft robotics that actuate rapidly," Adv. Funct. Mater., 24, 2163, 2014.
189. M. Park, Y. Ohm, D. Kim, Y.-L. Park, "Multi-material soft strain sensors with high gauge factors for proprioceptive sensing of soft bending actuators," in Proc. IEEE 2019 Int. Conf. on Soft Robotics (RoboSoft), 384, 2019.
190. Y.-L. Park, B. R. Chen, R. J. Wood, "Design and fabrication of soft artificial skin using embedded microchannels and liquid conductors," IEEE Sens. J., 12, 2711, 2012.
191. T. Kim, Y.-L. Park, "A soft three-axis load cell using liquid-filled three-dimensional microchannels in a highly deformable elastomer," IEEE Robot. Autom. Lett., 3, 881, 2018.
192. J. Yin, V. J. Santos, J. D. Posner, "Bioinspired flexible microfluidic shear force sensor skin," Sens. Actuators A, 264, 289, 2017.
193. R. Fearing, "Simplified grasping and manipulation with dexterous robot hands," IEEE J. Rob. Autom., 2, 188, 1986.
194. M. T. Mason, K. M. Lynch, "Dynamic manipulation," in Proc. 1993 IEEE/RSJ Int. Conf. on Intelligent Robots and Systems (IROS), 152, 1993.
195. Y.-L. Park, S. C. Ryu, R. J. Black, K. Chau, B. Moslehi, M. R. Cutkosky, "Exoskeletal force-sensing end-effectors with embedded optical fiber-Bragg-grating sensors," IEEE Trans. Rob., 25, 1319, 2009.
196. F. Ikhouane, J. Rodellar, Systems with Hysteresis: Analysis, Identification and Control Using Bouc-Wen Model, John Wiley & Sons, Hoboken, NJ 2007.
197. X. Tan, R. V. Lyer, "Modeling and control of hysteresis," IEEE Control Syst. Mag., 29,

26, 2009.

198. T. Vo-Minh, T. Tjahjowidodo, H. Ramon, H. Van Brussel, “A new approach to modeling hysteresis in a pneumatic artificial muscle using the Maxwell-slip model,” IEEE/ASME Trans. Mechatron., 16, 177, 2011.

국문 초록

본 논문은 인간 친화적이고 주변 환경에 적응할 수 있는 로봇 시스템의 개발을 가장 큰 목표로 다룬다. 논문은 인간, 로봇, 환경 상호 작용의 성능의 개선을 위해 소프트 로봇 기술로부터 그 해결책을 찾고자 한다. 궁극적인 목표의 달성을 위해 세가지의 실질적 문제가 정의된다.

첫번째 문제는 인간, 로봇, 환경 각각의 시스템을 정확하게 인식하는 것이다. 2장에서는 이 문제를 해결하기 위해 개선된 민감도를 갖는 다중 강성 센서 구조를 제안한다. 그리고 이 구조의 성능을 이론적 모델링과 실험적 검증을 통해 입증한다.

두번째 문제는 로봇 및 환경과의 상호작용을 위해 가장 적극적이고 정교하게 사용되는 인간 손의 움직임을 측정하는 것이다. 3장에서는 측정의 정확성과 구조의 간결함을 동시에 확보하기 위해 다중 강성 센서 기반의 착용형 장갑을 개발하고, 이 장갑의 캘리브레이션을 위한 정확한 레퍼런스 데이터 수집을 위한 후처리 방법을 제안한다. 또한 정량 및 정성 평가를 통해 제안한 손 트래킹 시스템의 우수한 정확성과 강건성을 입증한다.

세번째 문제는 소프트 로봇의 정확한 동작 제어를 위한 자가 감각 기능의 구현과 이 로봇의 상태를 다시 인간에게 전달할 수 있는 햅틱 디바이스 개발을 통해 인간과 로봇을 연결하는 것이다. 4장에서는 구조적 간결성, 낮은 입력 전압 및 고유한 안전성을 갖춘 이온 기반 전기 활성 고분자 구동기를 해결책으로 선택한다. 소프트 센서가 통합된 고분자 구동기와 햅틱 디바이스가 통합된 소프트 그리퍼 시스템의 정확한 원격 조작을 통한 실용적인 파지 및 놓기 작업을 시연한다.

마지막 문제는 소프트 로봇과 주변 환경을 연결하여 전체 상호 작용을 완성하는 것이었다. 5장에서는 높은 복잡도를 갖는 소프트 로봇의 기구학을 단순화하기 위한 하이브리드 시스템 분석 방법을 제안한다. 이를 통해 환경과 상호작용하는 동안 로봇은 내장된 센서를 활용하여 환경을 식별하고 이에 적응할 수 있다. 이 방법을 실제로 구현하기 위해, 미

지의 물체를 잡기 위한 공압 그리퍼 시스템을 예로 든다. 제안된 분석 방법을 통해 로봇 그리퍼는 미지의 물체의 크기를 추정하고 이에 기반해 자신의 위치를 조절함으로써 주어진 작업을 성공적으로 수행한다.